



Skolkovo Institute of Science and Technology

Characterization and Optimization of Organic Redox-Active Electrode Materials for
Potassium-Ion Batteries
Doctoral Thesis

by

VAHID RAMEZANKHANI

Doctoral program in MATERIALS SCIENCE AND ENGINEERING

Supervisor
Assistant Professor Stanislav S. Fedotov

Moscow - 2023

© Vahid Ramezankhani 2023

I hereby declare that the work presented in this thesis was carried out by myself at Skolkovo Institute of Science and Technology, Moscow, except where due acknowledgement is made, and has not been submitted for any other degree.

Candidate (Vahid Ramezankhani)

Supervisor (Assistant Professor Stanislav S. Fedotov)

Abstract

Scientists developing energy storage systems, particularly metal-ion batteries and beyond, are redeemers of Earth, targeting by-products resulting from the massive usage of traditional fossil fuels. Despite the current breakthroughs in the progress of lithium-ion batteries (LIBs), the ever-growing market demand/expenses, as well as the incorporation of environmentally hazardous materials in LIBs, will not relieve corresponding challenges by 2030. Therefore, it is imperative to implement practical strategies to address these challenges through either recycling precious elements from used batteries or introducing alternative technologies such as post-lithium batteries. To address these issues, novel electrode materials must be produced from light and earth-abundant elements such as alkaline Na, K, and non-metallic N, H, S, O P, and F. Potassium-ion batteries (PIBs) have been considered a proper replacement due to the vast abundance of K and a number of its fundamental advantages over Li such as higher electropositivity in carbonate electrolytes resulting in higher electrode potentials, faster diffusion in liquids owing to smaller Stoke's radius and in solids due to larger ionicity of K-O bonds, non-alloying with aluminium, etc. Another reason for the increasing interest in PIBs recently is similar ion storage mechanisms in the electrodes as for the materials reported for LIBs. In addition, there is a substantial amount of research effort focused on introducing non-toxic and environmentally benign electrode materials for metal-ion batteries. Redox-active polymers represent a promising solution. Furthermore, organic redox-active materials could enable record-high capacities and energy densities since they are composed of common

lightweight chemical elements. Another important feature of organic redox-active materials is that they usually have a soft amorphous structure, which makes them non-specific to the inserting ions. Therefore, the same material can operate equally well in Li, Na, and K-ion batteries. Among all explored organic materials, carbonyl-containing organic redox-active materials have appealed tremendous attention. However, this class of materials possesses some challenges in terms of cyclability and conductivity. Herein, this dissertation focuses on circumventing the common obstacles in the further developments of carbonyl-containing organic materials which are the stabilization and optimization of capacity, cyclability, electrode composition, and mass loading of this family of organic materials.

Publications

Main author

1. **Ramezankhani V**, Yakuschenko I K, Mumyatov A V, Vasil'ev S G, Zhidkov I S, Kurmaev E Z, Shestakov A F, Troshin P A. Octahydroxytetraazapentacenedione: New organic electrode material for fast and stable potassium batteries. Journal of Power Sources. 2022 Jan;517:230711.

Role: Carried out battery assembling, electrochemical characterization, obtained data, analyzed data, prepared high-quality figures, and wrote the whole manuscript except DFT calculation and synthesis part. Significantly, I prepared responses to all questions asked by reviewers.

Journal of Power Sources. Impact Factor at the date of defense (2023): 9.2

2. **Ramezankhani V**, Yakuschenko I K , Vasilyev S, Savinykh T A, Mumyatov A V, Zhidkov I S, Shchurik E V, Kurmaev E Z, Shestakov A F, and Troshin P A. High-capacity polymer electrodes for potassium batteries. Journal of materials chemistry A. 2022 Jan;10:3044.

Role: Carried out battery assembling, electrochemical characterization, obtained data, analyzed data, prepared high-quality figures, and wrote the whole manuscript except synthesis and DFT calculation. Significantly, I prepared responses to all questions asked by reviewers.

Journal of Materials Chemistry A. Impact Factor at the date of defense (2023): 11.9

3. **Ramezankhani V**, Kozlov A, Shchurik E V, PluczykMałek S, Vasil'ev S, Mumyatov A V, Shestakov A F, and Troshin P A. High-capacity potassium-ion batteries using new rigid backbone quinone-based polymer electrode materials. *Journal of Power Sources*. 2023 Feb;562: 232744.

Role: Carried out battery assembling, electrochemical characterization, obtained data, analyzed data, prepared high-quality figures, and wrote the whole manuscript.

Significantly, I prepared responses to all questions asked by reviewers.

Journal of Power Sources. Impact Factor at the date of defense (2023): 9.2

Co-author

4. Slesarenko A, Yakuschenko I K, **Ramezankhani V**, Sivasankaran V, Romanyuk O, Mumyatov A V, Zhidkov I Tsarev S, Kurmaev E Z, Shestakov A F, Yarmolenko O V, Stevenson K J, Troshin P A. New tetraazapentacene-based redox-active material as a promising high-capacity organic cathode for lithium and potassium batteries. *Journal of Power Sources*. 2019 Jun;235:226724.

Role: Carried out battery assembling, electrochemical characterization, obtained data, analyzed data, prepared figures, and wrote the part pertaining to the electrochemical characterization.

Journal of Power Sources. Impact Factor at the date of defense (2023): 9.2

Acknowledgment

I would like to express my deepest gratitude to all those who have supported me throughout my Ph.D. journey. Firstly, I appreciate my family's unwavering support and understanding during this long and challenging period. Despite not being able to visit them as often as I would have liked, they remained a constant source of encouragement and motivation. This project was conducted under the support of Professor Keith J. Stevenson's Russian Science Foundation grant No. 16-13-00111. I would like to express my sincere gratitude to him for his invaluable contributions to project administration, insightful comments, and expert consultation.

I would also like to extend my heartfelt appreciation to my supervisors and supportive colleagues who played a pivotal role in guiding and assisting me throughout my Ph.D. journey.

Prof. Stanislav S. Fedotov because of editing and commenting on the dissertation;

Prof. Pavel A. Troshin because of the project supervision;

Dr. Igor K. Yakuschenko because of providing materials (**OHTAP, OHTAPQ, P1-P6**);

Dr. Alexey Kozlov because of providing materials (**P7-P9**);

Prof. Sergey Vasilyev because of NMR experiments;

Prof. Alexander F. Shestakov because of DFT calculation;

Dr. Visweshwar Sivasankaran because of the preliminary introduction of battery assembling.

Novelty

1. Scientists have proposed the use of certain tetraazopentacene derivatives as electrode materials for metal-ion batteries; however, no experimental confirmation of octahydroxytetraazapentacene (**OHTAP**) has been provided so far. Therefore, for the first time, we have investigated the energy storage properties of **OHTAP**. Furthermore, the novel organic molecular structure, octahydroxytetraazapentacenedione (**OHTAPQ**), with superior electrochemical performance in comparison to **OHTAP** has been reported in this dissertation.

2. We present and examine a set of six innovative redox-active polymers (**P1-P6**) derived from triquionoyl. These polymers exhibit impressive specific capacities in potassium batteries, along with reliable charge-discharge cycling at both low and high specific currents exceeding 10 A g^{-1} . Consequently, these specially designed polymers hold great potential as electrodes for ultrafast K-ion batteries, which are essential for various stationary and portable electric propulsion applications.

3. We introduce a novel family of polymeric materials, **P7-P9**, which are based on ladder-type quinones with a rigid structure that ensures their excellent chemical and conformational stability, making them promising for storing potassium ions. Other advantages of this family of polymers are: i) easy synthesis process ii) producible in large quantities at a low cost, iii) the potential candidate for various applications, and iv) insoluble in common organic solvents, including those used in battery electrolytes.

Table of Contents

Abstract	3
Publications	5
Acknowledgment	7
Novelty	8
List of Symbols, Abbreviations Term – Definition	12
List of figures	15
List of tables	21
1. Introduction	22
1.1. Thesis structure	24
2. Background	25
2.1 Why potassium-ion battery?	25
2.1.1 General introduction to K-ion batteries	25
2.2 Battery specification	27
2.2.1 Theoretical capacity	28
2.2.2 Capacity and current density.....	28
2.2.3 Specific gravimetric energy and power density.....	29
2.2.4 Coulombic efficiency (CE).....	29
2.3 How to distinguish battery from supercapacitor materials?	30
2.3.1 A brief introduction to the CV technique	30
2.3.2 Kinetic study of electroactive materials.....	31
2.4 Electrolyte	32

2.4.1 Exploring K-containing salts	34
2.4.2 Exploring solvents	35
2.5 Categorizing the reported K-organic batteries	36
2.6 Carbonyl-containing organic electrode materials	39
2.6.1 A thioether (-S-) linker group	39
2.6.2 An imino (-NH-) linker group.....	41
2.6.3 Other organic electrode materials	41
2.7 Dual-Ion Batteries.....	44
2.8 B-type electrode materials	46
2.9 Potassium metal: a member of alkali metal anode.....	47
2.10 Carbon-based anode materials	48
2.10.1 Graphite.....	48
2.10.2 Soft carbon.....	50
2.10.3 Hard carbon.....	51
2.11 Alloying materials.....	52
2.12 Conversion Materials	54
2.13 Polyanion compounds.....	54
2.13.1 V and Ti-based polyanion anodes.....	56
2.14 Concluding remarks	57
3. Thesis objectives.....	59
4. Methodology and techniques	61
4.1 Assembling of potassium half-cells for polymers	61

4.2 Potassium battery fabrication by spray-coating	63
4.3 Pre-potassiation of organic materials	63
4.4 Material characterization	64
5. Design of potassium batteries using organic redox-active materials	66
5.1. Introduction	66
5.2 New tetraazapentacene-based redox-active material as a promising high-capacity organic cathode for potassium batteries	70
5.3. Octahydroxytetraazapentacenedione: New organic electrode material for fast and stable potassium batteries	73
5.4 High-capacity polymer electrodes for potassium batteries	83
5.5 High-capacity potassium-ion batteries using new rigid backbone quinone-based polymer electrode materials	94
5.6 Concluding remarks	107
6. Concluding remarks	111
6.1 Introduction	111
6.2 Composition and energy density optimization	112
6.3 Battery specification comparison with the benchmark	113
6.4 Capacity retention comparison with benchmark	116
6.5 Recommendations for the prospective research	119
Bibliography	121
Appendices A	141

List of Symbols, Abbreviations Term – Definition

PIBs – Potassium-ion batteries

IEA – International Energy Agency

LIBs – Lithium-ion batteries

LNMC622 – $\text{LiNi}_{0.6}\text{Mn}_{0.2}\text{Co}_{0.2}\text{O}_2$

KNMC622 – $\text{KNi}_{0.6}\text{Mn}_{0.2}\text{Co}_{0.2}\text{O}_2$

HOMO – Highest occupied molecular orbital

LUMO – Lowest unoccupied molecular orbital

OCV – Open circuit voltage

C_{theo} – Theoretical capacity

CE – Coulombic efficiency

SEI – Solid electrolyte interface

PBA – Prussian blue analogue

KPF_6 – Potassium hexafluorophosphate

KFSI – Potassium bis (fluorosulfonyl) imide

EC – Ethylene carbonate

PC – Propylene carbonate

DMC – Dimethyl carbonate

EMC – Ethyl methyl carbonate

G_1 – Monoglyme

G_2 – Diglyme

G_4 – Tetraglyme

MOFs – Metal-organic frameworks

B-type – Bipolar-type

HAWP – High average working potential

PAQS – Poly (p-phenylene sulfide)

PPTS – Poly (pentacenetrone sulfide)

PANI – Polyaniline

PQs – Polydiaminoanthraquinones

PoPD – Poly(*o*-phenylene diamine)

CuTCNQ – Copper-tetracyanoquinodimethane

Q-TTF-Q – Benzoquinone-tetrathiafulvalene triad

p-Na₂C₆H₂O₆ – Para-disodium-2,5-dihydroxy-1,4-benzoquinone

o-Na₂C₆H₂O₆ – Ortho-disodium salts of tetrahydroquinone

K₄PM – Tetra potassium pyromellitic

PTCDA – 3,4,9,10-perylene-tetracarboxylic acid-dianhydride

TQY – Triquinoxalinylene

HAT – Hexaazatriphenylene

ADAPTS – Azobenzene-4, 4' - dicarboxylic acid potassium salts

PTPAn – Poly (triphenylamine)

PDPPD – Poly(N, N' - diphenyl-P-phenylenediamine)

PVK – Poly(*N*-vinylcarbazole)

PTMA – Poly (2,2,6,6- tetramethylpiperidinyloxy-4-ylmethacrylate)

CNT – Carbon Nanotube

G – Graphite

EG – Expanded graphite

HC – Hard carbon

T – Temperature

PDPA – Polydiphenylamine

XRD – X-ray diffraction

SEM – Scanning electron microscopy

EDX – Energy dispersive X-ray spectroscopy

FTIR – Fourier-transform infrared spectroscopy

TEM – Transmission electron microscopy

NMR – Nuclear magnetic resonance

OHTAP – Octahydroxytetraazapentacene

OHTAPQ – Octahydroxytetraazapentacene

P1-P9 – Polymers # 1-9

MWCNTs – Multi-Walled Carbon Nanotubes

CV – Cyclic voltammetry

ESR – Electron spin resonance

List of figures

Fig. 1.1 Cost analysis of conjectural KNMC||G (a) and LNMC||G (b)

Fig. 2.1 The introduction of metal-ion full and dual-ion half-cells and their corresponding mechanisms for K-ion storage

Fig. 2.2 The way of obtaining CE and Energy density from the charge and discharge profile

Fig. 2.3 CV of single electron transfer reaction while the scan rate is increased. (158)

Fig. 2.4 Schematic representation of electrode and band diagram, SEI formation, and concept of V_{oc}

Fig. 2.5 The main characteristic of solvents used in electrolytes. a) Dielectric constant trend at 25°C and b) viscosity evolution at 25 °C and constant pressure.

Fig. 2.6 Different types of organic redox-active materials explored in PIBs with advantages and disadvantages.

Fig. 2.7 Schematic representation of organic redox-active types and corresponding K-ion storage mechanisms a) *n*-type, b) *p*-type, and c) B-type organic redox-active materials.

Fig. 2.8 *n*-doped aminoxyl salt (a) *p*-doped oxoammonium salt.

Fig. 2.9 All organic molecular structures discussed above. a) *n*-type organic materials (black colour) b) bipolar (dark green colour) c) *p*-type (red colour).

Fig. 2.10 AB Bernal stacking schema of graphene (a), triple stages of K-ion storage in graphite (b), the first charge and discharge profile of G||K at the current density of 27.9 mA g⁻¹ (c), waterfall XRD pattern of G||K during discharge and charge (d). (129)

Fig. 2.11 A schematic representation of connected octahedron and tetrahedron with the possible embedded elements in the KTP structure (a) and 3D image of KTP structure projected along [010] direction (b).

Fig. 3.1 Research methodology flow chart

Fig. 4.1 Schematic representation of half-cell (a) and Electrode preparation process (b).

Fig. 5.1 Molecular structures of all investigated organic materials

Fig. 5.2. The charge-discharge profiles (a) and cycling performance of K||**OHTAP** cells at C/10 current rate (cathode deposited on Al foil by tape casting (b). cycling performance of the K||**OHTAP** cells at 1C current rate (spray-coated cathode on Al/C current collector) (c). (The composite electrode formulations used in both deposition techniques are 50:40:10 wt. % of **OHTAP**: Carbon super P: PVDF and the electrolyte formulation is 1 M (KTFSI) in (DOL:DME = 1:1 v/v).)

Fig. 5.3 SEM image of the composite electrode containing **OHTAPQ**.

Fig. 5.4 Cyclic voltammogram of **OHTAPQ**||K cell with 2.2M KPF₆ solution in G₂ as electrolyte recorded at the rate of 100 mV s⁻¹ (a). The high-resolution core-level O 1s (b) and N 1s spectra of **OHTAPQ**-based electrodes in the pristine state, after the first discharge to 0.7 V and the first charge to 4 V (c). M-ion storage and release mechanism of **OHTAPQ**.

Fig. 5.5 Cyclic voltammograms recorded at different voltage sweep rates (a) and the power law dependence of the peak current on scan rate (b) used for the estimation of the parameter b .

Fig. 5.6 Comparison of cycling performance of **OHTAPQ**||K half-cell in 1 M KTFSI in (DOL:DME = 1/1 v/v) (a) and 2.2 M KPF₆ in G₂ (b). Charge-discharge profile in the voltage range of 0.7-4 V (c) and the average discharge cell potential in G₂-based electrolyte (d).

Fig. 5.7 The cycling behavior of the potassium half-cells with **OHTAPQ** electrodes at the current densities of 0.6 A g⁻¹ and 1.2 A g⁻¹ without initial preconditioning.

Fig. 5.8 SEM images of the pristine composite electrode (a) and after >2000 charge-discharge cycles in a cell using G₂-based electrolyte (b).

Fig. 5.9 Cycling behavior of the potassium half-cells assembled with **OHTAP** (**OHTAPQ** analog without two carbonyl groups) electrode material and 2.2M KPF₆ in G₂ as electrolyte.

Fig. 5.10 The rate capability of **OHTAPQ** ||K half-cells assembled with 2.2 M KPF₆ in G₂ after preconditioning (a) and charge-discharge curves for every 10 cycles (b).

Fig. 5.11 Synthesis of polymers **P1-P6**. The differently substituted triquinoyl fragments in the structures of **P4-P5** are represented by circles; the drawn motifs just illustrate the complexity of these statistical copolymer structures and should not be considered as the exact representations of the molecular structures of these materials.

Fig. 5.12 Cyclic voltammograms of **P1** at 1 mV s^{-1} (five cycles shown) (a) and ATR-FTIR spectra of pristine and potassiated electrodes (b). The K-ion storage and release mechanism for **P1** (c).

Fig. 5.13 Discharge capacities of **P1**||K half-cells (a) and charge-discharge profiles (b) at various current densities.

Fig. 5.14 Cycling performance of **P1**||K half-cells within the potential window of 0.7-4 V (a), the selected charge-discharge profiles (b), and the average discharge potential plotted as a function of the cycle number (c).

Fig. 5.15 The CV plots of **P1**||K half-cells recorded at different voltage scan rates (a), the plot of the peak current versus the voltage scan rate (b), and the relative contributions of the capacitive and diffusion currents at different scan rates (c).

Fig. 5.16 Introduction and synthesis process of polymers **P7-P9**.

Fig. 5.17 SEM images of the pristine powders of polymers **P7** (a), **P8** (b) and **P9** (c).

Fig. 5.18 Cyclic voltammogram of **P7** at 20 mV s^{-1} scan rate after galvanostatic preconditioning at 360 mA g^{-1} (a). ATR-FTIR spectra of pristine and metallated **P7** powders (b). The scheme illustrating K^+ storage and release in **P7**-based electrodes (c).

Fig. 5.19 Rate capability (top row), charge-discharge profiles (middle row), and the evolution of the cell discharge capacity upon cycling (bottom row) for the potassium half-cells assembled with the composite electrodes comprising polymers **P7** (a-c), **P8** (d-f), or **P9** (g-l) as redox-active materials.

Fig. 5.20 The evolution of the specific capacity of the composite electrode comprised of 70 wt. % of **P7** upon battery cycling (a) and charge-discharge profiles of the **P7**||K half-cells within the potential range of 0.7-4 V (b).

Fig. 5.21 The evolution of the specific capacity of the composite electrode comprised of 70 wt. % of **P7** upon battery cycling (a) and charge-discharge profiles of the **P7**||K half-cells within the potential range of 0.7-4 V (b).

Fig. 5.22 The evolution of the cell discharge capacity upon cycling (left column) and charge-discharge profiles (right column) for the potassium half-cells assembled with the composite electrodes comprising 85 wt. % of polymers **P7** (a-b), **P8** (c-d), or **P9** (e-f) as redox-active materials, 10 wt. % of MWCNTs and 5 wt. % of PVdF binder. The charge-discharge cycling was performed at the current density of 30 mA g⁻¹.

Fig. 5.23 The evolution of the cell discharge capacity upon cycling (left column) and charge-discharge profiles (right column) for the potassium half-cells assembled with the composite electrodes comprising 85 wt. % of polymers **P7** (a-b) or **P8** (c-d) as redox-active materials, 10 wt. % of MWCNTs and 5% of PVdF binder. The charge-discharge cycling was performed at the current density of 70 mA g⁻¹.

Fig. 6.1 Comparison of the presented results with the best-reported positive electrode materials (a) negative electrode materials (b) comparison of the presented results with the best-reported half-cells in terms of energy and power density (c)

Fig. 6.2 Active mass content comparison of the investigated materials with other carbonyl-containing organic materials.

Fig. 6.3 Capacity retention comparison of polyanion and organic redox active materials with the best-reported materials so far.

Fig. 6.4 Morphology of composite electrodes containing **P1** (a) and **OHTAPQ** (b)

Fig. 6.5. SEM image of the composite electrodes containing **P2** (a), **P3** (b), **P4** (c), **P6** (d), **P7** (e) and **P8** (f).

Fig. 6.6 Proposed electron withdrawing groups (shown in red) to be introduced in the molecular structure. (135)

Fig. 6.7 Possible scenarios to assemble full potassium batteries. All organic (a), hetero-structure (b)

List of tables

Table 2.1 Physico-electrochemical properties of alkali metals and other (di)/trivalent elements in metal-ion batteries (14,57).

Table 2.2 Initial alloying materials with their conductivity and final alloying product with associated theoretical capacity.

Table 5.1 Overview of the electrochemical performance of polymers **P1-P6**.

Table 5.2 Surface area properties of **P1-P6**.

Table 5.3 Basic electrochemical performance parameters for potassium half-cells assembled using **P7-P9** electrode materials.

Table 6.1 Summary of the obtained results.

Chapter 1

1. Introduction

It is well-known that potassium has advantageous over lithium in terms of abundance, price. Nevertheless, according to the “*hypothetical techno-economic analysis*”, the price of full K-ion exceeds Li-ion battery technology while utilizing $\text{LiNi}_{0.6}\text{Mn}_{0.2}\text{Co}_{0.2}\text{O}_2$ (LNMC622) and $\text{KNi}_{0.6}\text{Mn}_{0.2}\text{Co}_{0.2}\text{O}_2$ (KNMC622) cathodes and graphite anode for both technologies (Fig. 1.1). The cost for electrodes (both anode and cathode) in PIBs compromises 34.9% vs. 28.4% in the LIBs technology. (1) Thus, it is highly recommended to focus on the development of the novel and promising electrode materials to tackle costly and non-environmental benign electrode materials. Another obstacle in presenting the technological feasibility of PIBs is the cyclability of batteries while graphite is not only a critical material but also has an inappropriate volume expansion, leading to the short cycle life of batteries, especially in the case of PIBs.

Hence, the investigation of alternative materials for post-lithium-ion battery technology inspires us to explore the electrochemical behavior of novel and promising materials. Although materials containing heavy transition elements with rigid structures do exist. Such inorganic materials have a complicated mechanism for bulky K-ion de/intercalation causing crystal structure modification and volume expansion. Thus, these issues are leading to the capacity degradation of batteries. In addition, conducting an in-depth investigation

of electrodes of this nature necessitates the utilization of advanced techniques that are not typically accessible in conventional research laboratories.

However, organic redox-active materials do not have a complex synthesis process and ion storage pathway. Among different types of organic materials, carbonyl-containing ones endow the advantage of high theoretical capacities due to the existence of a palette of functional groups and the inclusion of light elements in the molecular structure. However, in order to empower the technological feasibility of this type of material, one might circumvent the drawbacks corresponding to carbonyl-functional group-based polymers such as dissolution of active materials, capacity fading, low mass-loading, inferior electrode composition (less active material contribution), adverse conductivity and improper initial coulombic efficiency (ICE). The main focus of this dissertation is electrochemical characterization and solving the aforementioned issues highlighted above. In what follows, the next chapters of this dissertation are described.

1.1. Thesis structure

Chapter 2- Background Introduction about battery performance, a literature survey on organic materials, electrolytes, and inorganic negative electrode materials.

Chapter 3- Thesis object. In this chapter, the thesis objectives are introduced.

Chapter 4- Methodology and techniques.

Chapter 5- Design of potassium batteries using organic redox-active materials. This Chapter explores the novel **OHTAP** and **OHTAPQ**, a modified type of the monomer, adding two new carbonyl functional groups. In addition, electrolyte formulation, suppressing capacity fading compared to **OHTAPQ** is optimized. In addition, K-ion storage properties of a series of novel redox-active polymers derived from triquinoyl are investigated. The importance of applying a G₂-based electrolyte to achieve record-breaking gravimetric discharge capacity and energy density is concluded. a series of benzoquinone-based ladder-type with rigid backbone polymers as anode materials for potassium-ion batteries is also studied.

Chapter 6- Concluding remarks. In this chapter, the achieved results and the discussion of prospective developments are summarized.

Chapter 2

2. Background

2.1 Why potassium-ion battery?

The International Energy Agency (IEA) has predicted an unprecedented growth in demand for energy storage systems applied in electric vehicles, stationary storage, and portable electronic devices up to approximately 11600 GWh by 2040. (2) The imminent risk of LIB usage and the shortage of implemented resources globally has inspired scientists to consider complementing the current LIBs technology. Hence, it is imperative to explore its possible replacements. A couple of potential candidates for this purpose are neighboring alkali elements to Li in the periodic table, such as sodium-Na- and potassium-K. Despite Na being more abundant than potassium in Earth's crust and ocean, K has electrochemical similarity to Li and even some advantages such as a more negative potential vs. SHE in propylene carbonate (PC) and superior conductivity of K ion in 1 M KFSI in ethylene carbonate (EC)/diethyl carbonate (DEC). (3)

2.1.1 General introduction to K-ion batteries

Alkali-ion or secondary (rechargeable) batteries are usable due to their capability of ion storage in electroactive electrode materials due to reversible redox reactions.

Generally, to extract current from electrochemical reactions inside batteries, the latter are required to possess a couple of terminals (cathode and anode electrodes). The chemical medium between two electrodes is called an electrolyte, which is responsible for charge transport. One may assemble batteries in either half or full cells. The former enables to investigate the K-ion storage properties of electroactive materials, where organic or inorganic electrode materials are studied versus metallic potassium. However, this configuration is not recommended for practical application because of fire hazards resulting from dendrite formation. On the other hand, K-free and disordered (hard carbon) or crystalline electrode materials and K-embedded electrodes may serve as anodes and as cathodes, respectively. The fabricated battery has an open circuit voltage (OCV) showing a potential difference between the anode and cathode. During the exploitation, the battery undergoes the discharge process (change of voltage from OCV to 0 V), requiring K ions to shuttle from the anode to the cathode and transfer electrons from the negative electrode to the positive one to maintain charge neutrality. During the charging process, K-ions move from the negative (reductive) to the positive (oxidative) electrodes. Such a back-and-forth transfer of ions between two electrodes is referred to as a “rocking chair mechanism”. In addition to this mechanism, there is another ion storage pathway called dual-ion. (4) According to batteries functioning under this mechanism, separated anions/cations during the charging process react with the cathode/anode at high voltage. In the reverse process (discharging process), anions/cations deintercalate into the electrolyte (Fig. 2.1).

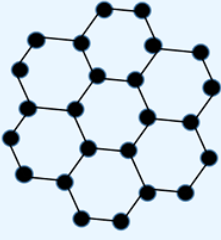
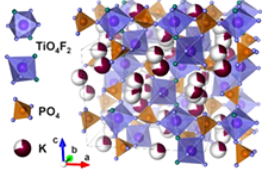
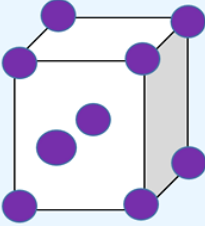
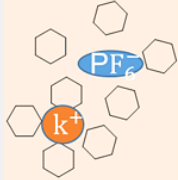
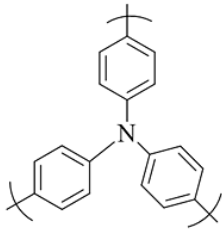
Anode (-)	Electrolyte and mechanism	Cathode (+)
 <p>G</p>	<p>Discharge: $\text{KTiPO}_4\text{F} \longrightarrow \text{K}_{(1-x)}\text{TiPO}_4\text{F} + x\text{K}^+ + xe^-$</p> <p>Charge: $\text{C}_6 + x\text{K}^+ + xe^- \longrightarrow \text{K}_x\text{C}_6$</p> <p>Overall reaction: $\text{KTiPO}_4\text{F} + \text{C}_6 \longrightarrow \text{K}_{(1-x)}\text{TiPO}_4\text{F} + \text{K}_x\text{C}_6$</p> <p>Configuration: Full cell</p> <p>Electrolyte: 1 M KPF_6 in EC:PC (1:1, V/V)</p>	 <p>KTiPO_4F</p>
 <p>K</p>	<p>Configuration: Half cell</p> <p>Electrolyte: 1 M KPF_6 in EC:PC (1:1, V/V)</p> 	 <p>PTPAn</p>

Fig. 2.1 The introduction of metal-ion full, dual ion half-cells, and their corresponding mechanisms for K-ion storage.

2.2 Battery specification

The main battery specifications, such as capacity, reversibility, stability, and rate performance of active materials under various current densities, can be achieved through the galvanostatic technique. this method is based on the application of a constant current and following the evolution of the cell voltage. The capacity delivered by coulomb counting when normalized to the mass or volume of the electrode can determine the specific capacity of the electrode under study.

2.2.1 Theoretical capacity

The maximum metal-ion storage capability is defined as the specific capacity shown in equation (1).

$$C_{\text{theo}} = \frac{26800 \cdot n}{M_w} \quad (1)$$

M_w : Molecular weight, n : Number of transferred electrons

2.2.2 Capacity and current density

In order to evaluate the K-ion storage properties of explored electrode materials and predict mass loading ratios for positive and negative electrodes, half-cells can be designed where metallic potassium serves as a reference/counter electrode in a two-electrode scheme. In a half-cell configuration, a specific current can be normalized to active mass (A g^{-1}) or C-rate (obtainable from theoretical capacity). For example, considering $C_{\text{theo}} = 133.4 \text{ mAh g}^{-1}$ of KTiPO_4F , 1C-rate means discharge for an hour to extract fully one potassium ion from this material. Thus, converting 1C from specific current to C-rate is $1\text{C} = 133.4 \text{ mA g}^{-1}$. The capacity (mAh g^{-1}) for this type of battery is preferably defined as gravimetric capacity. However, it is recommended to report the capacity of full cells based on areal capacity (mAh cm^{-2}) to better compare distinct implemented anode materials in the full-cell batteries.

2.2.3 Specific gravimetric energy and power density

The ability of active materials to store energy per unit mass in a half cell, or the amount of energy of a full cell measured with its total weight, including inactive electrochemical components, is referred to as gravimetric energy density and is known in (Wh kg^{-1}). As shown in Fig. 2.2, energy density can be measured by multiplying the average discharge potential by the maximum discharge capacity. The quickness of energy delivery can be shown as power density with a unit of W kg^{-1} .

2.2.4 Coulombic efficiency (CE)

CE (Fig.2.2) is defined as the ratio of discharge to charge capacity or the number of K ions inserted/intercalated into the cathode to the number of the same ions released from the anode. Due to parasitic cross-talk between electrode and electrolyte, CE remains less than 100%, particularly at the initial cycles. For example, electrolyte decomposition by-products may accumulate on the surface of the anode, leading to the use of K ions known as a non-faradaic or irreversible reaction.

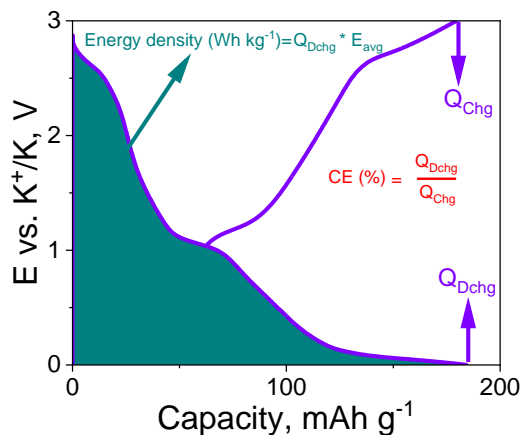


Fig. 2.2 The way of obtaining CE and Energy density from the charge and discharge profile.

2.3 How to distinguish battery from supercapacitor materials?

The kinetic study of redox electrode materials is a substantial way to realize the difference between battery and pseudocapacitive or supercapacitor materials. According to the cyclic voltammetry (CV) test, the influence of switching scan rate on current can be tracked to recognize whether the kinetic is diffusion-dominant (battery materials, e.g. LiFePO_4) or not. Hence, the electrochemical CV test is first elaborated below.

2.3.1 A brief introduction to the CV technique

CV refers to a dynamic, powerful, and popular electrochemical test that is exploited to study the redox process of either organic or inorganic materials. Such a technique is usable to investigate electrochemical reactions within or on the surface of electrodes. Based

on this test, a couple of target voltages (V_1 and V_2). are defined in order to voltage be swept between two pre-defined voltages at the specific scan or swept rates. CV is used to identify the reversibility of reactions, as shown in Fig.2.3 for the single electron transfer reaction. The reversibility of the redox reaction is shown through i) The peak to peak separation should be ~ 57 mV ii) non-modification of peak position as scan rate changes iii) The ratio of cathodic and anodic current peak should be 1 iv) cathodic and anodic peak currents should be proportional to the square root of scan rates. (158)

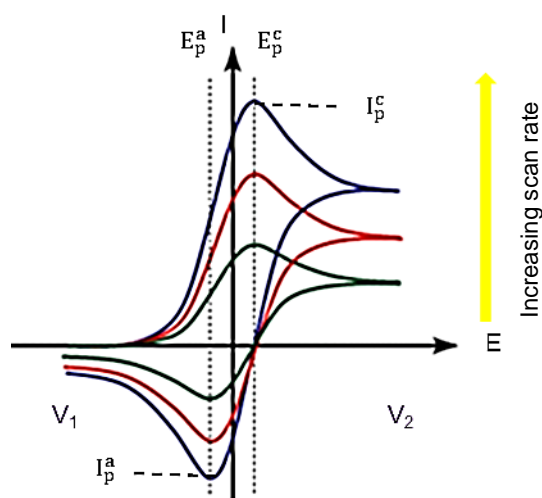


Fig 2.3 CV of single electron transfer reaction while the scan rate is increased. (158)

2.3.2 Kinetic study of electroactive materials

The current response from CV is originated from faradiac (diffusion-dominant (i_{diff})) and non-faradic (i_{cap}) processes. The mathematic formula where parameters a and b involved (equation 2) represents that the actual current is sum of slow diffusion-controlled process and near surface capacitive reactions on the surface of electrode.

$$i(v)=i_{\text{cap}}+i_{\text{diff}}=av^b \quad (2)$$

$$\text{Log } i(v)=\text{Log } a+b \text{ Log } v \quad (3)$$

To define the mechanism of ion storage, one may calculate a b value by deriving the slope of the plot, log i versus log v (equation 3). A b value around 0.5 shows that the materials has more diffusion-controlled process (battery materials) and a b value approximately 1 means that material has pseudocapacitive characteristic. Finally, A transition region (0.5 <b<1) means material in addition to diffusion controlled properties has capacitive contribution in storage of ions as well. (129)

2.4 Electrolyte

PIBs operate using the same mechanism as the LIB technology, known as the rocking-chair mechanism, where K ions move between the negative and positive electrodes via the electrolyte. The development of PIBs heavily relies on the proper design of the electrolyte formulation, including the appropriate concentration of salt and solvent. The selection of electrolyte formulations not only governs optimal battery performance but also plays a crucial role in understanding the interfacial properties between the anode and electrolyte. The solid electrolyte interface (SEI), a well-known obstacle that limits the progress and practical application of PIBs, allows K ions to shuttle between opposite electrodes while hindering electronic contacts between electrodes and electrolytes. (3)

The SEI layer forms when the lowest unoccupied molecular orbital of the negative electrode (LUMO) and the highest occupied molecular orbital (HOMO) of the positive

electrode used in a battery do not fulfil band structure criteria (Fig. 2.4). In other words, the SEI is the product of a mismatch of the redox potential of an anode (μ_A), when the Fermi level of the anode stays beyond the LUMO level as well as positioning redox potential of the cathode (μ_c) below the HOMO energy level of electrolyte. The well-known anode materials such as graphite (G), antimony (Sb), and red phosphorus (P) have a Fermi energy state beyond LUMO, leading the spontaneous reaction with the outcome of interphase layers formation. (5-7) The practical application of PIBs requires inventing electrolytes with novel formulations, exploiting proper salts and solvents. In what follows, the recent progress of electrolyte usage is discussed in detail:

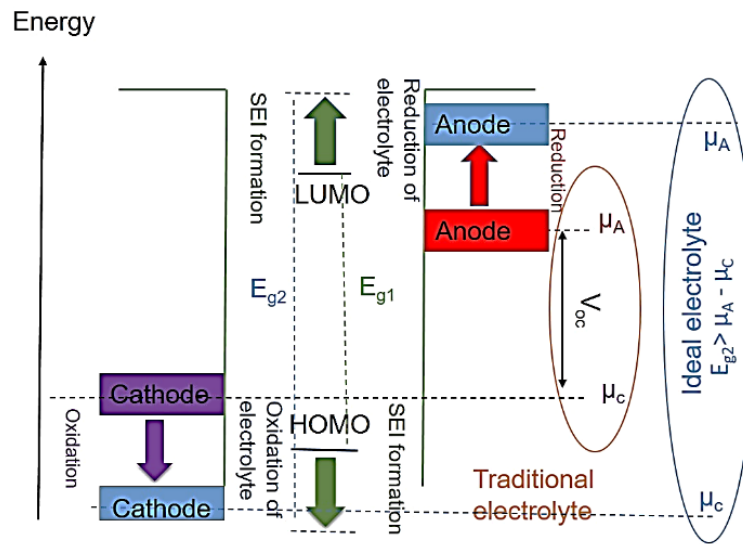


Fig. 2.4 Schematic representation of electrode and band diagram, SEI formation, and concept of V_{oc} .

2.4.1 Exploring K-containing salts

The conventional explored salts for PIBs, potassium hexafluorophosphate (KPF_6) and Potassium bis (fluorosulfonylimide (KFSI), have some advantages and disadvantages. To compare these salts, KFSI functionality is superior in the anode, while KPF_6 is showing better performance in high-voltage cathodes. (8) KFSI shows stronger solvation, which may result in fewer free solvent molecules. Furthermore, weak ionic bonding between K^+ cations and FSI⁻ anions leads to elevated conductivity. For example, the electrochemical characterization of anode materials such as Bi, Sn, and Sb in common electrolyte formulations like 0.8 M $\text{KPF}_6/\text{EC}:\text{DEC}$ and 1 M $\text{KFSI}/\text{EC}:\text{DEC}$ showed that the mechanical stability of SEI (homogeneity and integrity) of the KFSI-containing electrolyte was maintained for the first 10 cycles. On the other hand, KFSI is less applicable to high-voltage cathodes due to its higher oxidation tendency and resulting corrosion of the Al substrate. (9) Nevertheless, KPF_6 is able to cover such weak points because of its advantages such as superior stability at voltages above 4 V, passivation of Al foil, and cost-effectiveness. The decent performance of the Prussian blue analog (PBA) in terms of optimized discharge capacity, less polarization potential, and cyclability originates from the passivation properties of KPF_6 at higher operating voltage. (10) Given the (dis)advantages of these salts, the mixture of $(\text{KPF}_6)_x/(\text{KFSI})_y$ may be a reasonable approach to retain the benefits of each while covering the disadvantage of electrolytes in low/high voltages. It was found that ionic conductivity was improved through the blending strategy. Besides the fruitful result came out when $(\text{KPF}_6)_x/(\text{KFSI})_y$ formulation ($x:y=3$) is

exploited for $\text{K}_2\text{Mn}[\text{Fe}(\text{CN})_6]||\text{G}$ full cell, demonstrating a decent cycling performance for 500 cycles. (11)

2.4.2 Exploring solvents

The most studied solvents for PIBs are carbonates and ethers. There is a common trend in implementing solvents of the Li-ion technology in PIBs. For instance, cyclic, ethylene carbonate (EC) and propylene carbonate (PC), and linear carbonate, diethyl carbonate (DEC), dimethyl carbonate (DMC), and ethyl methyl carbonate (EMC) are usable in both technologies. (12) Among these classes of solvents, EC and PC have a potent ability to either dissolve salts or provide higher polarity (charge stabilization). In contrast, linear counterparts enable greater ionic mobility because of lower viscosity. In the electrolyte preparation, LUMO and HOMO energy levels of carbonate-based solvents when bonded with K-ion shift to lower energy levels indicating improved oxidation stabilities but reduced reduction stabilities. Similarly, the same trend in the alteration of energy levels is observed in ether K-ion complexes with more lowering LUMO resulting in far worse reduction stability. (8)

Glymes (ether-based electrolytes) are another fascinating family of linear-type solvents. Glymes with the general formula $[\text{R}-(\text{OCH}_2\text{CH}_2)_n-\text{OR}; n=1,2,4, \text{Monoglyme, Diglyme and Tetraglyme, respectively}]$ endow features such as the capability of forming mixtures in polar and non-polar liquids, and constituting metal complexes with metals (chelation). (13)

According to the criteria for ideal solvents for electrolytes, EC possesses a high dielectric constant that provides superior salt solubility and higher ionic conductivity (Fig. 2.5a). In addition, G₁ has less viscosity (Fig. 2.5b). Furthermore, EC with HOMO (-7.924 eV)

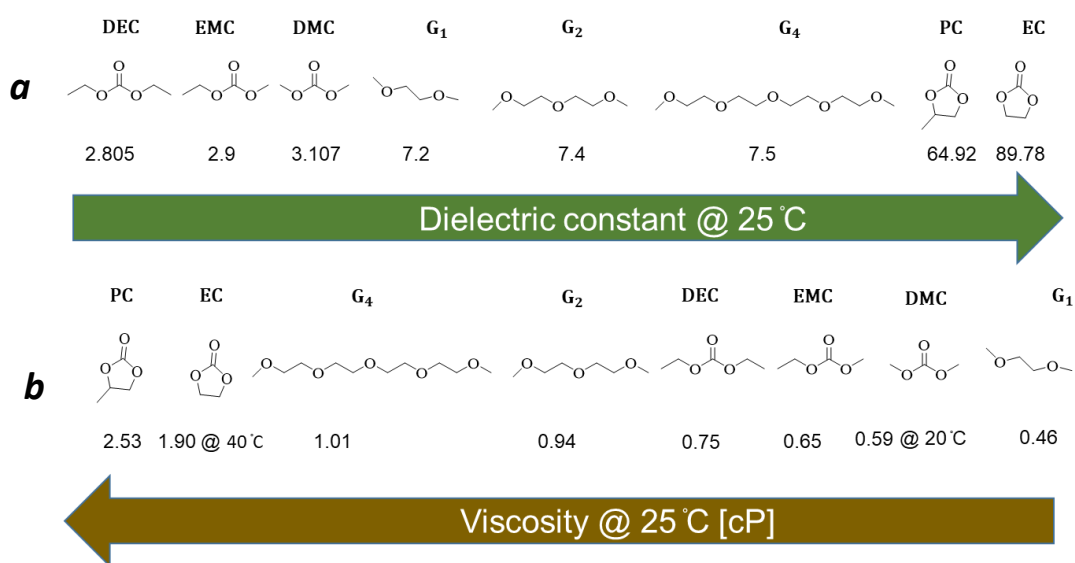


Fig. 2.5 Dielectric constant trend at 25^oC a) and viscosity evolution at 25^oC and constant pressure b).

presents better oxidation stability at a higher potential. Nevertheless, G₁ with LUMO (2.532 eV) demonstrates proper reduction at lower potential leading to less risk of SEI formation. (13)

2.5 Categorizing the reported K-organic batteries

There are a couple of approaches for the classification of organic materials with storage usages:

1. According to electronic configurations, i.e., being *n*, *p*, or bipolar;
2. According to the electroactive functional groups, i.e., possessing carbonyl, azo, nitrogen-containing, metal-organics (MOFs), and so on (Fig. 2.6).

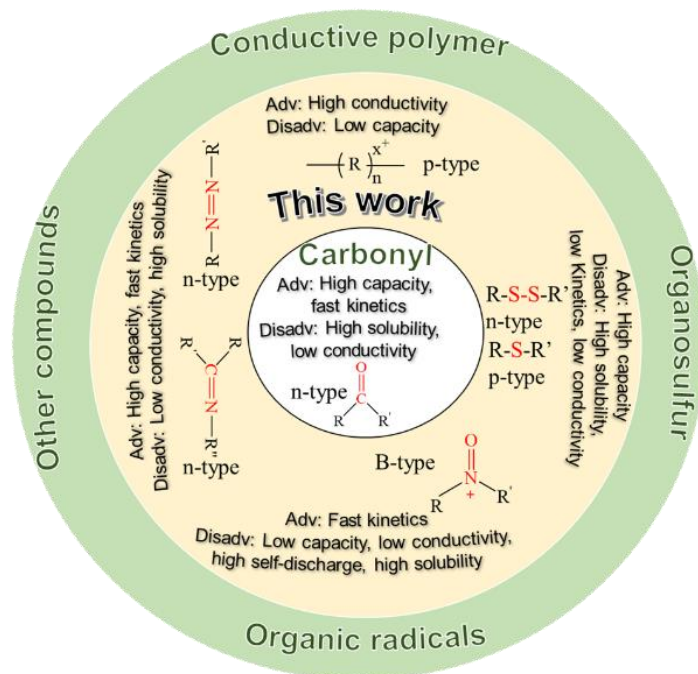


Fig. 2.6 Different types of organic redox-active materials explored in PIBs with advantages and disadvantages.

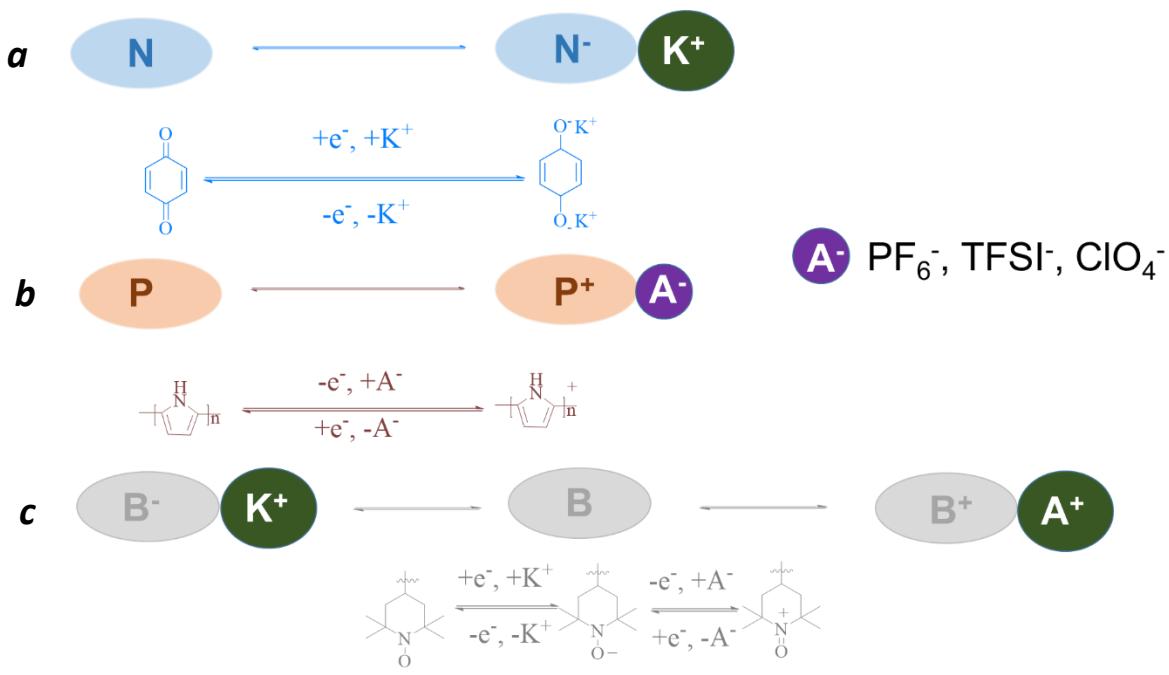
Based on the first categorization approach, *n*-type organics (Fig. 2.7a) use carbonyl groups and pyrazine rings that enable them to attract counter ions through reduction. Conversely, *p*-type materials (Fig. 2.7b) capture negatively charged anions through oxidation. Bipolar organics possess both *p*- and *n*-type properties that might first reduce or oxidize. The practical implementation of either *n*- or *p*-type organics relies on their redox potential. Hence, *p*-type organics always serve as positive electrodes while *n*-type ones are applicable

for both negative and positive electrodes. It is worth mentioning that the theoretical capacities of the *p*-type are normally less than those of *n*-type counterparts due to the presence of redox-inactive parts in the molecular structure. (15)

Bipolar (B-type) polymers (Fig. 2.7c) present both *n*- and *p*-type features. This means that upon the applied voltage they are able either to oxidize to form B^+ or to reduce in the form of B^- . (16)

Investigated polymer electrodes, particularly nitrogen-containing polymers, have a high average working potential (HAWP) of 3.2-4.1 V (vs. K^+/K) in dual-ion batteries. However, organic electrodes containing carbonyls and disulfides, where cation insertion is the dominant storage pathway, possess a working potential of less than 3.0 V (vs. K^+/K), which is unsuitable for cathode applications. The redox potential of the organic materials is determined by the energy of the molecular orbital and the dislocation of electron density of aromatic rings. (17) This means that electroactive groups with the ability to modify the electronic properties of organic molecules, either donation or withdrawal, are capable to manage the potential of the whole molecule. To gain a deeper insight into this phenomenon, strong electronegative groups such as halogenides (18–22), cyanides (22–24), sulfonyls (25,26), and heteroaryls (27–29), can be attached to main functional groups to lower the lowest unoccupied molecular orbital (LUMO) and boost anion uptake, resulting in a higher redox potential to provide electrons. Moreover, there is another approach to boosting the potential. For example, instead of attaching the functional groups to meta-, ortho-, and para- positions, one may substitute the carbon in the aromatic rings with O, N,

and S to delocalize electron density, thus improving the overall potential of the complex molecule. (30). In contrast, the elevation of LUMO level or decreasing electron affinity of



organic materials is feasible through electroactive groups with weaker electronegativity such as amino, alkyl groups, methoxy group, $-\text{OLi}/\text{Na}$). (18, 31,32)

Fig. 2.7 Schematic representation of organic redox-active types and corresponding K-ion storage mechanisms a) N-type, b) P-type, and c) B-type organic redox-active materials.

2.6 Carbonyl-containing organic electrode materials

2.6.1 A thioether (-S-) linker group

According to the Phillips synthesis route, an (-S-) bond is linked to the benzoquinone rings in the main chain through the polycondensation of dihalogenated

monomers and Na₂S. Poly(p-phenylene sulfide) (PAQS) and poly(pentacenetrone sulfide) (PPTS) have been reported for PIBs. (33,34) Obtaining such compounds requires meeting certain criteria for polymerizations, such as (i) using NMP or DMF as a strong polar solvent (ii) utilizing Na₂S as an anhydrous salt, and (iii) maintaining proper reaction temperature (T>150 °C). The average discharge potentials and redox-active centers of PAQS (1.9 V, 2e) and PPTS (1.65 V, 4e) are achieved in the potential window of 1.5-3.4 V and 0.8-3.2 V vs. K⁺/K respectively. Despite incorporating more active centers in the molecular structure of PPTS, either the inclusion of more electron-donating active groups or charge repulsion among active centers may be responsible for the drop in average potential. In addition to including 2X more redox-center in PPTS, a couple of critical parameters in designing half-cells cause the superior cyclability of PPTS vs. PAQS (e.g., 3000 cycles @ 5000 mA g⁻¹ vs. 200 cycles @ 200 mA g⁻¹). These parameters are:

- 1) The consumption of different electrolyte formulations. To evaluate electrochemical properties of PPTS, 1 M KPF₆ in DME was exploited, showing a better performance. This superior performance in comparison to the 0.5 M KTFSI in DME:DOL is due to the lower energy level of DME (2.532 eV) vs. DOL (3.049 eV), providing a better match for the LUMO level of PPTS and DME-based electrolyte.
- 2) The inclusion of more carbon nanofiller in the production of the PPTS composite electrodes 40 vs. 20 wt. %. (35,36)

2.6.2 An imino (-NH-) linker group

Polyaniline (PANI) is a fascinating pioneer *p*-type polymer synthesized via linking (-NH-) group to an aromatic chain. Based on this route, polymerization occurs through chemical or electrochemical oxidation of amino-containing quinone-based monomers. As for PANI, the presence of the light molecular weight (-NH-) group provides benefits such as high C_{theo} , high average reduction potential (3.1 V, 1e), and optimum electronic conductivity from the main chain of the structure. (37) However, the synergy of carbonyl and amine groups in polydiaminoanthraquinones (PQs 1-3) results in *n*-type polymers with a reduced average reduction potential. For example, the incorporation of pendant multi-redox centers increases the probability of dissolution of (PQs 1,2) active material in the electrolyte, leading to capacity decay. Nevertheless, further polymerization enables (PQs 3) to show better cyclability (200 cycles @ 250 mA g⁻¹ with capacity retention ~ 91%). (38)

The disadvantage of such a synthesis pathway is the difficulty of controlling the degree of doping. For instance, poly(*o*-phenylene diamine) (PoPD) with plenty of redox-active centers and conjugation was synthesized using a high ratio of phenylene diamine and (NH₄)₂S₂O₈, cycling stable for 200 cycles at a high current density (2 A g⁻¹). (39)

2.6.3 Other organic electrode materials

The main objective of energy storage research, particularly organic-potassium batteries, is to prolong the lifespan of batteries. However, the cyclability of lightweight

small molecules is hindered because of dissolving in electrolytes. Therefore, circumventing the bottleneck of solubility has always remained a challenge. In addition, insufficient reversibility, volume changes (especially for inorganic materials), and structural transformations (especially for inorganic materials) are also potential factors determining cycling performance. For example, the highest cyclability (50 cycles) was observed in organic small molecules containing quinoid moieties (Copper-tetracyanoquinonodimethane) (CuTCNQ) and benzoquinone-tetrathiafulvalene triad (Q-TTF-Q). (40, 41)

To solve the aforementioned issues, various approaches have been proposed. For instance, quinone salts with -ONa and $\text{-SO}_3\text{Na}$ polar groups showed reduced solubility in organic electrolytes and improved Li storage performance. Zhao's group explored para-disodium-2,5-dihydroxy-1,4-benzoquinone ($p\text{-Na}_2\text{C}_6\text{H}_2\text{O}_6$) and the ortho-di-sodium salts of tetrahydroxyquinone ($o\text{-Na}_2\text{C}_6\text{H}_2\text{O}_6$) as novel electrode materials for PIBs, and they displayed specific capacities of $190.6 \text{ mA h g}^{-1}$ at 0.1C ($1\text{C} = 248 \text{ mA g}^{-1}$) and $168.1 \text{ mA h g}^{-1}$ at 25 mA g^{-1} , respectively. (42)

For organic materials to be competitive with inorganics, one has to develop synthetic strategies to enhance K-ion uptake. Given that the large K-ion uptake of the majority of reported inorganic electrode materials has challenges such as adverse volume change upon (de) intercalation of K-ion, causing structural deformation and, thus, capacity decay. Researchers may take into consideration the advantages of organic materials, which are:

- i) The structural diversity;
- ii) Versatile designability;

iii) More importantly, ignorable volume change upon battery cycling. (42)

Despite the listed benefits of organic materials, one should design strategies to address inferior power density, capacity, and cyclability. (42) According to the works of literatures, some approaches have been developed to tackle these issues. We explain these approaches in what follows:

Firstly, one approach is the modification of the molecular structure of organic material from an amorphous shape to a crystalline one, e.g. lamellar morphology. It is reported that a lamellar tetra potassium pyromellitic (K_4PM) with four functional C=O groups has a decent cycling performance with a high gravimetric capacity of 223 mAh g^{-1} @ 5C. (43) Introduction of potassium into the structure can boost the tap density due to its heavier atomic weight and density in contrast to the lightweight elements such as C, N and S, which are the main components of carbonyl-containing organic materials. (43)

Secondly, Lee et al. reported a series of PTCDA-based electroactive materials. They made these through polycondensation between 3,4,9,10-perylene-tetracarboxylic acid-dianhydride (PTCDA) and alkyl diamine. A couple of tactics have been implemented to improve simultaneously power density. This correlates with the materials synthesis and usage of super-concentrated electrolyte (5 M KTFSI in DME.) in the half-cells design. The former is achievable by shortening the attached alkyl chain linkers (discharging <10s @ 147C rate) while the latter is improved via the consumption of concentrated electrolyte to reduce the dissolution of active materials (presenting 1000 cycles @ 7.35C). (44–46)

Thirdly, Kapaev et al. reported that the substitution of the exocyclic bonds with heterocyclic bonds in triquinoxalinylene (TQY) small molecule and polymerization of this

suppress the dissolution of hexaazatriphenylene (HAT). (47) The reported impressive electrochemical performance of HAT, 169 mA h g^{-1} @ 10 A g^{-1} for 4600 cycles is because of the extended π -conjugated backbone and nano-sized (200-500 nm) its particles. However, the practical implication of such *n*-type cathode material in the real PIBs is not feasible due to inferior average discharge potential (1.6 V) at the potential range of 0.9-3.4 V. Finally, not only does synthesizing organic-potassium salt mitigate the dissolution of even small molecule, but also improve conductivity and enable its operation at elevated temperature (50 and 60 °C). For example, Wang et al. reported lamellar morphology-based azobenzene-4,4'-dicarboxylic acid potassium salts (ADAPTS). Although this strategy is effective in suppressing the shuttle effect (losing active materials in electrolytes), the average discharge potential (1.55 V in the range 0.5-3 V) is too high to utilize ADAPTS anode in the full-cell format. (48)

2.7 Dual-Ion Batteries

Scientists anticipated that the invention of conducting polymers in the 1970s would assist in reducing the incorporation of conductive nanofiller in the creation of composite electrodes and, generally, boosting the rate capability of batteries. (49) Nevertheless, the unexpected outcomes such as smooth charge and discharge profile, poor cycling performance, and fast discharging shocked scientists. As a preliminary example, polyaniline (PANI) presents 138 mAh g^{-1} at 10 mA g^{-1} with the support of a PMMA-based gel polymer electrolyte. There is improved cycling stability in comparison to the non-

aqueous-based electrolyte. However, the slopping charge and discharge profile stayed a challenge. This shortcoming is the result of the synergic effect of *p*-doping and storage mechanisms. It means that the shape of the charge and discharge profile depends on the amount of doping which modifies as battery (contains PANI electrode) proceeds in cycling. (50) Thus, to diminish the electronic impact of functional groups on the rigid backbone, researchers proposed a design of an unembedded redox center from the π -conjugated backbone. (51) For instance, non-planar and highly cross-linked poly(triphenylamine) (PTPAn) is a type of arylamine compound, with an anion insertion-type mechanism where nitrogen plays the role of the active center, which is not embedded in the π -conjugated backbone. Hence, the expected C_{theo} (111 mAh g⁻¹) is less than that of PANI. In contradiction to PANI, PTPAn does not suffer from voltage issues with conductivity in the doped state as high as 10 S cm⁻¹. (52) The gravimetric capacity of investigated PTPAn shows 100 mAh g⁻¹ (90% of C_{theo}) with the average K reduction potential of 3.3 V in the voltage range of 2-4 V. (52). It seems that the porous structure of polymer paves the way for anion penetration to compensate oxidation of the central N atom.

The incorporation of a couple of redox centers (N atoms) with the aim of improving theoretical capacity (209 mAh g⁻¹) was reported by Phillip Obrezkov et al. poly(N,N'-diphenyl-p-phenylenediamine) (PDPPD) possess the similar structure as PTPAn. Despite the improved discharge potential (3.5 V) in comparison to the PTPAn (3.23 V), the gravimetric discharge capacity (63 mAh g⁻¹) requires to be further optimized. (52)

The other type of *p*-type cathode traditionally examined as a hole transport layer in optoelectronic devices is poly(*N*-vinylcarbazole) (PVK). Redox-active centers in PVK are

not embedded in the main aliphatic backbone. Because of this, the doping level has no influence on the redox potential. PVK delivers the acceptable gravimetric capacity of 117 mAh g⁻¹@ 20 mA g⁻¹ which is 85% of C_{theo.} (54)

Polydiphenylamine (PDPA) is another cathode material with some characteristics that correspond to practical inorganic cathode materials. PDPA has a cation stabilization center because of the connection of a couple of phenyl rings to the central N atom. The energy density of PDPA is optimized up to 462 Wh kg⁻¹ in K half-cell. (55) Polycondensation of dihydrophenazine with diphenylamine produced PDPAPZ. This new molecular structure with a reduction potential of ~ 3.55 V in potassium half-cell demonstrated an energy density of 398 Wh kg⁻¹ at current density of 5 A g⁻¹. (56)

2.8 B-type electrode materials

Nitroxides are the building blocks of this class of organic materials. Nitroxides incorporated in the functional organic material can produce *n*-doped aminoxyl salts (Fig 2.8a) and *p*-doped oxoammonium salt (Fig. 2.8b) upon reduction and oxidation, respectively. TEMPO can be considered a paradigm manifest of B-type polymers.



Fig. 2.8 *n*-doped aminoxyl salt (a) *p*-doped oxoammonium salt

Nakahara et al. implemented a TEMPO redox-active group in poly (2,2,6,6-tetramethylpiperidinyloxy-4-ylmethacrylate) (PTMA), demonstrating $C_{\text{theo}} = 111 \text{ mAh g}^{-1}$ ($1e^-$) with an average potential $\sim 3.6 \text{ V}$. (52) Unfortunately, adverse electrical conductivity and solubility of PTMA in Li cell are main obstacles for practical application of PTMA. These issues might be circumvented by modifying the synthesis process such as cross-linking and increasing aromaticity or grafting with carbon nanotube (CNT). (52) However, there is no report corresponding to the usage of PTMA in the K cell. The molecular structures of all discussed organic redox-active materials are presented in Fig. 2.9.

2.9 Potassium metal: a member of alkali metal anode

To pair with high-capacity cathode materials, the pursuit of alkali-metal (Li, Na, and K) anodes is becoming a necessity for the development of high-energy batteries.

To evaluate the electrochemical performance of synthesized materials, one needs to adjust the achieved material with the alkali-metal (Li, Na, or K) anode. Hence, we summarized the physico-electrochemical properties of alkali metals and other (di)/trivalent elements in Table 2.1. (14,57)

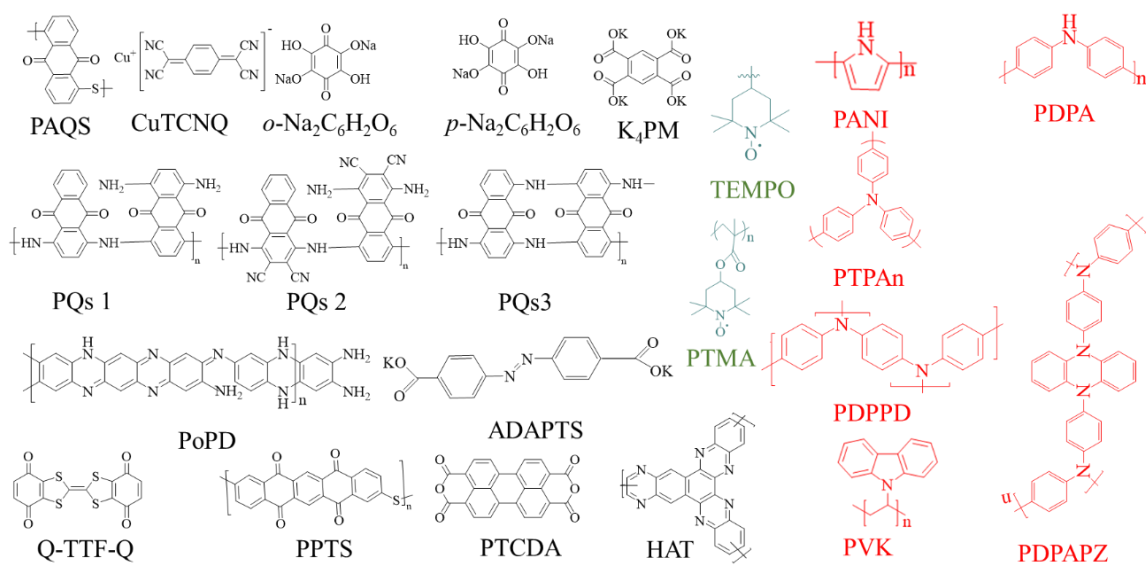


Fig. 2.9 All molecular structures discussed above. a) *n*-type organic materials (black colour) b) bipolar (dark green colour) c) *p*-type (red colour).

Table 2.1 Physico-electrochemical properties of alkali metals and other (di)/trivalent elements in metal-ion batteries (14,57)

Electrode	C _{theo} (mAh g ⁻¹)	Deposition potential vs Li/Li ⁺ (V)	Density (g cm ⁻³)
Li	3861	0	0.53
Na	1166	0.34	0.97
K	685	0.12	0.89
Mg	2205	0.67	1.74
Ca	1337	0.18	1.55
Zn	820	2.28	7.13
Al	2980	1.38	2.7

2.10 Carbon-based anode materials

2.10.1 Graphite

Graphite (G) is formed when honeycomb graphene layers are stacked on each other known as “Bernal stacking” (Fig. 2.10a) with an interlayer distance of ~ 0.335 nm. (58) Ji

et al proposed the intercalation/deintercalation mechanism for K-ion storage in a non-aqueous medium, using 0.8 M KPF₆ in EC: DEC. (59) When completely intercalated with K-ion, graphite delivers capacity ~ 279 mAh g⁻¹ with a volume change of ~ 60 %. Operando X-ray diffraction (XRD) shed some light on the mechanism of ion storage and the structural instability of graphite upon uptaking K-ions. The K-ion storage mechanism of graphite consists of three stages at different potentials consistent with the XRD data. At stage iii where G stores 36 K-ions (Fig.2.10b), in the potential range of ~ 0.2-0.3 V (Fig 2.10c), a couple of peaks at 22.00° and 29.40° (Fig. 2.10d) appear following the disappearance of intense G's peak at 2 Θ ≈26.70°. The peaks at 2 Θ ≈20.20° and 2 Θ ≈30.60° confirm the phase transition from KC₃₆ to KC₂₄. Discharge to the lower potential (0.01 V) and 0 V cause KC₈ and G phases, respectively. Unfortunately, less intense peaks upon (de)intercalation corroborate damage to the crystal structure. Unfortunately, G has disadvantages such as poor cycling stability despite its ubiquitous usage in LIBs. Several feasible approaches exist to tackle the highlighted issues. Firstly, Feng et al designed and synthesized the expanded graphite (EG) with a large interlayer spacing in order to accommodate bulky K-ions. Hence, this way boosts gravimetric discharge capacity to 273 mAh g⁻¹ @ 10 mA g⁻¹. In addition, EG is stable with almost no capacity fading for 500 cycles @ 200 mA g⁻¹. (60) In another approach, Pint et al. recommended nitrogen doping of G to provide more active sites for intercalating more K-ions. However, this method cannot solve the volume expansion problem of G. (61)

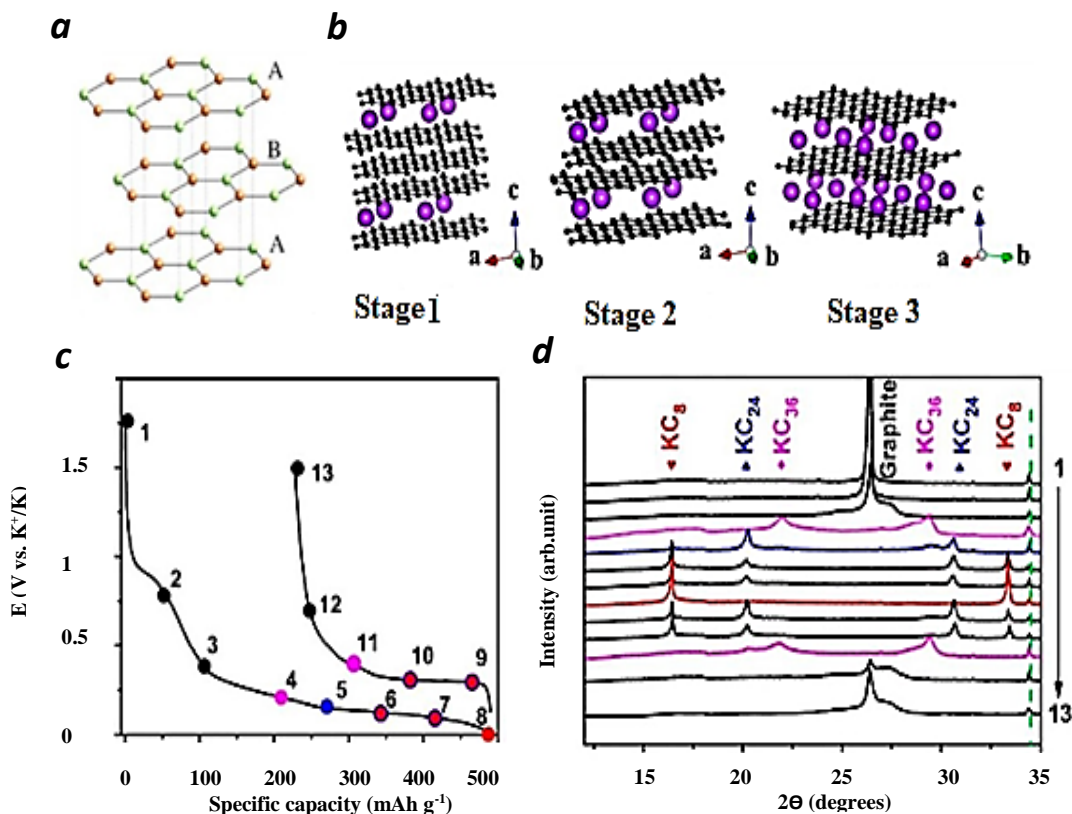


Fig. 2.10 AB Bernal stacking schema of graphene (a), triple stages of K-ion storage in graphite (b), the first charge and discharge profile of G||K at the current density of 27.9 mA g^{-1} (c), waterfall XRD pattern of G||K during discharge and charge (d). (159)

2.10.2 Soft carbon

To explore alternative carbon-based materials with enlarged interlayer spacing, Jian et al. reported soft carbon with an almost amorphous structure with some degree of graphitization degree when the $T > 2000 \text{ }^\circ\text{C}$ is implemented during the synthesis process. (58) The presence of graphitization inside the structure improves conductivity and the non-crystalline part of the structure ensures cycle and rate performance of soft-carbon as

explored in K half-cells because of better compatibility of soft carbon and electrolyte. For example, the capacity of PTCDA-derived soft carbon delivers 140 mAh g⁻¹@ 5C while G is not functioning at the high current rate. (62)

2.10.3 Hard carbon

Hard carbon (HC) consists of a disordered amorphous morphology and graphitic domains possessing spacious layer spacing, accommodating more K-ion, and it resists graphitization even at temperature (T)>2000 °C. Jian et al were the first to investigate the K⁺ uptake of HC, showing superior diffusion coefficients compared to Na⁺. (63)

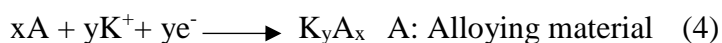
HC has an inappropriate ICE (e.g. 36.68 % when the synthesis T is 900 °C) and adverse rate capability, hindering the technological feasibility of HC as an anode. (64) These issues emerge from a large specific surface area as well as structure defects corresponding to the graphitic stacks of HC. (65)

Ghimbeu et al investigated the impact of T in the hydrothermal synthesis on the electrochemical and physico-electrochemical of HC in contrast to the ICE of commercial graphite (Gr-SLP 30). Regarding ICE, this study presents that HC prepared at T=1700 °C (further denoted as HC1700) has ICE=62% which is superior to HC1500 (ICE=54%), HC1900 (ICE=51%), and Gr-SLP 30 (ICE=43%). Nevertheless, raising the T does not improve the rate performance of ICE1700. For example, HC1500 presents 230 mAh g⁻¹ at 10C rate, while HC1700 and HC1900 demonstrate 228 and 214 mAh g⁻¹ at identical C rate.

They claim that the reason might be due to interlayer spacing between graphene and defects in the structure of HC1500. (66)

2.11 Alloying materials

Elements from groups IVA and VA, as well as their related intermetallic compounds of the periodic table, have caught the attention of researchers due to their high theoretical capacity, which is comparable even to metallic potassium. The reported elements are Si, Ge, Bi, Sn, Sb, Pb, and P with the general mechanism shown in equation 4.



Nevertheless, such elements do not fulfill the requirement for anode materials because of huge volume variation. Such compounds suffer from the adverse expansion of unit cell volume and poor electronic conductivity, e.g. particularly in the case of red and black P, leading to improper cycling performance. (67) Table 2.2 summarizes the electrical conductivity and C_{theo} of alloy-based materials. Some of these elements are capable of alloying with multiple K, endowing them with the advantage of a high C_{theo} .

There are several ways to solve problems corresponding to the volume variation of alloy-based anode materials. Firstly, scientists reported on the nanosizing and carbon coating of active alloy-based materials. For instance, a sonoelectrochemistry synthesis route is implemented to achieve nano-size Bi from bulk in order to buffer the volume change.

Although success has been achieved in the development of K-ion storage properties (delivering gravimetric capacity $\sim 200 \text{ mAh g}^{-1}$ @ 20 mA g^{-1} after 2500 cycles), inferior

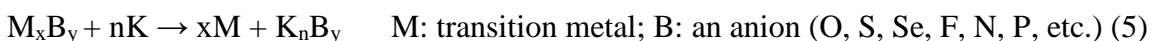
Table 2.2 Initial alloying materials with their conductivity and final alloying product with associated theoretical capacity. (68)

Initial material	Electrical conductivity (S m^{-1})	Final alloying material	C_{theo} (mAh g^{-1})
Si	$< 10^{-1}$	KSi & $\text{K}_{1.1}\text{Si}$	955 & 1049
Ge	2000	KGe	369
Pb	4.8×10^6	KPb	126
P	10^{-12} (RP) & 3×10^4 (BP)	KP & K_4P_3	865 & 1154
Sn	9.1×10^6	KSn	226
Sb	2.65×10^6	K_3Sb	660
Bi	7.7×10^5	K_3Bi	385

initial coulombic efficiency is obtained because of the enhancement of the interface between Bi nano-particles and electrolyte, which increases the risk of SEI formation detrimental to the practical usage of such material. (69) Another commonly applied tactic is producing a heterostructure or binary alloy. With this method, some percentage of volume variation may be diminished. For example, Bi possesses a large interlayer spacing in the *c*-direction (3.95 \AA bigger than K-ion size), which has the potential to store large K-ion. However, the low C_{theo} hinders the usage of Bi in batteries. To optimize C_{theo} , one may synthesize a binary alloy with Sb to improve C_{theo} . As a result of implementing this way, the volume expansion becomes 22% less in the case of K_3Bi (406%). (70)

2.12 Conversion Materials

These types of materials do not require large cavities to host K-ions. Instead, they have a large interlayer spacing that is considered a structural advantage for storing K-ion. Additionally, conversion-type compounds have a large C_{theo} due to the nature of the ion storage mechanism. Nevertheless, both alloying and conversion compounds have a common challenge upon the release and uptake of K-ions. The same approaches used for alloy-type materials are applicable to these anode materials as well. (71) According to equation 5, conversion-type compounds store K-ion in the transition metal separate, and K-ion establishes a bond with the anion part.



2.13 Polyanion compounds

To tackle with bottlenecks related to improper structural integrity, robust 3D structures referred to as polyanion compounds are synthesized and introduced. This class of compounds constitutes a combination of tetrahedra $[(XO_4)^{n-}]$ or $(X_mO_{3m+1})^{n-}$; X = P, S, W, As or Mo] and polyhedra [(MO); M = transition metals]. Tetrahedra-containing electronegative groups are strong enough to establish ionic bonds with oxygen and bridge neighboring polyhedra groups, creating cavities to accommodate alkali ions. The ionization of bonds can be strengthened by exploiting the “inductive effect” through the introduction of F⁻ into the 3D polyanion-based structure.

Hence, the general formulation $AMXO_4L$ [$A = \text{Li, Na, K}$; $M = \text{Fe, Ti, V}$; $X = \text{P, S, Si}$; $L = \text{O, F, OH}$] belongs to the KTiOPO_4 (KTP) structural class where the M-O-X anionic network is embedded in XO_4 tetrahedra and MO_6 octahedra forming a helical chain (Fig. 2.11). This type of 3D open structure possesses channels in the b direction with activation energy ~ 0.52 eV to facilitate K-ion exchange. (72)

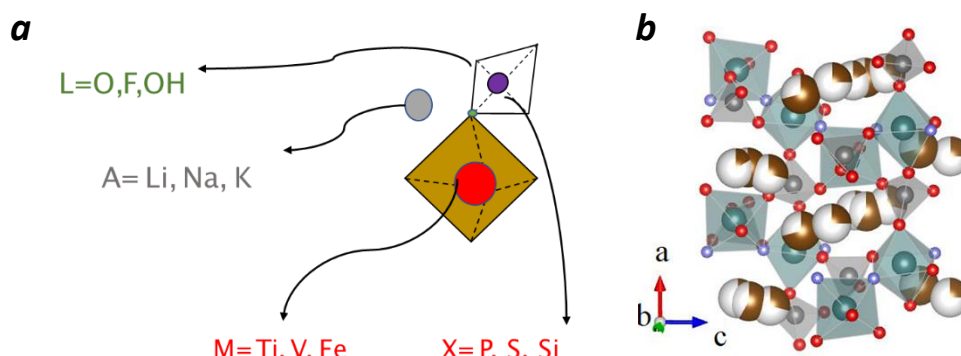


Fig. 2.11 A schematic representation of connected octahedron and tetrahedron with the possible embedded elements in the KTP structure (a) and a 3D image of the KTP structure projected along the $[010]$ direction (b).

The fascinating feature of the KTP structure is the incorporation of Fe, Ti and V as core redox centers, enabling the implementation of such a material as cathodes and anodes. This is because the versatile oxidation states of central transition metal allow for the assembly of a full symmetric battery. Full symmetric batteries refer to a type of battery where the aforementioned materials are applicable as positive and negative electrodes. For example, M (Ti and V) utilizes the redox reaction of M^{2+} and M^{3+} when used as the anode, as well as M^{3+} and M^{4+} as applied as the cathode.

2.13.1 V and Ti-based polyanion anodes

The first V-based polyanion anode material is VPO₄. Fedotov et al first reported the intercalation-based α -VPO₄ adopting from the α -CrPO₄ structure. They synthesized VPO₄ through heat treatment of the precursor, NH₄VPO₄. Despite the large $C_{\text{theo}} \sim 550$ mAh g⁻¹, α -VPO₄ delivers 37 mAh g⁻¹ in K cell. (72) On the other hand, the conversion-based carbon-coated VPO₄-F (F stands for flower-like structure), synthesized by a reflux route, delivers ~ 400 mAh g⁻¹@ 50 mA g⁻¹. (73)

When V is exploited as the core redox center, the oxidation state variation from 3+ to 2+ may endow the anodic characteristic to KVPO₄F (KVPF). Considering this, Zhang et al. synthesized KVPF and characterized it electrochemically using 1 M KPF₆ in EC:PC in the potential window of 0-3 V. Electrodes containing 70 wt. % of KVPF delivered 105 mAh g⁻¹@ 100 mA g⁻¹ with 91% of capacity retention after 100 cycles. (74) The lowest volume variation (7.1%) among the KTP family has been observed in K_{0.76}V_{0.55}Nb_{0.45}OPO₄ (KVNP). Nevertheless, it is not recommended to implement KVNP for anode due to the low $C_{\text{theo}} \sim 97$ mAh g⁻¹. (75)

One may switch the redox center from V to other transition elements, e.g. Ti or Fe. Ti is an abundant transition element that can be exploited in aerospace, medical surgery, and energy storage. The latter application is due to the various oxidation states of Ti (2+, 3+ and 4+). Ti-based NASICON materials with a hexagonal structure refers to the family of compounds with high ionic conductivity. The structure constitutes the connection of six vertex-sharing tetrahedra with Ti-O octahedra. (76) As a manifest paradigm of this family, the phase transformation of KTi₂(PO₄)₃ between phase 1 (KTi₂(PO₄)₃, Ti³⁺) and phase 2

($\text{K}_3\text{Ti}_2(\text{PO}_4)_3$, Ti^{4+}) is responsible for K-ion storage. (77) Another approach to further improve the conductivity of such phosphates is by nano sizing and incorporating a carbon matrix. In this way, $\text{KTi}_2(\text{PO}_4)_3$ delivers 297 mAh g^{-1} in the potential range of 0.01-3V. (78) Qi et al, reported KTiOPO_4 as a workable host, cycling for 10000 cycles. In addition, KTiOPO_4 shows 176 mAh g^{-1} @ 30 mA g^{-1} . (79) Of course, the KTP structural anode comprising Ti and V would bring a fascinating result. Carbon-coated $\text{K}_{2.13}\text{V}_{1.52}\text{Ti}_{0.48}(\text{PO}_4)_3$ (KVTP) presented a superiority based on discharge capacity over $\text{KTi}_2(\text{PO}_4)_3@\text{C}$ and KVNP. KVTP presents 136 mAh g^{-1} @ 10 mA g^{-1} . (80) Recently, a MXene-derived carbon coated $\pi\text{-Ti}_2\text{O}(\text{PO}_4)_2$ with a low K ion migration energy of 0.23 eV and small volume variation of 9.18% showed promising K-ion storage properties delivering 134.5 mAh g^{-1} after 2000 cycles at 1.0 A g^{-1} . (81)

2.14 Concluding remarks

In summary, the introduction of novel organic, (none)-crystalline inorganic materials to mainstream PIBs is a rapidly evolving field. Generally, in this chapter, various anode materials ranging from organic to inorganic-based (carbon-based, conversion/alloying, and polyanion) materials have been analyzed and compared, highlighting the (dis)advantages of each material. Organic materials owing to liberty in the incorporation of distinct functional groups offer high gravimetric capacity and are cost-efficient, but have poor cycling stability, solubility, and inferior active mass loading that impede further implementation of these materials in the battery landscape. Although

carbon-based materials endow advantages of decent cyclability, the energy-consuming synthesis process, and the structural integrity remain challenges. Despite the high gravimetric capacity of alloying-type anodes, volume variation leads to capacity fading upon cycling. Likewise, conversion-type anodes have high capacity but suffer from poor reversibility and low cycling stability. As a high-capacity anode, metallic potassium anodes possess medium C_{theo} but are highly reactive with electrolytes with a fire hazard. The outer layer of alkali metals, such as lithium Li, Na, and K, is known to develop an oxide coating, primarily composed of K_2O with a layer of KO_2 on top. Notably, the oxide layer on K is more porous compared to that on Li and Na, even when potassium is handled with care within an argon (Ar)-filled glove box. An additional challenge associated with using metallic potassium is its strong propensity to develop dendrites when it comes into contact with the electrolyte. This is particularly concerning as the onset of dendrite formation occurs at a remarkably low crossover current, as low as 0.2 mA cm^{-2} . This behavior is likely attributed to the relatively high self-diffusion coefficient of potassium compared to Li and Na. To sum up, the selection of anode materials highly relies on specific application requirements such as capacity, stability, cost, and safety. It is recommended further exploration to optimize the performance of these materials for practical implementation in PIBs.

Chapter 3

For an extended period, the integration of organic materials into metal-ion battery technology has posed substantial challenges. Organic materials are prone to dissolution in carbonate and ether-based electrolytes, with carbonyl-containing organic materials being particularly susceptible. Their performance is hindered by lower tap energy density, reduced conductivity, capacity degradation, and suboptimal ICE. In this context, we introduce 11 novel organic redox-active materials within the carbonyl-containing family, widely recognized as one of the most formidable classes of organic materials. Our goal is to address the longstanding challenges that have persisted since the 1980s. To achieve this, we have established the following research objectives and detailed research flow chart (Fig 3.1):

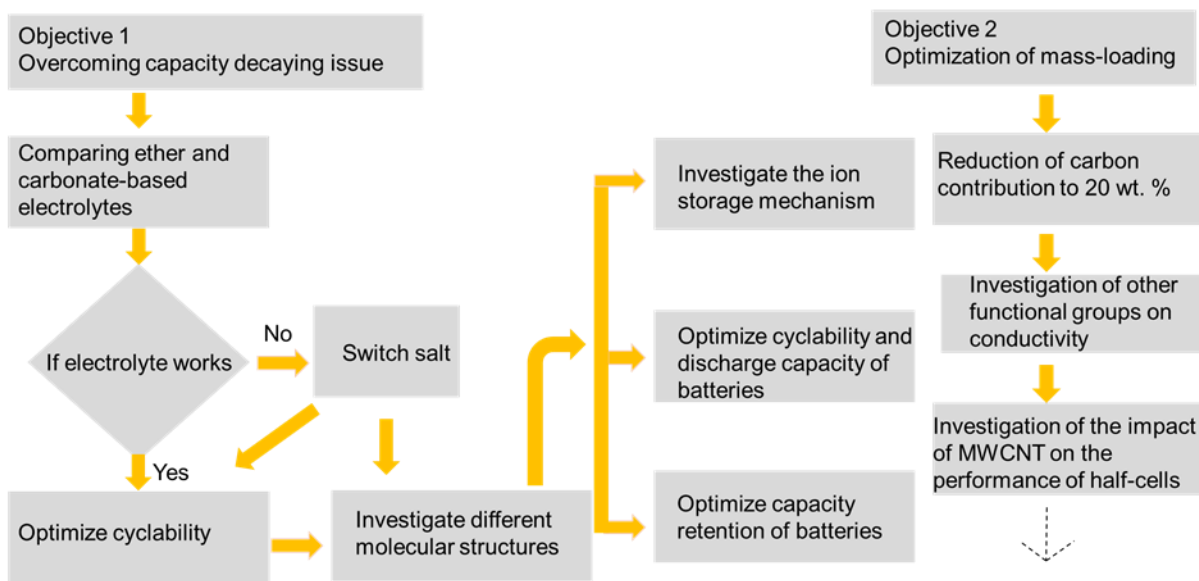
3. Thesis objectives

Aim: Design of advanced K-ion batteries using organic redox-active materials.

Objectives:

- Characterization of the organic carbonyl-containing small molecules and polymers;
 - Tetraazapentacene-based redox-active materials;
 - Polymers derived from triquionoyl;
 - Rigid backbone quinone-based polymers

- Electrochemical characterization of the materials in half-cells with K-anode (cyclic voltammetry, galvanostatic charge/discharge, etc.);
- Investigation of proper electrolyte formulation to match well with metallic potassium;
- Exploring K-ion storage mechanism of carbonyl-containing materials by means of:
 - X-ray photoelectron spectroscopy (XPS);
 - Fourier Transform Infrared Spectroscopy (FTIR).
- Optimization of the electrodes in order to reach the highest capacity and the best charge-discharge cycling stability.



- Optimization of the electrode composition and mass-loading.
 - Replacing carbon super P with MWCNT.

Fig. 3.1 Research methodology flow chart

Chapter 4

4. Methodology and techniques

Organic redox-active materials were synthesized in the Institute for Problems of Chemical Physics, Russian Academy of Sciences. Quinoxalino[2,3-b]phenazin-1,2,3,4,8,9,10,11-octaol or octahydroxytetraazapentacene (**OHTAP**), octahydroxytetraazapentacenedione (**OHTAPQ**), and **P1-P6** were synthesized by Dr. Igor K. Yakuschenko. **P7-P9** were provided by Dr. Alexey Kozlov. The synthesis process as well as the characterization of these materials are elaborated in Appendices A.

4.1 Assembling of potassium half-cells for polymers

Coin-type cells (CR2032-Fig 4.1a) were used to characterize electrochemical properties. The positive electrodes were prepared in the following way. The PVDF binder (20 mg, Gelon Lib) was stirred with 1.5 mL of N-methyl-2-pyrrolidone (NMP) for 30 min. Then, well-grinded active material (one of the organic redox-active materials, 100 mg) and conductive filler (80 mg, super-P, Gelon Lib) were added to the PVDF in NMP. The mixture was stirred at room temperature for 12 h and the resulting slurry was cast on Al/C foil (Gelon Lib) by an automatic tape coating machine (Fig. 4.1b) and dried for 8h inside the vacuum oven. The active mass loading for all polymers was $\sim 0.3 \text{ mg cm}^{-2}$ (except when stated otherwise). To assemble the batteries, well-dried round-shape ($d=16 \text{ mm}$) composite

electrodes were transferred into the Ar-filled MBraun glove box (H_2O and $\text{O}_2 < 0.1$ ppm). The negative electrodes were prepared by pressing well-washed metallic potassium (150-170 mg) on a steel spacer (2 cm²). Glass fiber filter (WHATMAN, 1 layer) was used as a separator. Then, 120 μL of the electrolyte represented by the 2.2 M solution of KPF_6 in G_2 was applied to the steel spacer. It should be mentioned here that in the case of **OHTAP** and **OHTAPQ**, 1 M KTFSI in DOL:DME (1:1, v/v) was used to evaluate K-ion storage properties.

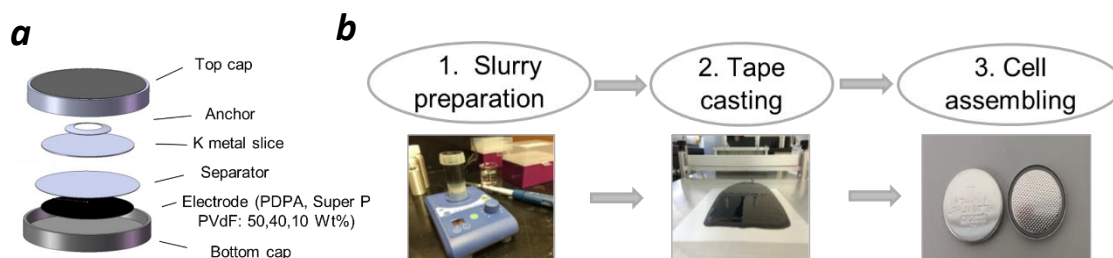


Fig. 4.1 schematic representation of half-cell (a) and Electrode preparation process (b).

Half-cells were cycled repeatedly within the voltage window of 0.7-4 V (except when stated otherwise). The fabricated potassium half-cells were characterized by potentiostatic measurements (cyclic voltammetry) using the Biologic VMP3 instrument and by galvanostatic measurements (charge-discharge cycling) using the battery analyzer BTS-5 V (Neware Technology Ltd.). Before performing the final measurements, the cells were preconditioned in a galvanostatic regime at the current density of 0.5 A g⁻¹ until the specific capacity value was stabilized. The initial evolution of the specific capacity was attributed to the SEI formation and electrode activation. Typically, such preconditioning required several tens or even hundreds of cycles (depending on the material activation behavior).

4.2 Potassium battery fabrication by spray-coating

For OHTAP, we are exploring spray coating to control thickness, uniformity, and adhesion to the Al current collector. However, for the other materials, we are exclusively investigating tape casting.

The electrode composite was prepared using 50 wt. % of **OHTAP** active material, 40 wt. % of Super P conductive filler and 10 wt % of PVDF binder all dispersed in NMP. The slurry was mixed with a homogenizer for 30 min and spray coated on an Al foil and dried at 70 °C under vacuum for 14 h. The electrodes were cut into 16mm diameter circles and dried at 110 °C for 1 h. Coin cells were assembled with potassium foil as the counter/reference electrode, a whatman glass microfiber separator, and 1 M potassium bis(trifluoromethane sulfonyl)imide (KTFSI) in mixed 1,2-dimethoxyethane/ dioxolane solution (DOL:DME = 1:1 v/v) as an electrolyte (120 µl per cell). The active mass loading was ~ 0.1 mg cm⁻². The cells were cycled within the voltage range of 1.1-3.1 V.

4.3 Pre-potassiation of organic materials

Solution-based pre-potassiation is a straightforward technique used to investigate the uptaking of metallic potassium by functional groups. In this method, the composite is treated with potassium naphthalene, leading to a discernible change in the solution's color as the reaction progresses. Subsequently, the reacted electrodes are examined using FTIR to compare their spectra with those of pristine organic materials. This approach offers the

advantage of bypassing the arduous process of extracting electrodes from cycled coin-type cells.

A dry and clean piece of potassium (90 mg) was dissolved in 0.25 M solution of naphthalene in diglyme (1 mL) to obtain a dark green solution. Pristine electrodes, containing 90 wt. % of the active material and 10 wt. % of carboxymethyl cellulose (CMC) binder were soaked in the resulting solution (1 mL) for 12 h. Afterward, the electrodes were washed 3 times with dimethoxyethane (5 mL each time) and dried in a vacuum antechamber. All the aforementioned procedures were performed in the Ar-filled glove box.

4.4 Material characterization

A Bruker ALPHA II spectrometer placed inside a nitrogen-filled glove box was exploited to measure FTIR spectra. The spectra are recorded in the range of 4000-400 cm^{-1} with a resolution of 2 cm^{-1} and 3 scans averaging.

The specific surface area was estimated from the nitrogen adsorption isotherm that was measured at the temperature of liquid nitrogen with a NOVA touch LX. The significant degassing step was done in a dynamic mode for a couple of hours at 300 °C. To calculate the specific surface area, the Brunauer-Emmett-Teller (BET) method, which is achievable from nitrogen adsorption data in the relative pressure ($P/P_0=0.05-0.30$). Scanning electron microscopy (SEM) images of polymers were obtained using a ZEISS LEO SUPRA 25 instrument.

X-ray photoelectron spectroscopy (XPS) core-level measurements were performed using a PHI 5000 Versa Probe XPS spectrometer (ULVAC Physical Electronics, USA) based on a classic X-ray optic scheme with a hemispherical quartz monochromator and an energy analyzer working in the range of binding energies from 0 to 1500 eV. The apparatus uses electrostatic focusing and magnetic screening to achieve an energy resolution of $\Delta E \leq 0.5$ eV.

Chapter 5

5. Design of potassium batteries using organic redox-active materials

5.1. Introduction

The interest of researchers to investigate organic redox-active materials has been increasing rapidly within the last few years due to the impressive characteristics they showed in metal-ion and redox-flow batteries. (82-84) The concept of using organic compounds as electrode materials for batteries emerged more or less at the same time with the discovery of inorganic intercalation-type compounds. However, in view of the great success of inorganic materials in the late 1980s, their organic counterparts have been slower to develop. Moreover, inorganic anode and, particularly, cathode materials are approaching now the limit of their development with respect to the achievable specific capacitances and energy densities. (85) On the contrary, organic materials are emerging and have begun to show superior characteristics. (86-88) While inorganic materials still form a basis of industrial Li-ion technology, many research groups over the world work on the development of promising organic electrode components. Unfortunately, the practical implementation of the current generation of organic electrodes is hampered due to a number of issues. (87-90) A major challenge is related to the fact that most of organic materials undergo partial dissolution in the electrolyte, which is leading to the battery capacity fading during charge/discharge cycling. Another major issue is related to low

electrical (and often ionic) conductivity of organic materials, which is mitigated by adding considerable amounts (up to 60 wt. %) of conductive carbon filler at the expense of the battery capacity.

The next generation of organic electrode materials (both cathodes and anodes) should satisfy a number of requirements, particularly being completely insoluble in electrolytes, have intrinsically high ionic and electronic conductivity, show high capacities, and demonstrate excellent electrochemical stability. Batteries based on organic materials are expected to deliver both high energy and power densities, e.g., being capable of gaining a full charge and discharge in much less than 1 h. Finally, organic materials should be based on abundant, cheap, and easily produced redox-active compounds (82-84, 86-88).

Organic carbonyl compounds represent probably one of the most promising families of redox-active materials. (91) Armand et al. showed in 1997 that partially metallated polyoxycyclohexanes such $\text{Li}_2\text{C}_6\text{O}_6$ can be further reduced and loaded with lithium ions. (92) However, it was shown later that such compounds are unstable in air, while their cycling stability in batteries is very poor due to a high solubility in organic carbonate-based electrolyte. (93, 94)

The aforementioned issues can be resolved by using polymeric redox-active materials (95,96) or specific low molecular weight compounds featuring planar molecular structures and capable of efficient π - π stacking. Such properties can be potentially observed for derivatives of tetraazopentacenes, which have been first synthesized in the 1960s. (97,98) There are many research papers (99-102) and patents (103-106) reporting the application of tetraazopentacenes in organic field-effect transistors, diodes, and photovoltaic cells.

(107). Recently, a potential application of some tetraazopentacene derivatives as electrode materials for metal-ion batteries was declared in a patent, while no experimental verification has been reported so far. (108)

Here, we report the K-ion storage properties of promising compounds of the organic electrode materials (Fig. 5.1). Quinoxalino [2,3-b]phenazin-1,2,3,4,8,9,10,11-octaol or octahydroxytetraazapentacene (**OHTAP**), octahydroxytetraazapentacenedione (**OHTAPQ**), a series of a series of novel redox-active polymers (**P1-P6**) derived from triquinoyl, and a family of ladder-type quinone-based polymeric materials (**P7-P9**).

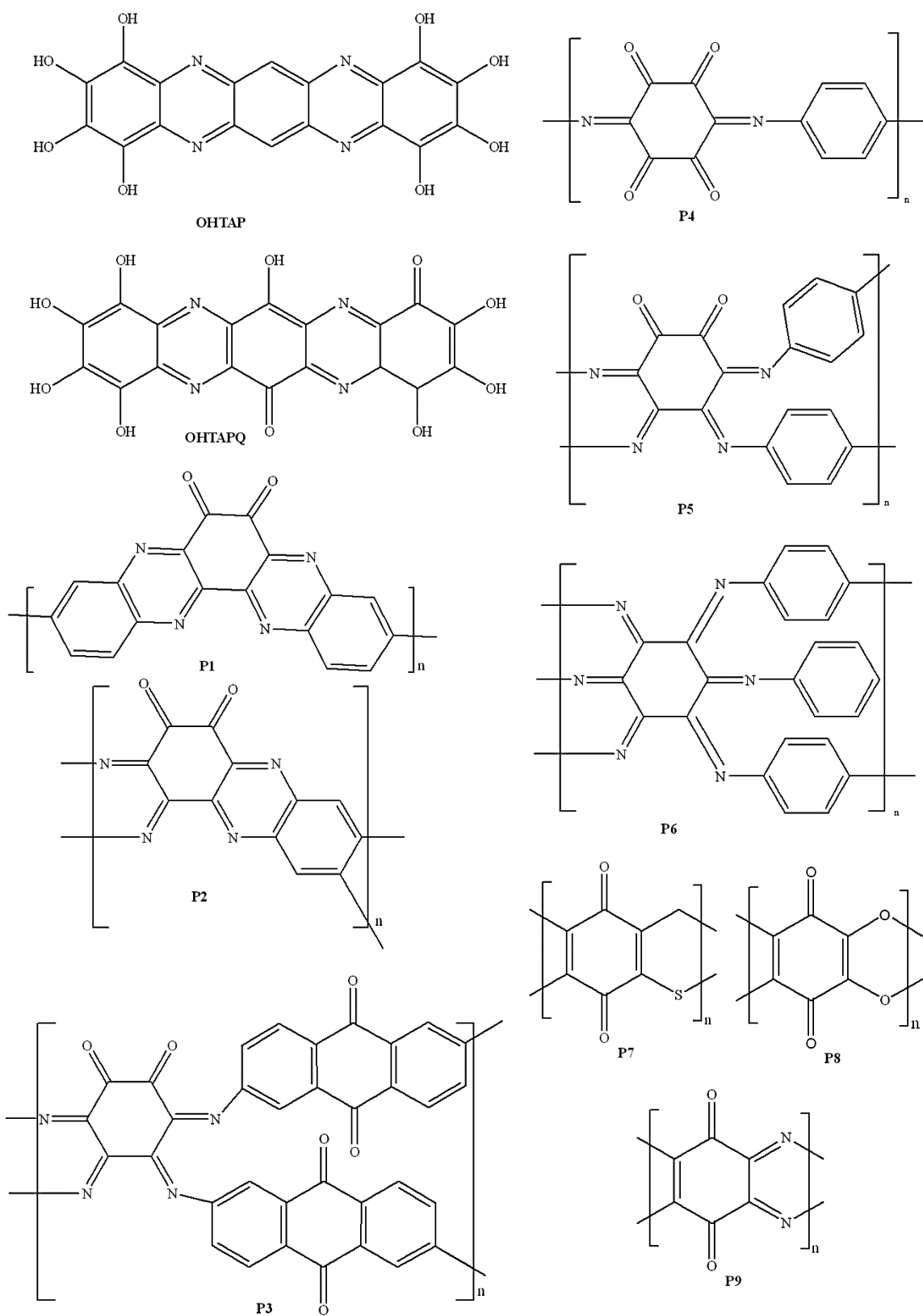


Fig. 5.1 Molecular structure of all investigated organic materials in this dissertation.

5.2 New tetraazapentacene-based redox-active material as a promising high-capacity organic cathode for potassium batteries

We have explored the potential of **OHTAP** as a cathode material for potassium batteries. The **K||OHTAP** cells were fabricated using either the tape or the spray coating of the slurry (**OHTAP**+Super-P+PVDF in NMP) on Al or Al/C current collectors. A 1 M potassium bis (trifluoromethanesulfonyl) imide (KTFSI) solution in dimethoxyethane and dioxolane mixture (DOL:DME = 1:1 v/v) was used as the electrolyte.

The charge-discharge characteristics of the **K||OHTAP** cells (Fig. 5.2) fabricated by tape coating of a thin layer of the cathode composite on Al foil show clearly that the first few cycles are associated with some irreversible processes, which are most probably related to the **OHTAP** conversion to its potassium salt **K-OHTAP**.

The SEI formation might also contribute to the irreversible capacity at the first cycles. The irreversible processes were accompanied by high coulombic efficiency (CE) exceeding 100% for the first ~ 10 cycles because of the formation of the **OHTAP-K** emanated from probably the consumption of none-transparent electrolyte and rapid dissolution of active materials (Fig. 5.2b). For subsequent cycles, the CE was slightly below 100%. It is known that half-cells with K anodes usually give CE <100% at relatively low current rates due to parasitic reactions induced at highly reactive metallic potassium. (109) It has been shown recently that this effect can be mitigated by a significant increase in the current density (36), which turned out to be challenging for **OHTAP**-based cells, which do not operate well at high current rates. The **K||OHTAP** cell capacity stabilized after 8-10 cycles at ~

220 mAh g⁻¹, which corresponds to ~ 50% of the theoretical capacity value. K⁺ ions are larger than Li⁺, therefore some steric hindrance effects might be responsible for the incomplete involvement of the **OHTAP** hydroxyls in the redox transformations with potassium ions under the battery cycling. It is very probable that only four K⁺ ions can occupy energetically favorable positions in the **OHTAP** framework.

In spite of the aforementioned limitation, the achieved practical capacity of 220 mAh g⁻¹ is already quite impressive for potassium batteries. To the best of our knowledge, it represents the highest value reported so far for potassium-ion storage in organic cathodes. (110-115) It is also notably higher compared to virtually all evaluated to date inorganic cathodes for potassium-ion batteries. (116,117)

Unfortunately, the cycling stability of the K||**OHTAP** cells was not very good and the capacity slowly decayed to ~162 mAh g⁻¹ after 50 cycles. We believe that the dissolution of the active material in the electrolyte is the main reason for such degradation. To mitigate the capacity fading, we used a carbon-coated Al foil as a current collector and applied thicker cathode composite films by spray-coating. This approach leads to a lower cell capacity of ~ 110 mAh g⁻¹ obtained at the first cycles at 1C current rate and the stabilized value of ~ 70 mAh g⁻¹ reached after ~ 25 cycles. These cells showed decent stability and maintained still ~ 50 mAh g⁻¹ after 500 charge-discharge cycles at 1C rate (Fig. 5.2c). The obtained results clearly show a high potential of **OHTAP** as organic cathode material for potassium ion batteries.

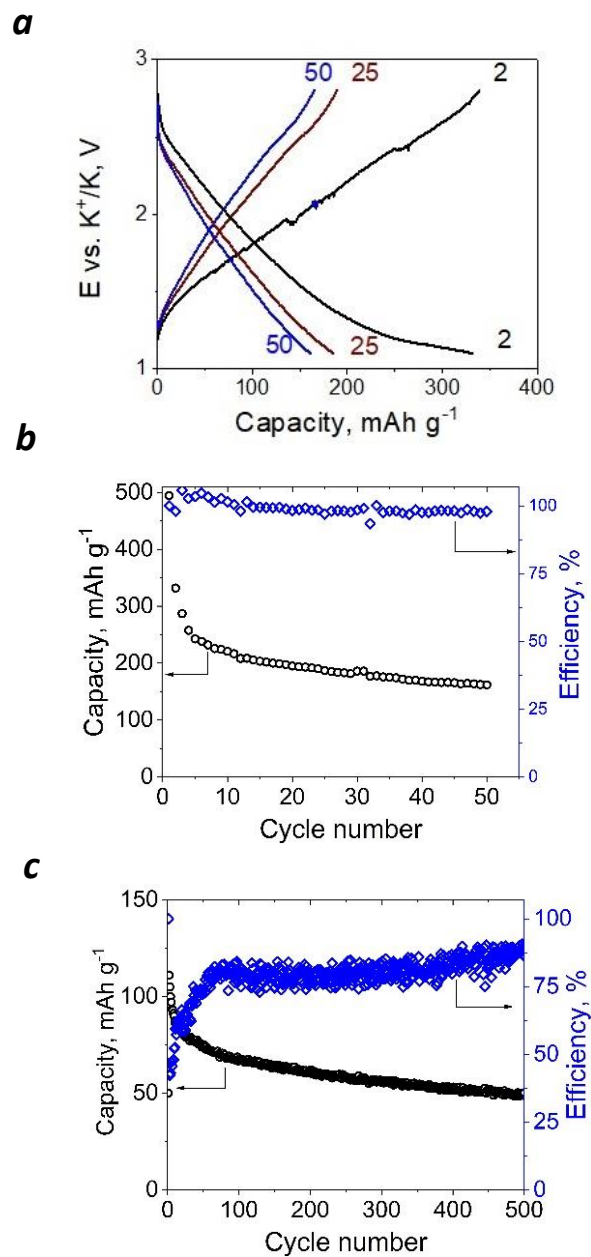


Fig. 5.2. The charge-discharge profiles (a) and cycling performance of K||OHTAP cells at C/10 current rate (cathode deposited on Al foil by tape casting (b). cycling performance of the K||OHTAP cells at 1C current rate (spray-coated cathode on Al/C current collector) (c). (The composite electrode formulations used in both deposition techniques are 50:40:10 wt. % of OHTAP: Carbon super P: PVDF and the electrolyte formulation is 1 M (KTFSI) in (DOL:DME = 1:1 v/v).)

5.3. Octahydroxytetraazapentacenedione: New organic electrode material for fast and stable potassium batteries

Many publications are addressing the application of organic redox-active materials (low molecular weight materials and polymers) as electrode materials in batteries. (118,119) Unfortunately, most low molecular weight compounds showed poor capacity retention because of the dissolution of the active materials in electrolytes. (40,112,114,119–121) Proper electrolyte selection has been considered one of the most promising strategies to overcome the aforementioned challenge. (122)

Glymes [R-(OCH₂CH₂)_n-OR] represent the main family of ether-based electrolyte solvents. Johansson et al. performed a systematic physicochemical study of different electrolytes in inorganic sodium-ion half- and full-cells. (47) It was found that 1 M sodium hexafluorophosphate (NaPF₆) in G₂ forms a stable solid electrolyte interface (SEI) with conventional electrode materials such as Na₃V₂(PO₄)₂F₃ and Na₃V₂(PO₄)₃. The application of G₂ as a solvent in the K-ion batteries was first reported by Zhang et al., who used 1 M KPF₆ in G₂ to stabilize the interface with the nanostructured bismuth-based anode materials in half and full cells. (123) The G₂-based electrolytes with different salt concentrations were used in inorganic PIBs. (124)

Previously, we showed that a similar tetraazapentacene derivative **OHTAP** represents a promising redox-active material for both lithium and potassium batteries. However, the practical capacity was relatively low and the cells rapidly degraded because of the active material dissolution. (120) Herein, we address these challenges by designing the next-

generation tetraazapentacene-based organic redox-active compound **OHTAPQ** having an impressive theoretical specific capacity ($C_{\text{theo}} = 852 \text{ mAh g}^{-1}$) and demonstrating a remarkable performance and cyclability when used as organic electrode material in PIBs. SEM was used to characterize the morphology of the composite electrode comprised of 50 wt. % of **OHTAPQ**, 40 wt. % of carbon super P, and 10 wt. % of PVDF binder. The obtained SEM image (Fig. 5.3) shows that the electrode features multiple nanosized grains and no big **OHTAPQ** particles, which is a proper morphology for the battery electrode ensuring a sufficient surface area, porosity, and ion penetration depth.

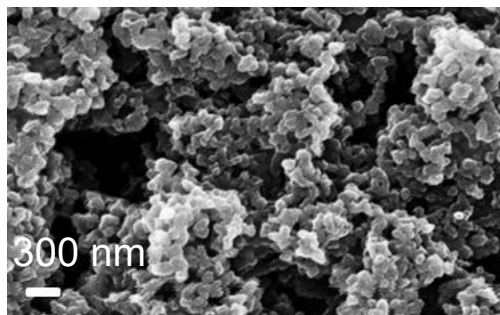


Fig. 5.3 SEM image of the composite electrode containing **OHTAPQ**.

To study the electrochemical behavior of the **OHTAPQ**-based electrodes, we fabricated the half-cells with potassium metal anodes. CV measurements performed at the scan rate of 100 mV s^{-1} reveal no evolution within 10 cycles as shown in Fig. 5.4a. A set of broad peaks between 1.68 V and 3.13 V (oxidation) and 1.48-2.5 V (reduction) characterize the redox behavior of **OHTAPQ**. Some conjugated polymers such as polyaniline, polypyrrole, and PEDOT-PSS exhibit similar broad redox reaction waves due to the presence of multiple reaction centers in each molecule. (53, 125,126) Indeed, **OHTAPQ** has 14 redox centers and, therefore, can behave similarly to conjugated polymers. We also recorded the

cyclic voltammograms for **OHTAPQ** electrodes at different voltage sweep rates to discriminate the contributions of the diffusion Faradaic processes and capacitive behavior to the overall energy storage in our cells. Following a standard approach, we plotted the logarithm of the peak current as a function of the logarithm of the voltage sweep rate and the slope of the obtained dependence provided us with the characteristics parameter b (Fig. 5.5). The estimated b value of 0.68 suggested that diffusion-type Faradaic processes are dominating in our devices, whereas the capacitive-type storage also plays an important role due to high conductive carbon filler loading. However, the **OHTAPQ** itself enables energy storage through the Faradaic redox processes, which justify its application as electrode material in PIBs. To further analyze the redox transition pathway of **OHTAPQ**, high-resolution O 1s and N 1s *ex-situ* X-ray photoelectron spectroscopy (XPS) was conducted on the pristine, potassiated and depotassiated electrodes. As shown in Fig. 5.4b-c, there are notable shifts of O 1s and N 1s bands to the higher binding energies when the cells are discharged (electrode material is reduced) and *vice versa* upon charging. These findings confirm that both C=O and C=N functional groups undergo reductive metallation when the cell is discharged and hence contribute to the K-ion storage in the **OHTAPQ**-based electrode. Such findings are consistent with the previous reports on the electrochemical behavior of LiOTAP and quinones or pyrazines in general. (120)

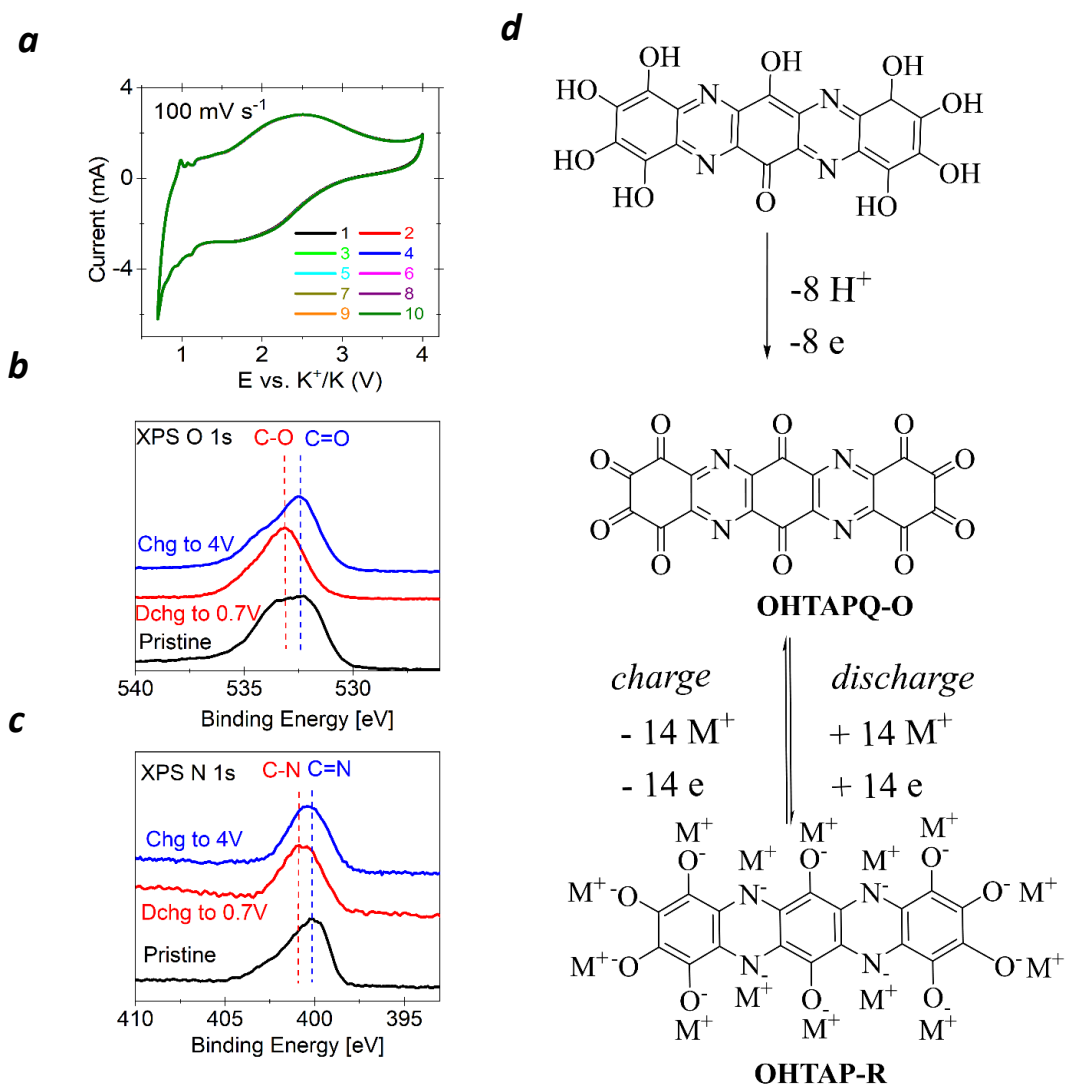


Fig. 5.4 Cyclic voltammogram of **OHTAPQ**||K cell with 2.2 M KPF_6 solution in G_2 as electrolyte recorded at the rate of 100 mV s^{-1} (a). The high-resolution core-level O 1s (b) and N 1s spectra of **OHTAPQ**-based electrodes in the pristine state, after the first discharge to 0.7 V and the first charge to 4 V (c). M-ion storage and release mechanism of **OHTAPQ** (d).

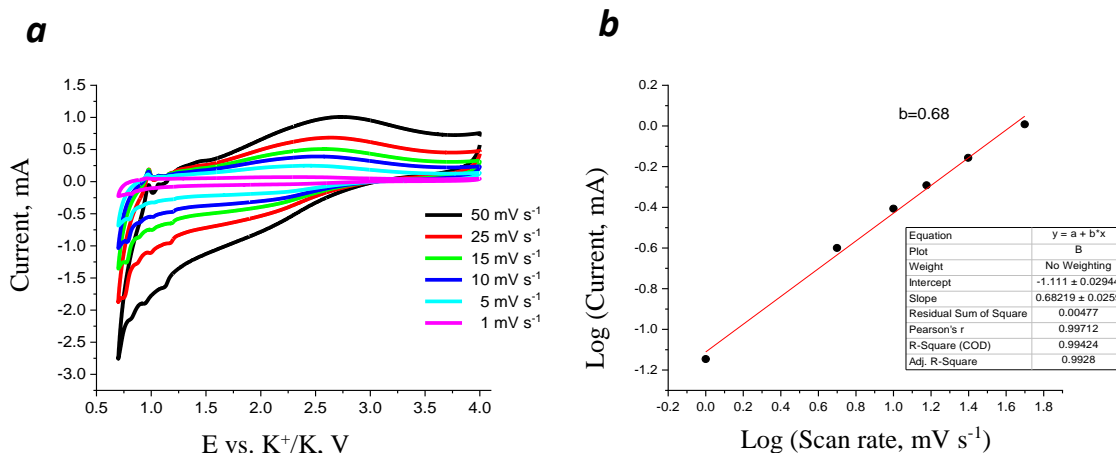


Fig. 5.5 Cyclic voltammograms recorded at different voltage sweep rates (a) and the power law dependence of the peak current on scan rate (b) used for the estimation of the parameter b.

Formally, the molecule of **OHTAPQ-O** possesses 14 redox-active centers, which could accommodate up to 12 ions of alkali metal and form a fully reduced state **OHTAPQ-R** as shown in (Fig. 5.4d). However, the incorporation of bulky K⁺ ions at some point would cause severe steric hindrances preventing further redox transitions and metallation of the fully oxidized form **OHTAPQ-O**.

K-ion storage properties of **OHTAPQ**-based electrodes were further evaluated by performing galvanostatic charge-discharge cycling after a certain preconditioning stage as described in the chapter of methodology and techniques (section 4.1).

First, we investigated the cells assembled with 1 M KTFSI solution in DOL and DME mixture (1:1 v/v) as electrolyte cycled at the current density of 0.6 A g⁻¹ within the voltage window of 0.7-4 V (Fig. 5.6a). The specific capacity initially approaches ~ 289 mAh g⁻¹ at the first cycles due to some irreversible reactions leading to the solid electrolyte interface (SEI) formation as can be concluded from low CE. However, the specific discharge

capacity then rapidly drops down to 114 mAh g⁻¹ after 60 cycles and then starts to increase back up to 200 mAh g⁻¹. At the last cycle, both the capacity and CE values become unstable due to the partially irreversible stripping/plating of the metallic potassium at the anode side, leading to dendrite growth. (109)

To address the aforementioned issue, we employed a concentrated G₂-based electrolyte (2.2 M KPF₆). The specific capacity and CE of the **OHTAPQ**||K half-cells assembled with the G₂-based electrolyte were stable for >1200 cycles recorded after the initial preconditioning at 1 A g⁻¹ for a number of cycles required to achieve the stable capacity behavior (Fig. 5.6b). The specific discharge capacity stays near 190 mAh g⁻¹, whereas the super P carbon contribution was estimated to be below 20 mAh g⁻¹ under the used test conditions. The charge-discharge profiles of **OHTAPQ**-based cells do not show any plateau, which is typical for organic molecules with multiple redox centers such as conjugated polymers (Fig. 5.6c). (118, 127) The average cell discharge potential stays at the level of ~1.7 V (Fig. 5.6d).

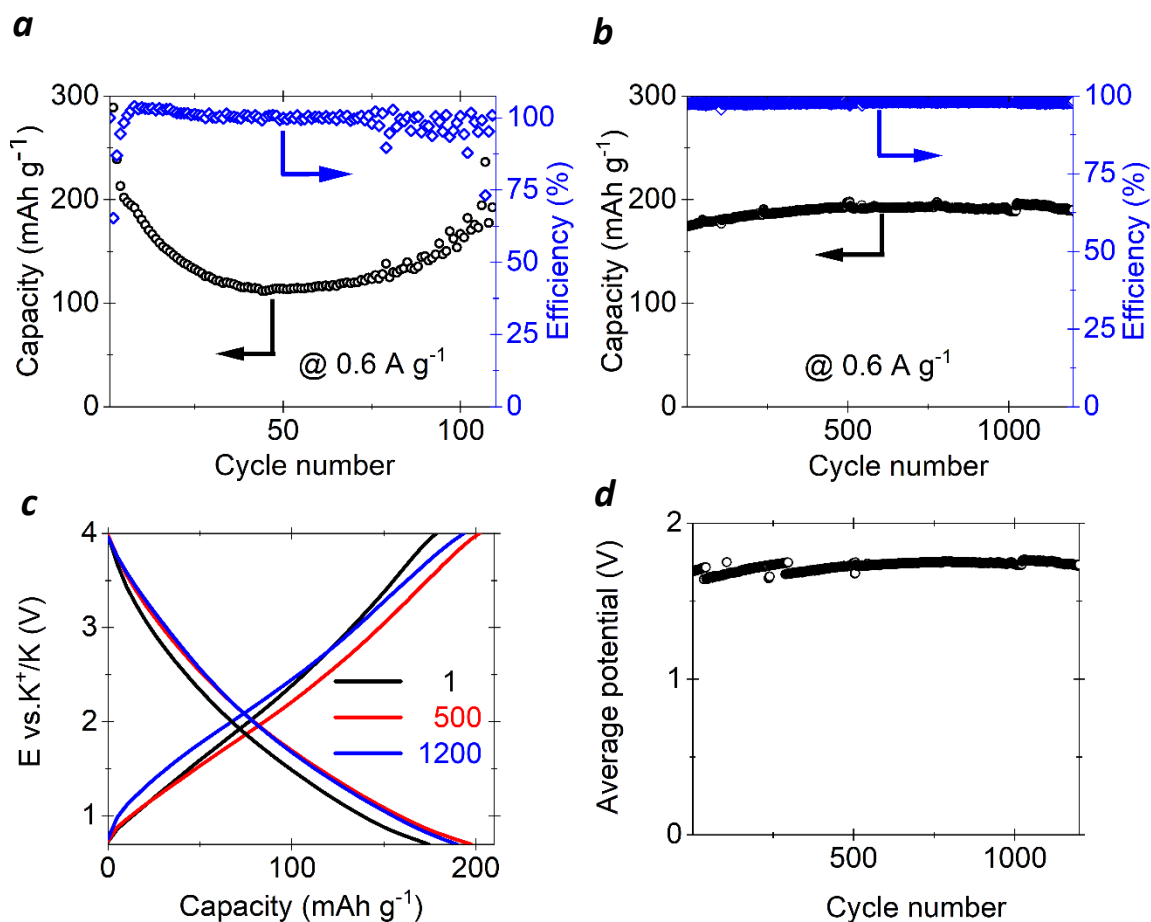


Fig. 5.6 Comparison of cycling performance of **OHTAPQ||K** half-cell in 1M KTF6SI in (DOL:DME= 1/1 v/v) (a) and 2.2 M KPF₆ in G₂ (b). Charge-discharge profile in the voltage range of 0.7-4 V (c) and the average discharge cell potential in G₂-based electrolyte (d).

Notably, starting cycling at 0.6 A g⁻¹ without preconditioning results in initial activation accompanied by the specific capacity increase from ~100 to ~200 mAh g⁻¹ within the first 1000-1500 cycles and then slow decay of the capacity value after ~3000 charge-discharge cycles. A similar behavior was also observed at the higher current density of 1.2 A g⁻¹ (Fig. 5.7).

The obtained results reveal that the fabricated cells have good cyclability, which suggests that the used G₂-based electrolyte is optimal for the **OHTAPQ**||K cells. We believe that KPF₆-G₂ electrolyte formulation promotes the formation of compact SEI at the cathode and probably also at the anode side, which largely stabilizes the electrochemical performance of the batteries (Fig. 5.6b). On the contrary, using KTFSI – DOL/DME electrolyte most likely results in the formation of SEI with an unfavorable structure, which is evident from the rapid capacity decay in these cells. Slow activation of the **OHTAPQ** upon cycling, which is also observed in the G₂-based electrolyte (Fig. 5.7), explains the observed partial capacity restoration at the cycles 50-110 (Fig. 5.7a). Such effects were repeatedly observed previously and are discussed in the recent review. (128)

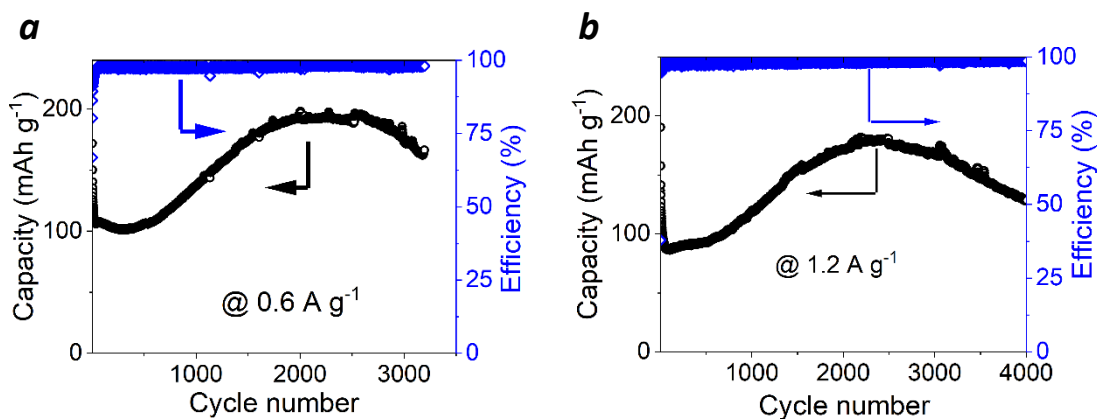


Fig. 5.7 The cycling behavior of the potassium half-cells with **OHTAPQ** electrodes at the current densities of 0.6 A g⁻¹ and 1.2 A g⁻¹ without initial preconditioning.

The aforementioned considerations are supported by the SEM images of the electrodes obtained from the cells which passed >2000 charge-discharge cycles (Fig. 5.8). It is clearly

seen that the grains of the material are covered by a uniform and thin “skin” of SEI, whereas the original composite structure is fully preserved and matches that of the pristine samples. No evident morphology changes were revealed for the electrodes after long-term cycling, which features their excellent stability enabled by a proper SEI formation.

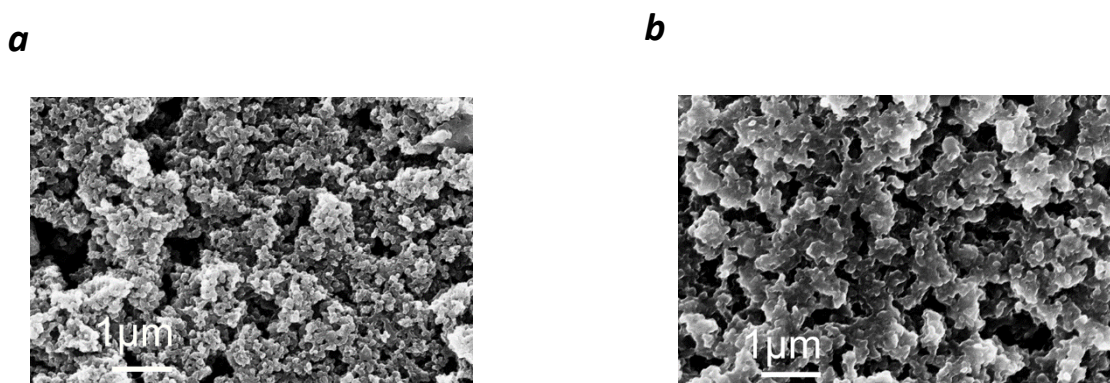


Fig. 5.8 SEM images of the pristine composite electrode (a) and after >2000 charge-discharge cycles in a cell using G₂-based electrolyte (b).

Interestingly, the cells assembled with the previously reported **OHTAP** material (**OHTAPQ** analog without two carbonyl groups) and G₂-based electrolyte formulation demonstrated inferior specific capacity ($\sim 130 \text{ mAh g}^{-1}$) and rapid capacity fading upon cycling (Fig. 5.9). (120)

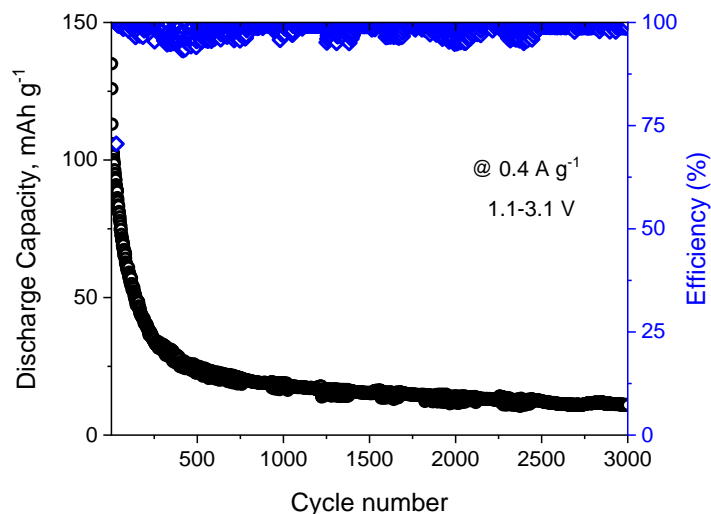


Fig. 5.9 Cycling behavior of the potassium half-cells assembled with **OHTAP** (**OHTAPQ** analog without two carbonyl groups) electrode material and 2.2 M KPF_6 in G_2 as electrolyte.

This observation suggests that the stabilization effect of the $\text{KPF}_6\text{-G}_2$ electrolyte also strongly depends on the composition of the electrode material itself. The rate capability of **OHTAPQ**||K cells was tested after precondition under different current densities ranging from 0.6 to 21 A g^{-1} (Fig. 5.10a,b). The capacity of **OHTAPQ**||K cells approaches 205 mAh g^{-1} at the lowest current density of 0.6 A g^{-1} and stays still reasonably high (>80 mAh g^{-1}) at the current rate of 21 A g^{-1} .

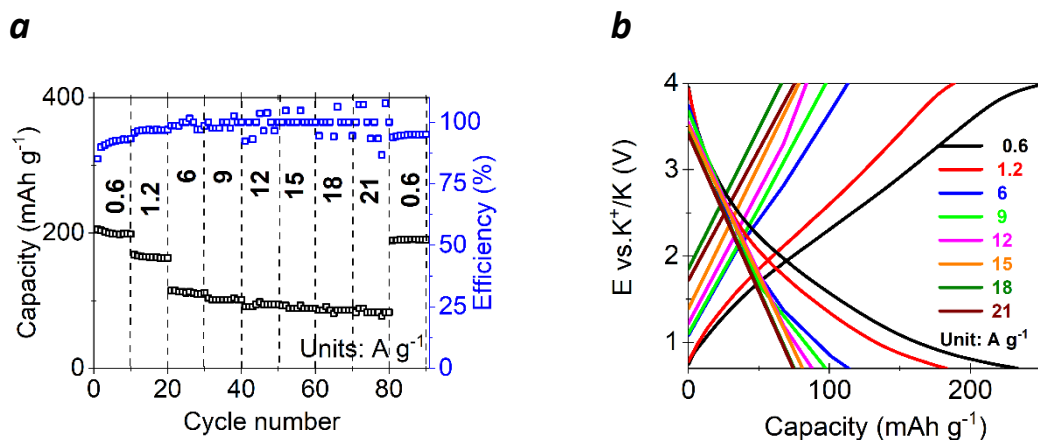


Fig. 5.10 The rate capability of **OHTAPQ**||K half-cells assembled with 2.2 M KPF_6 in G_2 after preconditioning (a) and charge-discharge curves for every 10 cycles (b).

5.4 High-capacity polymer electrodes for potassium batteries

In the previous section, it is concluded that molecular engineering has a great impact on K-ion storage. Hence, in this section, a series of triquinoyl derivatives is chosen to examine electrochemical performance with the objective of comparing the impact of quinoxaline (benzopyrazine) and imine bonds embedded in the polymers.

Six novel quinone-based polymers **P1-P6** were received from our collaborator. These polymers are synthesized starting from commercially available triquinoyl hydrate and the corresponding aromatic amines upon heating at reflux in acetic acid (Fig. 5.11). Thus, polymers **P1** and **P2** were prepared from 3,3'-diamino-*p*-benzidine and 1,2,4,5-tetraaminobenzene, respectively. Polymer **P3** was obtained *via* the condensation of triquinoyl with 2,6-diaminoanthraquinone. The reaction of triquinoyl with 1, 2, or 3 equivalents of *p*-phenylenediamine led to polymers **P4-P6**, respectively.

The electrochemical characteristics of **P1-P6** were investigated in the coin-type CR2032 half-cells with metallic potassium anodes. The cells were first subjected to several galvanostatic charge-discharge cycles to enable the formation of the solid electrolyte interfaces and stabilize the electrochemical performance. Afterward, the potentiostatic measurements were performed. The cyclic voltammograms (CV) of K||**P1** half-cell scanned at 1 mV s^{-1} are shown in Fig. 5.12a, whereas the CVs for the cells with polymers **P2-P6** are presented in Appendices (Fig. A.1).

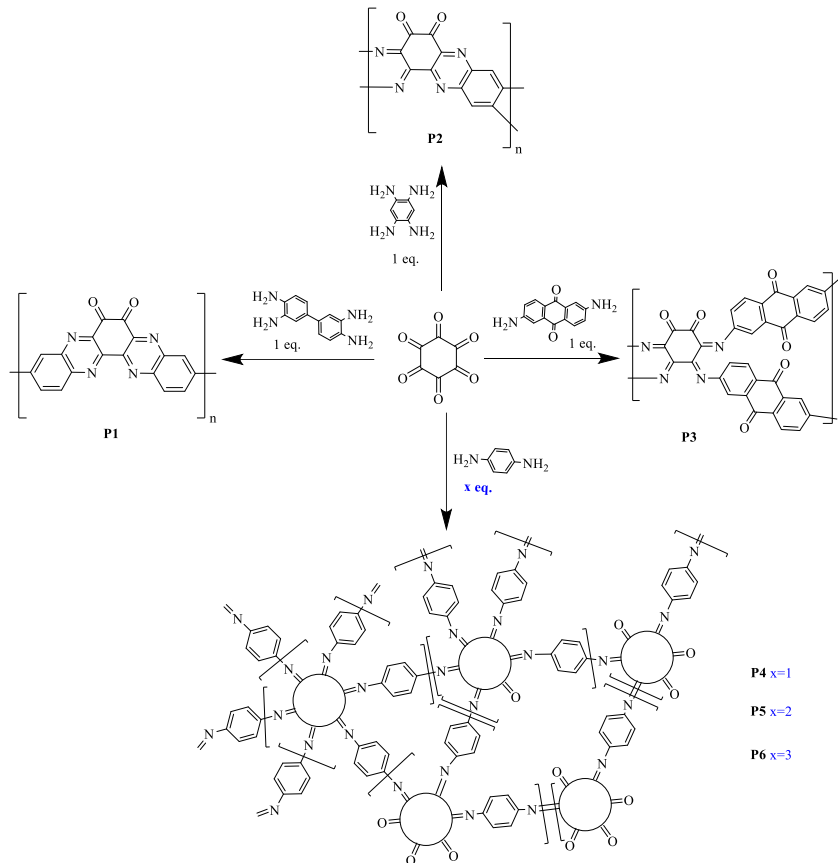


Fig. 5.11 Synthesis of polymers **P1-P6**. The differently substituted triquinoyl fragments in the structures of **P4-P5** are represented by circles; the drawn motifs just illustrate the complexity of these statistical copolymer structures and should not be considered as the exact representations of the molecular structures of these materials.

Cyclic voltammograms for the half-cells with the polymers **P1** (Fig. 5.12a) and **P2** (Fig. A.1b) demonstrate broad waves between 1.0 and 3.5 V, which are typical for conjugated polymers with multiple redox units. (53)

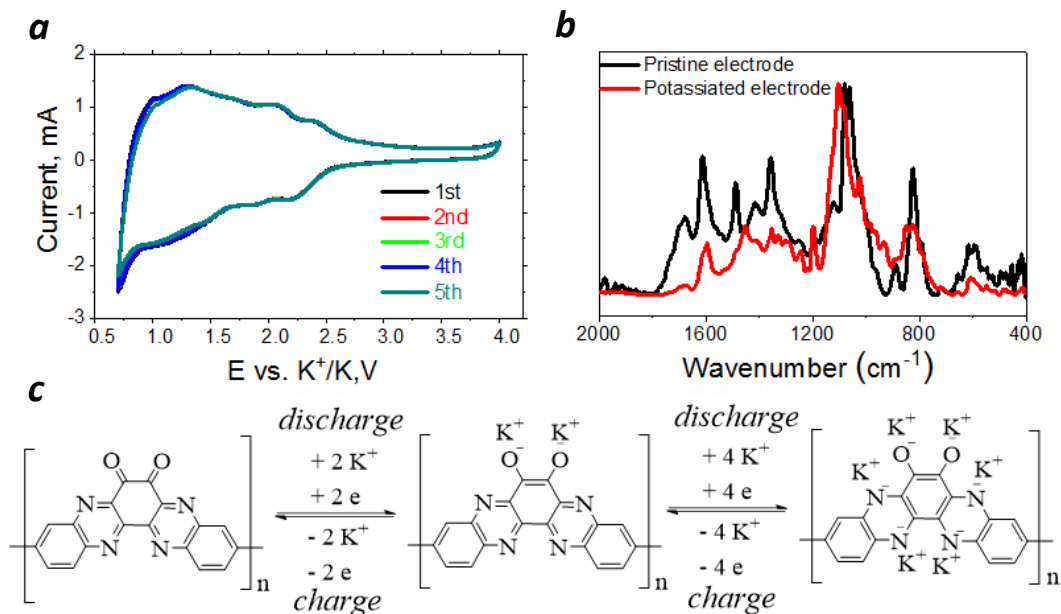


Fig. 5.12 Cyclic voltammograms of **P1** at 1 mV s⁻¹ (five cycles shown) (a) and ATR-FTIR spectra of pristine and potassiated electrodes (b). The K-ion storage and release mechanism for **P1** (c).

Indeed, the electrochemical transformation of some of the functional groups (i.e., reduction of C=O or C=N) gradually decreases the electron affinity of the polymer, which results in a cathodic shift of the potentials required to accomplish the transition of the neighboring redox centers.

Thus, the polymers with tens or hundreds of redox centers are expected to show a comparable number of redox peaks in cyclic voltammograms, which overlap and form a single very broad wave covering a wide range of potentials. (53,120)

Interestingly, the CV of polymer **P3** shows two narrower waves at 1.5-1.85 V and 2.0-2.2 V, which are typical for anthraquinone-based materials (Fig. A.1c). (144) CVs of **P3-P6** (Fig. A.1d-f) are very similar, exceptionally broad, and do not show any specific peaks with except for a sharp feature at ~ 0.7 V corresponding to the contribution from the conductive carbon filler. The cyclic voltammetry data indicate that polymers **P1-P3** are more attractive as organic battery electrode materials, whereas **P4-P6** behave more like pseudocapacitor materials.

Ex-situ X-ray photoelectron spectroscopy (XPS) was used to characterize the composite electrodes based on the polymer **P1** in the pristine, charged (4 V vs. K^+/K) and discharged (0.7 V vs. K^+/K) states as shown in Fig. A.2. The comparison of the C 1s and K 2p parts of the XPS spectra indicated the formation of SEI. Unfortunately, the surface SEI layer masks the transitions that occurred underneath, in the active material, upon charging and discharging. The SEI formation was also confirmed by SEM: the high-resolution image of the electrode subjected to few hundreds of the charge-discharge cycles at 0.5 A g^{-1} shows that the grains of the material are homogeneously covered with a skin of SEI (Fig. A.3).

To investigate the mechanism of K-ion storage in the electrodes based on polymer **P1**, we applied the attenuated total reflectance Fourier-transform infrared spectroscopy (ATR-FTIR). The measurements were performed for pristine electrodes and the electrodes metallated with potassium solution in a diglyme/naphthalene system. Fig. 5.12b shows that the intensity of the peaks corresponding to C=O and C=N bonds at $1400\text{-}1700 \text{ cm}^{-1}$ is notably decreased in the discharged state due to the reduction of the carbonyl groups and pyrazine rings as known from the preceding reports. (141-143) This assignment is

supported also by the appearance of new peaks at 900-1200 cm^{-1} , which are characteristic of the single C-N and C-O bond vibrations. Notably, the experimentally observed changes in the FTIR spectra are fully consistent with the theoretically predicted spectral behavior according to the DFT calculations performed for **P1** and its fully metallated form P18K (computed FTIR spectra are compared in Fig. A.4). Similar ATR-FTIR spectroscopy data were also obtained for the electrodes based on polymers **P2** and **P4**, which confirmed that reductive metallation of the carbonyl groups and C=N bonds is a general mechanism of potassium ion storage in the studied materials (Fig. A.5). The redox transformations of polymer **P1** are schematically illustrated in Fig. 5.12c, whereas the proposed pathways for other polymers are shown in Fig. A.6.

Considering the presented redox pathways, all studied polymers except for **P3** have 6 redox-active fragments (C=O, C=N) per repeating unit and, therefore, could potentially accept six potassium cations together with the same number of electrons. Polymer **P3** has two additional anthraquinone units and, therefore, could potentially undergo a 10-electron redox process and store 10 potassium ions per repeating unit.

Thus, all studied polymers have impressive theoretical specific capacity values as shown in Table 5.1 below.

However, the steric hindrance and electronic effects might hinder the complete stoichiometric metallation of **P1-P6**. We used density functional theory (DFT) calculations to model the redox processes occurring in polymers **P1-P2**. It has been shown that both polymers readily accept two electrons per repeating unit and incorporate two potassium cations, which is an energetically favorable process resulting in the release of ~ 1.6 eV of

energy per introduced K^+ ion. Further 2-electron reactions provide ca. 1.5 times smaller energy gains (Table A.1). Interestingly, the introduction of 4 electrons and the same number of potassium cations per repeating unit of **P2** results in a substantial planarization of the polymer backbone. In the case of **P2**, a similar structure is less planar due to the preferable out-of-plane localization of K^+ cations (Fig. A.7). The complete metallation of **P1-P2** (6e and $6K^+$ per repeating unit) delivers more than twice less energy per introduced potassium cation (~ 0.7 eV) as compared to the first stage of the redox process. However, the realistic energy gains could be considerably higher due to the intermolecular effects. Considering the possibility of K^+ coordination by two polymer chains (supramolecular dimers, Fig. A.8) gives the estimated energy gain ca. 1.5 eV per introduced K^+ ion, which is a very decent value for organic batteries. Similar results were also obtained for the model polyimine-type polymer **P4*** (Fig. A.9), which resembles the structures of **P4-P6**. Thus, the performed theoretical calculations suggest that all polymers **P1-P6** could potentially undergo a complete metallation thus utilizing all redox centers present in their molecular frameworks.

The electrochemical performance of the polymers **P1-P6** was evaluated in potassium half-cells using galvanostatic measurements within the identical voltage window of 0.7-4 V. We note that preconditioning was performed for several hundreds of charge-discharge cycles at 0.5 A g^{-1} to achieve a stable capacity after SEI formation and initial electrode activation.

The polymer **P1** delivered an impressive specific capacity of 355 mAh g^{-1} at the current density of 0.5 A g^{-1} . Furthermore, this material showed excellent rate capability since the

specific capacity retained above 200 mAh g^{-1} even at the high current densities such as 12 A g^{-1} (Fig. 5.13a,b). We note that the carbon filler contribution to the discharge capacity even at the lowest current density of 0.5 A g^{-1} stays in the range of 25 mAh g^{-1} .

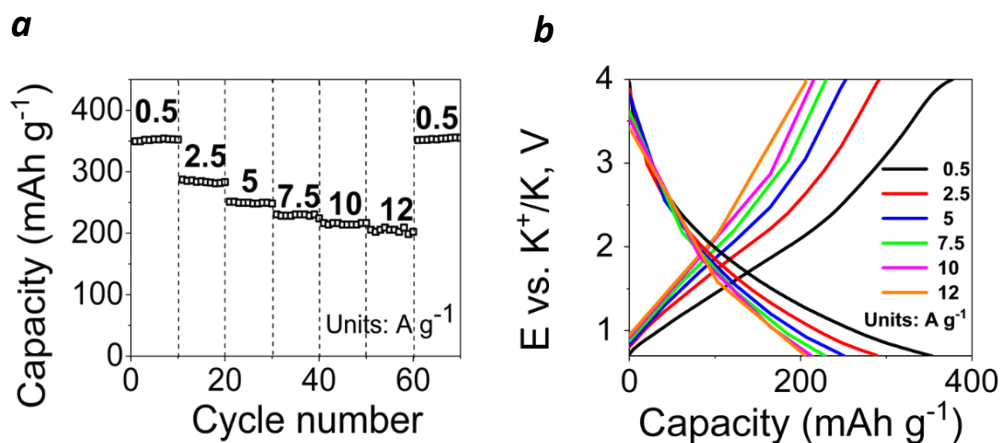


Fig. 5.13 Discharge capacities of P1//K half-cells (a) and charge-discharge profiles (b) at various current densities

Furthermore, the **P1**||K half-cells showed good cyclability: there is no capacity fading after 400 cycles (Fig. 5.14). On the contrary, the specific capacity of **P1**-based cathodes increases up to 422 mAh g^{-1} at the last charge-discharge cycles, which corresponds to $\sim 81\%$ of the theoretical capacity C_{theo} . We fabricated also cells with more than twice increased areal loading of **P1** (0.7 mg cm^{-2}) and obtained decent characteristics: specific capacities of ~ 200 and $\sim 150 \text{ mAh g}^{-1}$ at the current densities of 0.5 and 1.0 A g^{-1} , respectively, in combination with stable battery operation for at least several hundred cycles (Fig. A.10).

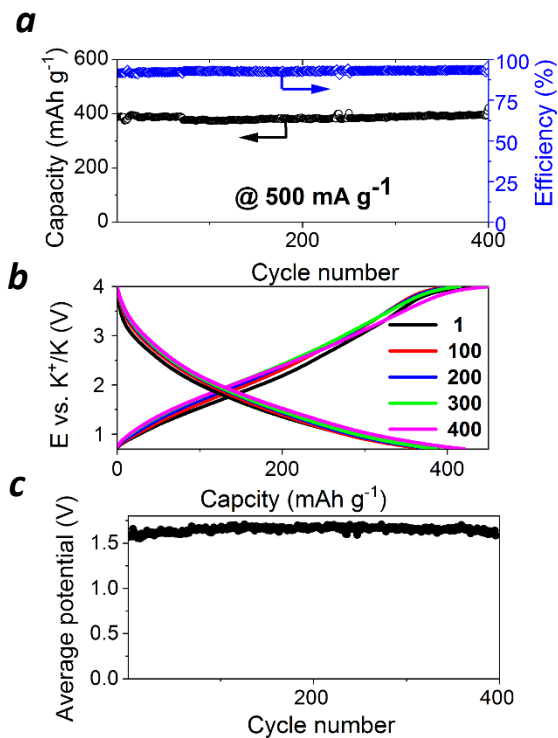


Fig.5.14 Cycling performance of **P1**//K half-cells within the potential window of 0.7-4 V (a), the selected charge-discharge profiles (b), and the average discharge potential plotted as a function of the cycle number (c).

The charge-discharge kinetics for **P1**//K cells were investigated by measuring cyclic voltammograms at different voltage sweeping rates (Fig. 5.15a). The obtained dependencies were analyzed following the general approaches. In particular, the plot of the peak current (I) versus the voltage sweeping rate (mV s^{-1}) delivered the b parameter of 0.77 (Fig. 5.15b). (129) The cells with an entirely capacitive storage mechanism show b values of >1 . On the contrary, batteries with the current controlled by the ion diffusion show b values below 0.5. Thus, we could conclude that the charge storage in **P1**-based electrodes involves a combination of both these mechanisms. In particular, the diffusion current is

dominating at low ($<10 \text{ mV s}^{-1}$) scan rates, whereas the capacitive current contribution becomes predominant at high scan rates (Fig. 5.15c).

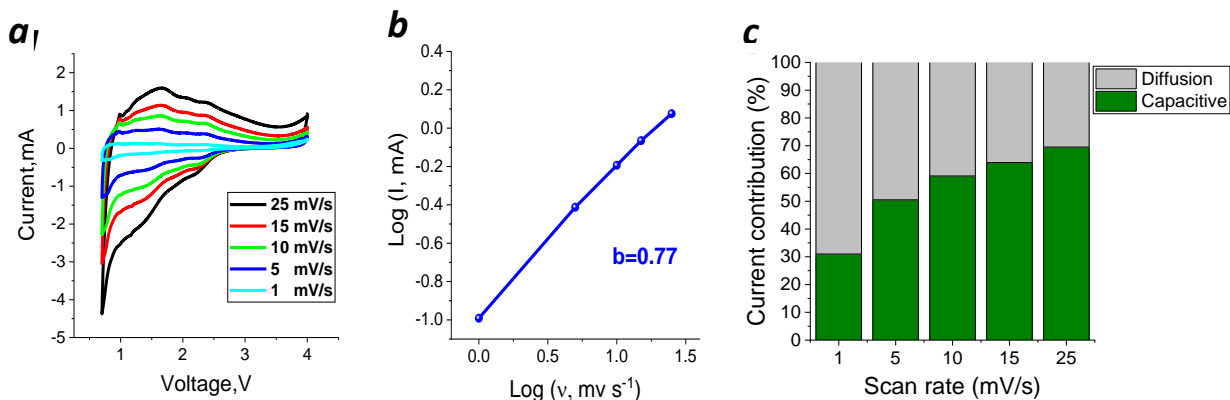


Fig. 5.15 The CV plots of **P1**//K half-cells recorded at different voltage scan rates (a), the plot of the peak current versus the voltage scan rate (b) and the relative contributions of the capacitive and diffusion currents at different scan rates (c).

The potassium half-cells assembled using a more rigid polymer **P2** delivered the specific capacity of $\sim 257 \text{ mAh g}^{-1}$ at 0.6 A g^{-1} and retain 149 mAh g^{-1} at 10 times higher current density of 6 A g^{-1} (Fig. A.11). The **P2**//K cells initially demonstrate a slight decrease in the specific capacity upon cycling followed then by a gradual increase up to 274 mAh g^{-1} after 500 cycles at 0.6 A g^{-1} (Fig. A.11c). Probably, the more rigid chemical structure of **P2** hinders the insertion of K-ions, which results in a lower specific capacity as compared to **P1**. Notably, an increase in the areal loading of **P2** up to 0.7 mg cm^{-2} provided still comparable battery performance: the specific capacity was stabilized at $\sim 220 \text{ mAh g}^{-1}$ when cycling at the current density of $\sim 0.6 \text{ A g}^{-1}$ (Fig. A.12).

The polymer **P3** obtained by condensation of triquinoyl with 2,6-diaminoanthraquinone showed specific discharge capacities of 198 mAh g⁻¹ and 97 mAh g⁻¹ at the current densities of 0.42 A g⁻¹ and 10.6 A g⁻¹, respectively (Fig. A.13). No capacity fading was observed for **P3**||K cells after 50 cycles at 0.4 A g⁻¹, whereas longer cycling resulted in the degradation, which is most likely induced by the active material dissolution in the electrolyte. The maximal observed discharge capacity of 207 mAh g⁻¹ corresponds to 44% of C_{theo} for polymer **P3**. We believe that the steric hindrance of this structure is responsible for the incomplete utilization of the existing redox centers in the electrochemical transformations occurring with this electrode material. The **P4**||K half-cells showed very good cyclability with no capacity fading after 1400 cycles at the current density of 0.55 A g⁻¹ (Fig. A.14). The maximal specific discharge capacity approached 216 mAh g⁻¹, which is 32% of C_{theo} value for **P4**.

An increase in the number of *p*-phenylenediimine bridges in the polymer **P5** to the expense of carbonyl groups enabled good rate capability: the batteries could be discharged within just 44 s at the current density of 11.5 A g⁻¹ (Fig. A.15). The **P5**||K half-cells delivered the specific capacity values of 216 mAh g⁻¹ and 142 mAh g⁻¹ at the current densities of 0.38 A g⁻¹ and 11.5 A g⁻¹, respectively. The cathodes based on the polymer **P5** showed stable cycling within 150 cycles with the final specific discharge capacity of 246 mAh g⁻¹ at 0.38 A g⁻¹. Further loading of the structure with the *p*-phenylenediimine bridges and complete elimination of the carbonyl groups in polymer **P6** improved the cyclability of the batteries as compared to the cells assembled with **P5** (Fig. A.16). Indeed, there was no capacity fade after 1000 charge–discharge cycles at 0.3 A g⁻¹, whereas the final discharge capacity of

P6-based cathodes approached 214 mA h g⁻¹, which is ca. 32% of the C_{theo} value for this material. The electrochemical performance of the polymers **P1-P6** is summarized in Table 5.1. The last column corresponds to the normalized energy density, considering the weight of carbon and binder.

Table 5.1 Overview of the electrochemical performance of polymers **P1-P6**.

Polymer	Theoretical specific capacity (mAh g ⁻¹)	Current density (A g ⁻¹)	Cycle number	The initial capacity (mAh g ⁻¹)	The final capacity (mAh g ⁻¹)	Average discharge potentials (V)	Energy density (Wh kg ⁻¹)	Normalized energy density (Wh kg ⁻¹)
P1	518	0.5	400	388	422	1.65	696	348
P2	686	0.6	500	254	274	1.84	504	252
P3	468	0.4	50	190	207	1.56	322	161
P4	669	0.55	1400	208	216	1.8	392	196
P5	515	0.38	150	243	246	1.7	418	209
P6	418	0.3	1000	204	214	1.77	379	189.5

The presented data show that there is a good correlation between the specific capacities obtained for the electrode materials and their specific surface area (BET) and values. Indeed, the highest specific surface areas were obtained for **P1** followed by **P2** and then **P5** (Table 5.2). The specific capacities observed for these materials descend in the same order.

Table 5.2 Surface area properties of **P1-P6**

Polymers	P1	P2	P3	P4	P5	P6
SSA ¹⁾	21.3	27.2	4.87	3.79	11.6	6.98
m ² g ⁻¹						
Volume of pores ²⁾	0.084	0.14	0.013	0.019	0.082	0.017
cm ³ g ⁻¹						

¹ SSA – specific surface area

² Calculated at P/P₀=0.99

We could also conclude that the construction of polymer chains via the formation of imine (exocyclic C=N) bonds like in the case of **P3-P6** is not the most promising approach since the resulting materials demonstrate modest practical capacities amounting to ~ 30% of the theoretically feasible values. The reasons for such behavior are not completely clear, while they could be related to the poor electronic and/or ionic conductivity of the polymers with imine fragments in the molecular framework. On the contrary, the reactions leading to the formation of pyrazine rings seem to be highly promising in the context of designing advanced redox-active organic materials.

5.5 High-capacity potassium-ion batteries using new rigid backbone quinone-based polymer electrode materials

According to the conclusion achieved from the previous section, the incorporation of polymers with the rigid backbone can suppress the dissolution of active materials in the electrolyte. The main objective of this section is to compare the impact of the implementation of thiopyran, dioxin, and pyrazine rings (shown in Fig 5.16 with the synthesis process) in the rigid polymeric molecular structure in order to reduce the amount of carbon nanofiller in the composite electrode.

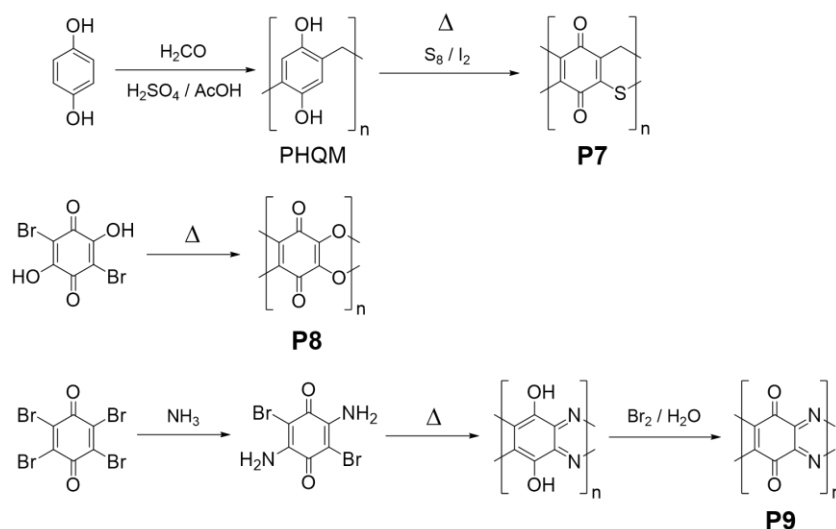


Fig. 5.16 Introduction and synthesis process of polymers **P7-P9**.

SEM was used to investigate the morphology of the fine powders of **P7-P9**. As an example, Fig. 5.17a shows the image of the pristine **P7**, which exhibits uniform round-shaped grains with an average size of $\sim 1 \mu\text{m}$. These particles are mechanically not very strong and could be easily ground or ball-milled to nanosized flakes as shown in Fig. A.17. The **P9** powder showed a very similar morphology to that of **P7** (Fig. 5.17c), whereas **P8** demonstrated a highly porous grainless structure (Fig. 5.17b). Such morphology can be considered very favorable for the battery electrode since it should provide a high surface area and facilitate ion transport. Indeed, the BET surface areas determined using the nitrogen adsorption method for powders of **P7**, **P8** and **P9** were ~ 26 , 236 and $17 \text{ m}^2 \text{ g}^{-1}$, respectively. Thus, the polymer **P8** clearly outperforms **P7** and **P9** in terms of porosity and specific surface area, which suggests that this material could deliver superior electrochemical performance.

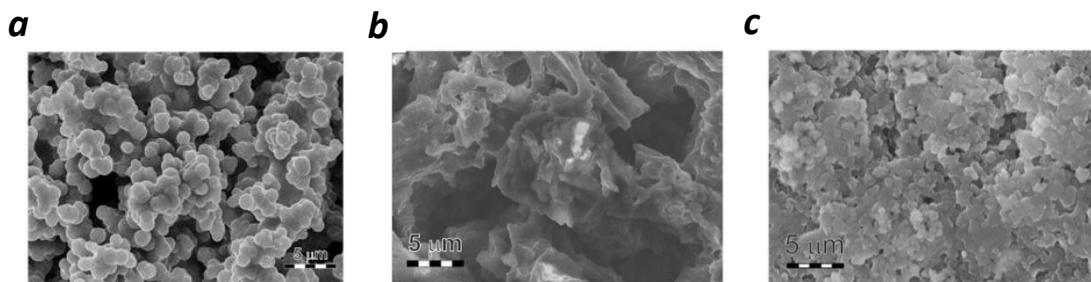


Fig. 5.17 SEM images of the pristine powders of polymers **P7** (a), **P8** (b) and **P9** (c).

CV measurements were performed for half-cells with **P7-P9** used as cathode components and metal potassium anodes. It should be noted that all cells showed initial activation and therefore were preconditioned by galvanostatic cycling at the current density of 350-900 mA g⁻¹ for a number of cycles required to reach a stable capacity. The cyclic voltammogram of **P7**||K cells (Fig. 5.18a) showed a broad wave in the potential range of 1.0-3.5 V, which is characteristic of polymeric materials with multiple redox centers, electronically influencing each other. (130) In other words, the reduction of a quinone unit in **P7** decreases the reduction potential of the neighbouring units since the energy gain becomes smaller due to the repulsive coulombic interactions of the negative charges. Furthermore, the polydispersity of the polymeric materials also contributes to the broadening of the redox peaks on cyclic voltammograms.

The cyclic voltammogram of **P8**||K cells showed a similar broad wave at 0.5-1.2 V, whereas the high-voltage part of the voltammogram was much less pronounced (Fig. A.18 a). Polymer **P9** showed a similar well-pronounced redox wave appearing within the 0.5-2.5 V range (Fig. A.18b). The fact that **P7** shows much higher electrochemical activity at high potentials (2.5-4.0 V vs. K⁺/K) as compared to **P8** and **P9** is most probably associated with the presence of a sulfide unit within the thiopyran rings, which is capable of oxidation

at high potentials as known for other organic sulfides. (131) However, organic sulfide redox transitions are known to suffer from poor reversibility, so the operation of **P7** as an organic cathode can hardly provide the desired cell durability.

To investigate the K-ion storage mechanism in polymers **P7-P9**, we performed *in-situ* spectroelectrochemical measurements. However, all studied polymers showed no Raman signals in the pristine and reduced states, which did not allow us to obtain any reliable information. The electron spin resonance (ESR) spectroscopy revealed the appearance of the same set of signals upon electrochemical reduction of the composite electrodes incorporating **P7-P9** (Fig. A.19). Thus, the obtained ESR spectra cannot be assigned to the redox dynamics of the polymers **P7-P9** having rather different chemical structures and most probably are related to some products of the electrochemical decomposition of the electrolyte. It was reported previously that the electrochemical oxidation of 1,2-dimethoxyethane (DME) produces methyl vinyl ether, which could yield the corresponding $\text{CH}_2=\text{C}-\text{OCH}_3$ radical. (132) However, the hyperfine splitting constants (HFCs) for this radical do not match well the experimentally observed ESR spectrum. On the contrary, the computed and previously reported experimental HFCs for ethyl acetate anion radical are in perfect agreement with the obtained experimental data (Table A.2). The pathway leading to the formation of ethyl acetate in the system remains unknown, and we could only speculate that it involves rearrangement and deprotonation of the DME radical cation. Still, the ethyl acetate and its radical anion likely represent important intermediates leading to the formation of SEI, stabilizing the electrode. (133)

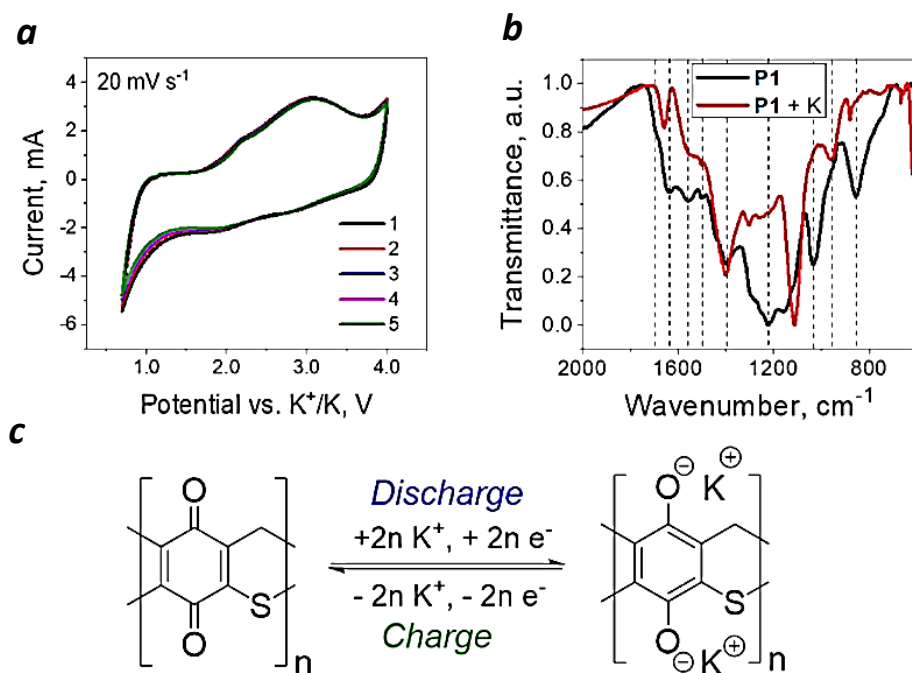


Fig. 5.18 Cyclic voltammogram of **P7** at 20 mV s^{-1} scan rate after galvanostatic preconditioning at 360 mA g^{-1} (a). ATR-FTIR spectra of pristine and metallated **P7** powders (b). The scheme illustrating K^+ storage and release in **P7**-based electrodes (c).

The most straightforward approach to study the spectral changes induced by chemical metallation of the corresponding polymers using potassium naphthalide was based on the application of ATR FTIR spectroscopy as described previously. (134) In particular, the **P7** demonstrated a severe quenching of the bands at $1600\text{-}1700 \text{ cm}^{-1}$ due to the reduction of carbonyl groups. Furthermore, the decrease in the intensity of the peaks at $1150\text{-}1350 \text{ cm}^{-1}$ was observed due to the conversion of the cyclohexadiene moiety to the aromatic ring (Fig. 5.18b). A new characteristic band emerged at $\sim 1110 \text{ cm}^{-1}$ due to the potassium phenolate ($\text{C-O}^-\text{K}^+$) C-O bond vibrations. Importantly, the experimentally observed FTIR spectral changes for **P7** upon the reductive potassiation are completely consistent with the

theoretical predictions as shown in Fig. A.20. Similar FTIR spectral dynamics was also observed for **P8** and **P9** upon the potassiation (Figs. A.21 and A.22).

These results evidence that C=O groups of all polymers **P7-P9** and probably also pyrazine units in the case of **P9** are responsible for the electrochemical activity of these materials. These functions become reduced and accept K^+ ions upon discharge of the batteries, whereas the reverse process occurs upon device charging. The proposed electrochemical pathways are shown in Fig. 5.18c for **P7** and Fig. A.23 for **P8** and **P9**.

Each quinone unit in polymers **P7-P9** could accept two K^+ ions and thus undergo a reduction with the formation of the corresponding potassium hydroquinolate. (120, 135, 136) Such redox transformations of **P7** and **P8** account for the theoretical specific capacities of these materials as high as 357 and 394 mAh g^{-1} . Furthermore, each pyrazine ring in **P9** could undergo 2-electron reduction and accept another two potassium ions, thus boosting the theoretical capacity characteristics of the electrodes based on **P9** up to 818 mAh g^{-1} . (120,135,136)

However, practical capacity could be considerably lower than the theoretical value due to many reasons. Steric hindrance effects induced by relatively large K^+ ions should be specifically considered in the case of electrode materials used in potassium batteries. DFT computational modelling confirmed that polymers **P7-P9** could easily undergo redox transformations coupled with the insertion of two K^+ ions per repeating unit. The potassiation of **P7** and **P8** results in the folding of the main chains of these ladder-type polymers (Fig. A.24a-b). The potassium ions in these structures form coordination bonds with the phenolate oxygen atoms as well as ether (-O-) and thioether (-S-) bridges in the

case of **P8** and **P7**, respectively. Strong coordination bonding of K^+ with the oxygen and nitrogen atoms in **P9** most likely keeps this structure planar (Fig. A.24c). The coordination shells of K^+ ions can be saturated by bonding to at least two polymer molecules as illustrated by the computed structure of the supramolecular dimer $[P9K2]_2$ shown in Fig. A.25. It should be noticed that all three polymers demonstrated comparable specific energy values of 2.0-2.8 eV per inserted potassium ion (Table A.3), which typically become ~ 1.0 eV higher in the solid-state due to the supramolecular bonding effects. It should be noticed that steric hindrance and coulombic repulsion effects seem to prevent a complete reduction and metalation of **P9** with the insertion of 4 potassium ions per repeating unit. There is no energy gain in the transition of $[P9K2]$ to $[P9K4]$ as can be seen from the data presented in Table A.3: the total accumulated energy per repeating unit in the latter is 4.32 eV (ca. 1.08 eV per K^+ ion), which is slightly less than 4.40 eV obtained for the former (2.20 eV per K^+ ion). Somewhat different energy gains could be obtained for $[P9K4]$ in the solid-state due to the multiple coordination bonding of K^+ ions (Fig. A.24b). Still, the formation of $[P9K4]$ upon potassiation of **P9** seems to be unlikely, though the practically achievable specific capacity for this material remains quite high assuming the formation of $[P3K2]$ and could approach 409 mAh g^{-1} .

The electrochemical characteristics of the redox-active polymers **P7-P9** were investigated by galvanostatic charge-discharge cycling of half-cells using the composite polymer-based cathodes, potassium metal anodes and 2.2 M KPF_6 in G_2 as electrolyte. The **P7**||K half-cells were investigated at different current densities within the potential window of 0.1-2.5 V. The cells demonstrated the specific capacity exceeding 200 mAh g^{-1} recalculated for the

P7 active mass, decent rate capability and good cyclability: just a minor capacity decrease was observed after 700 charge-discharge cycles at 0.7 A g^{-1} (Fig. 5.19a-c). The average discharge potential of the cells was ca. 0.56 V (Fig. A.26a), which suggests that **P7** could be considered as a promising anode material for K-ion batteries.

Replacing the thiopyrane unit in **P7** with a 1,4-dioxane fragment in **P8** apparently is beneficial for the electrochemical performance of the material. The **P8**||K half-cells delivered the reversible discharge capacities of $158\text{-}267 \text{ mAh g}^{-1}$ at the current densities ranging from 10 A g^{-1} to 0.66 A g^{-1} , thus illustrating the good rate capability of the polymeric electrodes (Fig. 5.19d,e). Furthermore, the **P8**||K half cells showed a clear activation behavior with the specific capacity gradually increasing to 268 mAh g^{-1} (66% of C_{theo}) after 500 charge-discharge cycles (Fig. 5.19f). The average discharge potential of potassium half-cells with **P8**-based electrodes was $\sim 1.17 \text{ V}$ (Fig. A.26c), which is also more characteristic of anode behavior.

The polymer **P9** with pyrazine units showed poor adhesion to Al foil (both with carbon coating and without it), so copper foil was used as a current collector. The fabricated **P9**||K half cells exhibited a decent rate performance by delivering specific capacities ranging from 143 mAh g^{-1} to 60 mAh g^{-1} at the current densities of $0.8\text{-}5 \text{ A g}^{-1}$ (Fig. 5.19g,h). No capacity fading was observed for the cells with **P9**-based electrodes even after 1400 charge-discharge cycles (Fig. 5.19) at 0.8 A g^{-1} , which manifests decent electrochemical stability of the material. Polymer **P9** can also be considered as an anode material since the average discharge potential of **P9**||K cells was 1.26 V (Fig. A.26d). It is worth noting that the contribution of the super P carbon filler to the capacity of the cells was below 70 mAh g^{-1}

(potential window 0.1-2.5 V) or 30 mAh g⁻¹ (potential window 0.5-4.0 V) as shown in Fig. A.27.

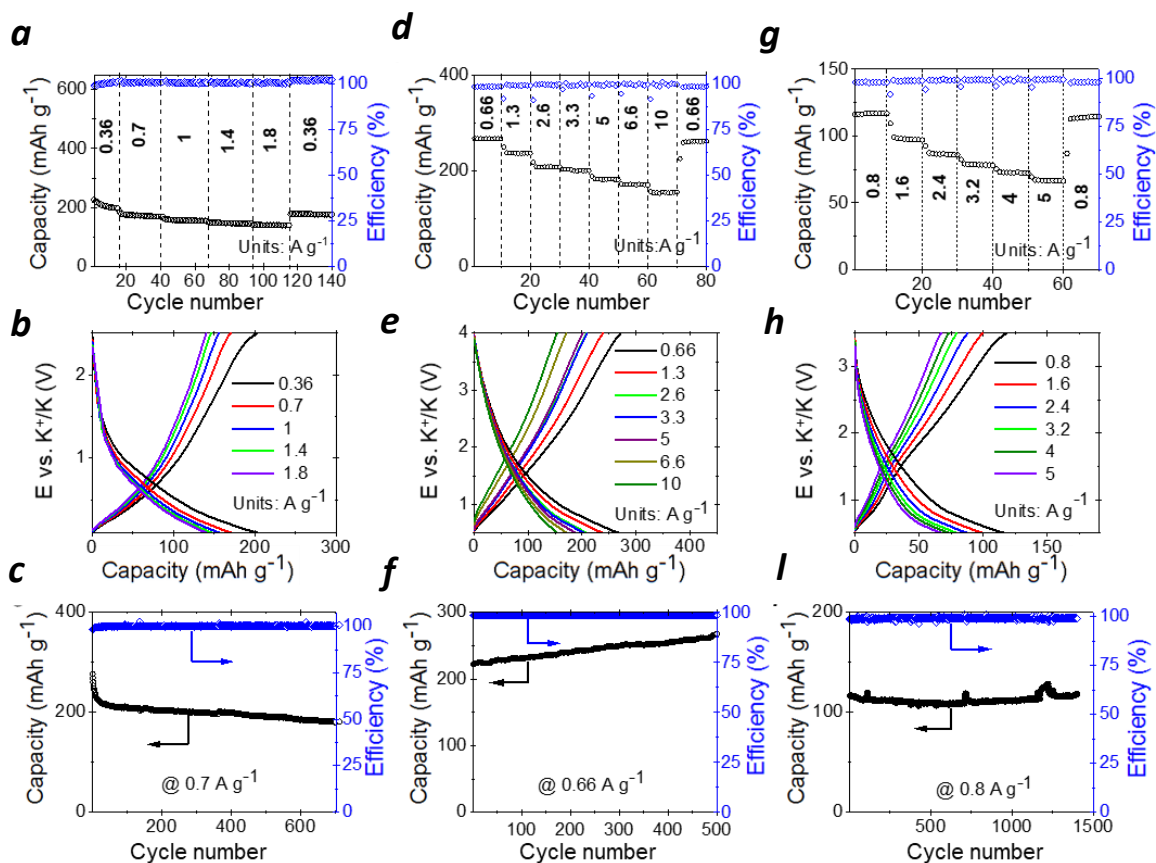


Fig. 5.19 Rate capability (top row), charge-discharge profiles (middle row) and the evolution of the cell discharge capacity upon cycling (bottom row) for the potassium half-cells assembled with the composite electrodes comprising polymers **P7** (a-c), **P8** (d-f), or **P9** (g-l) as redox-active materials.

We emphasize that polymers **P7-P9** have quite rigid ladder-type structures, which suppress undesirable conformational dynamics typically exhibited in redox reactions by conventional polymers with flexible backbones leading to fast electrode degradation and battery failure. (137,138)

Polymers **P7-P9** are also expected to show just a minor volume change upon metal insertion and demetallation, which could also explain the observed good operational stability of the electrodes during continuous charge-discharge cycling. Furthermore, rigid and quasi-conjugated molecular structures of **P7-P9** are beneficial for electronic transport. (139,140).

Indeed, we could increase the loading of the active material **P7** up to 70 wt. % (20 wt. % of carbon filler and 10 wt. % of the binder), which is one of the highest values ever reported for organic electrode materials. The fabricated half-cells showed a very decent specific capacity of $\sim 160 \text{ mAh g}^{-1}$, which increased to 203 mAh g^{-1} after 100 charge-discharge cycles at 0.36 A g^{-1} . (Fig. 5.20a,b)

An increase in the content of the active material and cycling within the optimal potential window (0.7-4 V) provided the higher average discharge potential of 1.78 V (Fig. 5.20b).

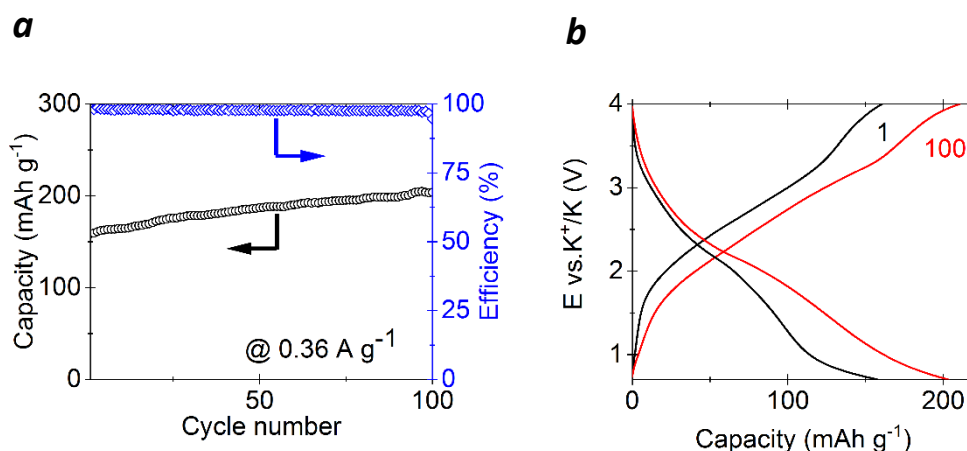


Fig. 5.20 The evolution of the specific capacity of the composite electrode comprised of 70 wt % of **P7** upon battery cycling (a) and charge-discharge profiles of the **P7** | K half-cells within the potential range of 0.7–4 V (b).

Thus, by changing the content of the active component in the composite and adjusting the operational conditions, one could tailor the electrode potential to specific values depending on the target application. This is one of the potential benefits, which could be exploited using organic electrode materials showing plateaus charge-discharge behavior. Further increase in the active material loading in the composite electrodes faces the problem with conductive carbon filler percolation, which is essentially required for efficient charge transport. However, this issue could be mitigated by using alternative forms of carbon with lower percolation threshold such as multiwall carbon nanotubes (MWCNTs), which continuously become less and less expensive. The potassium cells were fabricated with the electrodes comprised of 85 wt. % of redox-active polymers **P7–P9**, 10 wt. % of MWCNTs and 5 wt. % of PVdF binder. In the case of **P7–P8**, the specific capacity approached 300 mAh g⁻¹ after 50 charge/discharge cycles (Fig. 5.21), whereas the coulombic efficiency was low (75–95%), which suggests a significant contribution from irreversible processes probably occurring at the MWCNT/active material interface.

On the contrary, the cells assembled using polymer **P9** delivered a modest capacity of 55-80 mAh g⁻¹, while the coulombic efficiency was stable at ~100%. In order to solve issues corresponding to the inferior coulombic efficiency, particularly the initial coulombic efficiency (ICE), we increased the current density from 30 mA g⁻¹ to 70 mA g⁻¹ for **P7** and **P8** (Fig. 5.22). Surprisingly, **P7**'s ICE improved significantly (83%). Unfortunately, because of the higher surface area of **P8** which is 236 m² g⁻¹ causes more possibility of SEI

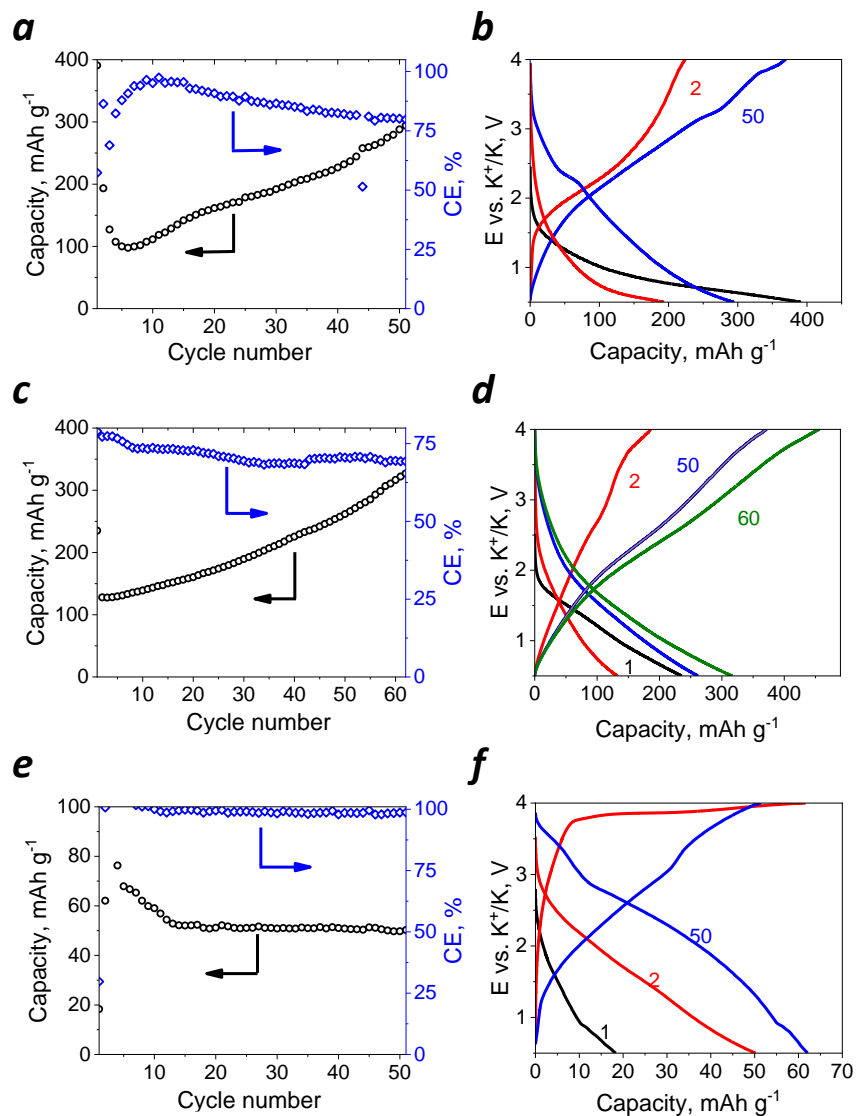


Fig. 5.21 The evolution of the cell discharge capacity upon cycling (left column) and charge-discharge profiles (right column) for the potassium half-cells assembled with the composite electrodes comprising 85 wt. % of polymers **P7** (a-b), **P8** (c-d), or **P9** (e-f) as redox-active materials, 10 wt. % of MWCNTs and 5% of PVdF binder. The charge-discharge cycling was performed at the current density of 30 mA g⁻¹.

formation. Hence, the ICE of **P8** is as low as 51.8%. These results suggest that though the fabrication of organic batteries with high mass loading of the active materials (up to 85%)

is possible, further optimization of the electrode composition and interfacial chemistry is still required.

The electrochemical characteristics of polymers **P7-P9** are summarized in Table 5.3. It should be noted that the best-performing polymer **P8** demonstrated the highest specific surface area as discussed above. The polymer **P7** undergoes some folding and unfolding upon metalation/demetalation, which facilitates ion transport and makes a considerable fraction of the material available for redox reactions. The polymer **P9**, however, has a very rigid, compact planar structure in both pristine and metallated states, which could be the reason for the relatively low practical specific capacity obtained for the electrodes based on this material.

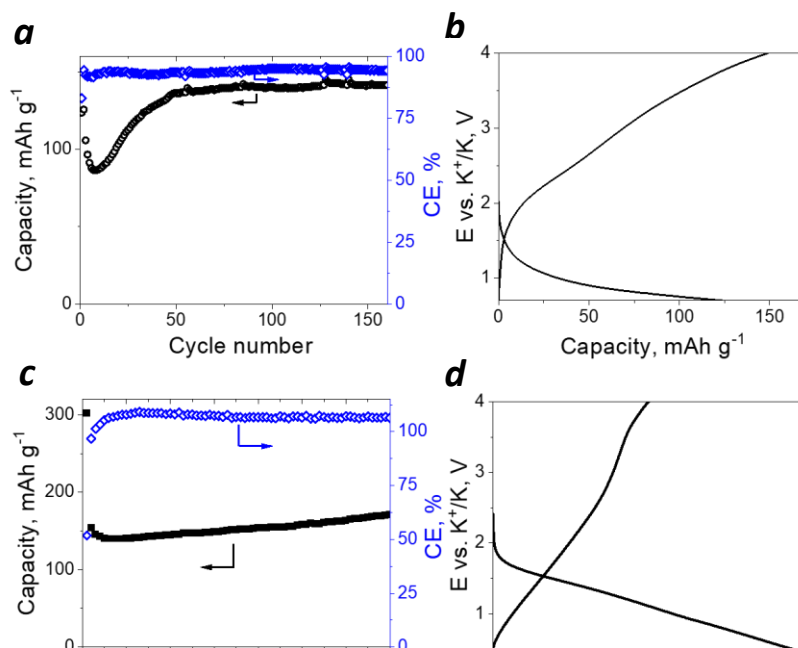


Fig. 5.22 The evolution of the cell discharge capacity upon cycling (left column) and charge-discharge profiles (right column) for the potassium half-cells assembled with the composite electrodes comprising 85 wt. % of polymers **P7** (a-b) or **P8** (c-d) as redox-active materials, 10 wt. % of MWCNTs and 5% of PVdF binder. The charge-discharge cycling was performed at the current density of 70 mA g⁻¹.

Table 5.3 Basic electrochemical performance parameters for potassium half-cells assembled using **P7-P9** electrode materials

Polymer	Polymer content in the composite (%)	Potential window (V)	Current density (A g ⁻¹)	Number of charge-discharge cycles	Theoretical specific capacity (mAh g ⁻¹)*	Initial discharge capacity (mAh g ⁻¹)	Final discharge capacity (mAh g ⁻¹)	Average discharge potential (V)
P7	50	0.1-2.5	0.70	700	357	276	180	0.56
P7	70	0.7-4.0	0.36	100	357	157	203	1.78
P7	85	0.5-4.0	0.03	50	357	193	294	1.50
P8	50	0.5-4.0	0.66	500	394	222	268	1.17
P8	85	0.5-4.0	0.03	60	394	127	327	1.25
P9	50	0.5-3.5	0.80	1400	409	116	118	1.29
P9	85	0.5-4.0	0.03	50	409	62	50	1.29

* - calculated per 2-electron redox transition of each polymer repeating unit

5.6 Concluding remarks

The ability of **OHTAP** to store potassium ions was explored using K||**OHTAP** half-cells, which demonstrated impressive reversible capacities of up to ~220 mAh g⁻¹, which corresponds to ~50% of the theoretical capacity of this material. Nevertheless, the achieved practical capacity stays among the record values reported for potassium cathodes based on both organic and inorganic materials. The obtained results evidence that **OHTAP** represents a promising organic cathode material capable of efficient storage of K. However, this material has certain limitations, which hamper its practical use. Our observations strongly supported the conclusion that **OHTAP** is at least sparingly soluble in electrolytes used in potassium batteries. This dissolution is believed to be the main reason for rapid capacity fading in both types of cells under charge-discharge cycling. To overcome this problem, one might consider an application of properly selected polymer electrolytes, which would not be able to solubilize **OHTAP**. Alternatively, **OHTAP** can

be further functionalized, e.g., polymerized, to reduce dramatically its solubility in any of organic (electrolyte) solvents. The other issue is related to the apparently low ionic and electronic conductivity of **OHTAP** in pristine. The rational design of new **OHTAP**-based molecules with improved molecular architectures and intrinsic properties is recommended for further development. Hence, a novel highly promising organic redox-active material **OHTAPQ** is synthesized from inexpensive commodity-type precursor compounds. The potassium half-cells with **OHTAPQ** electrodes demonstrated high specific capacities going beyond 200 mAh g⁻¹ at 0.6 A g⁻¹, stable operation for >1200 charge-discharge cycles and impressive rate capability. Using the concentrated 2.2 M KPF₆ in G₂ as electrolyte was the key approach to suppress the capacity fading and prevent active material dissolution. The specific power of >41000 W kg⁻¹ demonstrated for **OHTAPQ**-based electrodes in combination with the high capacity and excellent cyclability feature the potential for using this material in ultrafast hybrid-type devices for various high-power applications. Finally, the low discharge potential of the **OHTAPQ**-based electrodes suggests that they might be very attractive and safe anodes for full potassium-ion cells using high-voltage cathodes. To more investigate polymers, the electrochemical performance of a series of six novel redox-active polymers derived from triquinoyl as the key building block is explored. Evaluation of the electrochemical performance of **P1-P6** in half-cells with potassium anodes showed that all these materials are capable of delivering reasonably high specific capacities of >200 mAh g⁻¹ and demonstrate excellent rate capabilities. Among the studied polymers, **P1** demonstrated the highest discharge capacity of 422 mAh g⁻¹ and the record energy density of 696 Wh kg⁻¹ at the current density of 0.5 A g⁻¹. The relatively low average discharge

potential of **P1** (1.65 V) suggests that this material might be considered as a promising anode component for advanced K-ion batteries using high-voltage cathodes. Alternatively, there is substantial room for increasing the discharge potential and hence the energy density of **P1** cathodes via directed chemical functionalization of its backbone e.g., by introducing electron-deficient functional groups.

We have introduced three benzoquinone-based ladder-type redox-active polymers. The availability of these materials in bulk quantities positively distinguishes them from many other previously reported organic electrode materials, which were prepared using sophisticated multi-step chemical synthesis.

All three polymers showed competitive electrochemical performances in potassium half cells with specific discharge capacities ranging from 110 to almost 270 mAh g⁻¹ in combination with good operational stability: no capacity fading was observed for hundreds or even more than a thousand of charge-discharge cycles. The observed superior stability is ensured by the rigid ladder-type structures of polymers **P7-P9**, which suppress unfavorable conformational dynamics leading to the fast degradation of the electrodes based on conventional polymers with flexible backbones.

The cells based on polymer **P8** demonstrated high capacity and decent rate capability, which places this material among the best-performing electrode materials for high-power potassium batteries reported to date. Furthermore, the conjugated or quasi-conjugated backbones of polymers **P7-P9** facilitate electronic transport in these materials. Consequently, we could increase the content of the active polymeric material up to 70 wt.

% as well as 85wt. % and minimize the loading of the carbon filler and PVDF binder without any significant deterioration in the electrochemical performance of the cells.

Thus, the obtained results feature polymers **P7-P9** as promising anode materials for inexpensive and scalable organic K-ion batteries. In particular, there is an urgent need for high-capacity stationary energy storage systems connected to the electric grids to smooth down diurnal and seasonal mismatches in energy production and demand, becoming more and more severe with continuously increased contribution from renewable energies.

Chapter 6

6. Concluding remarks

6.1 Introduction

This dissertation focuses on the electrochemical characterization of organic redox-active materials for energy storage. The main focus of the investigation is on organic materials, specifically the usage of carbonyl-containing materials in energy storage devices. However, carbonyl-based materials possess improper electrical conductivity and dissolution of active materials in investigated electrolytes, which presents adverse challenges. For example, in Chapter 5, the results of characterizing K-ion storage of tetraazapentacene-based (**OHTAP**) demonstrated rapid capacity fade in K-half-cells despite presenting a high amount of discharge capacity in the initial cycles. It is recommended to modify molecular architecture to improve intrinsic properties. To tackle this issue, we explored a structurally identical monomer, octahydroxytetraazapentacene (**OHTAPQ**), with two additional carbonyl functional groups. It is concluded that both modifications on the molecule structure and implementation of super concentrated electrolyte (2.2 M KPF₆ in G₂) have a great impact on battery performance while cycling performance improved from 50 cycles to at least 2700 cycles and suppressing capacity fading of half-cells with power density of ~ 41000 W kg⁻¹.

The main confirmation of the influence of consumption of the G₂-based electrolyte is evident when it stabilized the cycling performance of a series of polymers from triquionoyl-derived polymers not only mitigating capacity fading but also achieving record-breaking results in terms of gravimetric discharge capacity and energy density. To add more, the impact of the inclusion of pyrazine rings and exocyclic bonds is investigated. I concluded that the polymers containing exocyclic bonds do not present high discharge capacity not recommended for the battery application. My collaborator developed new anode materials with rigid backbones that do not dissolve in electrolytes. Therefore, I followed my final objective to boost composition and active mass-loading $\sim 1 \text{ mg cm}^{-2}$. I realized that molecular structures containing thiopyrane and 1,4-dioxane fragments present better electrochemical performance in contrast to the pyrazine ring. More importantly, the consumption of MWCNT can assist in increasing the composition of the electrode from 50 wt. % of active material to 85 wt.%. The thiopyrane-containing polymer showed a higher conductivity and ICE in comparison to pyrazine and dioxin-based compounds.

6.2 Composition and energy density optimization

The summary of obtained results for organic-based electrode materials is presented in Table (6.1). The results show that all materials, except **OHTAP** (due to issues in the molecular structure and dissolution of active materials in the Investigated electrolyte), demonstrated stable cycling performance.

P1 has the highest amount of energy density. This is due to the optimized gravimetric discharge capacity, which suggests that this material could be a promising candidate for high-performance energy storage devices.

The ultimate observation from the data is the optimization of composition from the reduction of carbon nanofiller just from 40 wt. % of carbon super P to 10 wt. % of MWCNT. This indicates that the consumption of conductive additives has great potential in demonstrating the real application of polymers while they have improper TAP density because of composing of the light elements. The comparison of incorporating 70 wt. % of **P7-9** while using 20 wt. % of carbon super P confirms that thiopyrano-containing presents superior conductivity despite the large surface area of the dioxin-containing polymer **P8** which is $236 \text{ m}^2 \text{ g}^{-1}$. According to this, the dioxin ring has a capacitive contribution. However, both **P7** and **P8** are showing acceptable performance with the usage of 10 wt. % of MWCNT.

6.3 Battery specification comparison with the benchmark

To compare the obtained results with the benchmark, I categorize materials based on average discharge potential. Hence, **P1-P6** and **OHTAPQ** might be considered cathodes. Fig (6.1) shows that **P1** delivers the highest capacity reported so far while **P8** has comparable performance, contrasting with other state-of-art anode materials

Table 6.1 Summary of the obtained results

Materials	Contribution in composition (wt%)	Theoretical capacity (mAh g ⁻¹)	Current density (A g ⁻¹)	Potential range (V)	Cycle number	The initial capacity (mAh g ⁻¹)	The final capacity (mAh g ⁻¹)	Average discharge potential (V)	Energy density (Wh kg ⁻¹)
P1	50	518	0.5	0.7-4	400	388	422	1.65	696
P2	50	686	0.6	0.7-4	500	254	274	1.84	504
P3	50	669	0.55	0.7-4	1400	208	218	1.8	392
P4	50	515	0.3	0.7-4	1000	204	214	1.77	379
P5	50	418	0.38	0.7-4	150	243	246	1.7	418
P6	50	468	0.4	0.7-4	50	190	207	1.56	322
P7	50	357	0.72	0.1-2.5	700	276	180	0.6	108
P7	70	357	0.36	0.7-4	100	157	203	1.78	361
P7	85	357	0.03	0.7-4	50	127	294	1.78	523
P8	50	394	0.66	0.5-4	500	222	268	1.17	313
P8	70	394	0.3	0.5-4	100	61	75	1.3	97.5
P8	85	394	0.030	0.5-4	60	128	327	1.17	382
P9	50	409	0.8	0.5-3.5	1400	116	118	1.29	152
P9	85	409	0.03	0.5-4	50	76	50	1.29	98
OHTAPQ	50	730	0.6	0.7-4	1200	174	190	1.7	323
OHTAP	50	440	0.44	1.1-2.8	50	332	162.6	1.6	530.7

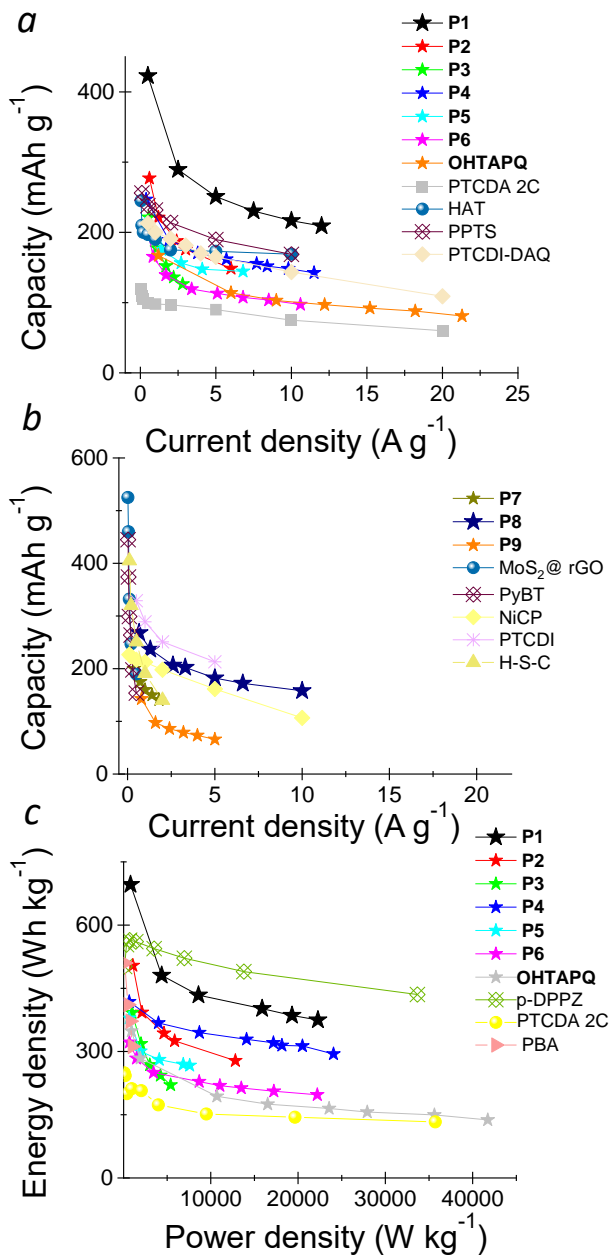


Fig. 6.1 Comparison of the presented results with the best-reported positive electrode materials (a) (36, 47,124,145) negative electrode materials (b) (146-149) Comparison of the presented results with the best-reported half-cells in terms of energy and power density (c) (150-152).

shown in publications (Fig. 6.1b). **P1** has less energy and power density versus p-DPPZ because this kind of a *p*-type polymer has a higher average discharge potential (~ 3.6 V) while **P1** possesses an average discharge potential of 1.65 V. (Fig 6.1c) The ultimate and significant conclusion emerges as the amount of the conductive matrix is reduced from 40 wt. % to 10 wt. %. As presented in Fig 6.2, **P7-9** contain the highest amount of active mass among all reported organic materials, placing **P7-P8** where composite electrodes contain less conductive carbon delivering high discharge capacity.

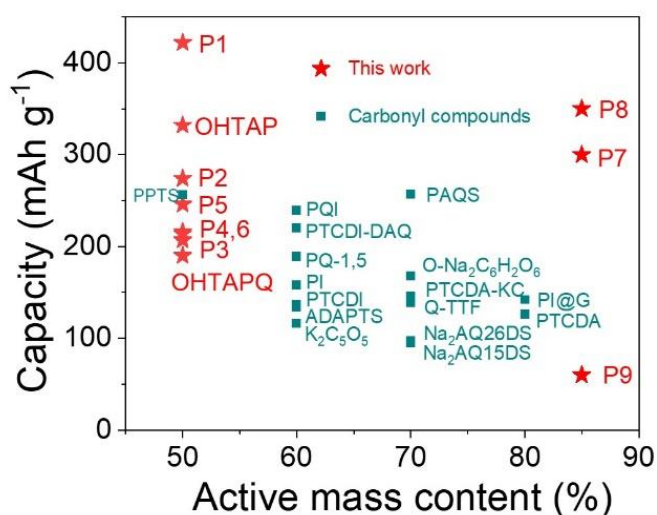


Fig. 6.2 Active mass content comparison of the investigated materials with other carbonyl-containing organic materials. (153)

6.4 Capacity retention comparison with benchmark

To the best of our knowledge, the explored materials have the highest capacity retention after several hundred cycles, placing the cycling performance of our materials close to record-breaking reported results, e.g., HAT has cyclability with ignorable capacity

fading for 4800 cycles (Fig. 6.3). In addition, the contrast with other materials revealed the superiority of **P1-9** and **OHTAPQ** with intercalation and alloy-based anode materials. The reason for the cyclability and capacity retention might relate to the morphology of the composite electrodes. Typically, the morphology of a composite electrode is expressed in terms of porosity and tortuosity.

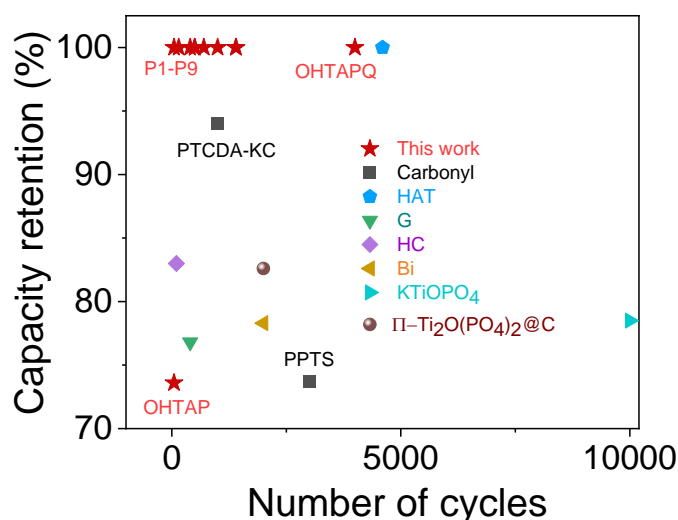


Fig. 6.3 Capacity retention comparison of polyanion and organic redox active materials with the best-reported materials so far. (75, 77, 154-157).

Large porosity and small tortuosity are beneficial for the electrode to have good ion-transfer characteristics, whereas closely packed electrode with low porosity enhance electron transfer. To find more pertinent details corresponding to the rate capability and cyclability, two conclusions are extracted based on morphology of composite electrodes:

1. Porosity and presence of macropores ensure extraordinary rate capability. For example, **P1** and **OHTAPQ** (Fig. 6.4).

2. Compactness ensures long cycling performance. For example, electrodes for **P2-P8** and **OHTAPQ** are more compact (Fig. 6.5 a-f). Unfortunately, **P3** and **P5** are dissolving in the electrolyte in spite of their compactness and porosity. Therefore, they have inferior cyclability.

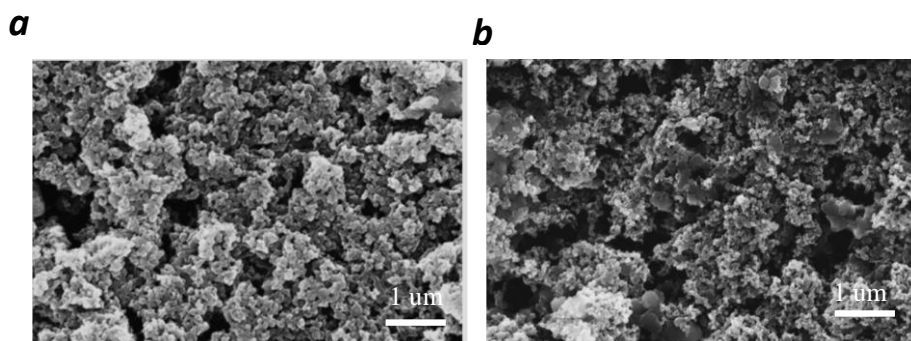


Fig. 6.4 Morphology of composite electrodes containing **P1** (a) and **OHTAPQ** (b)

Finally, electrodes made of small active particles with a larger pore size have higher electrical conductivity and better discharging performance under the high C-rate conditions compared with the electrode with large particles and smaller pore sizes. The porosity of electrodes plays an important role allowing a good contact between the particles and the electrolyte as well as providing a large available surface area for the electrochemical reactions. At the same time, compacting the electrode structure also increases its adhesion to the current collector foil, and decreases the resistivity.

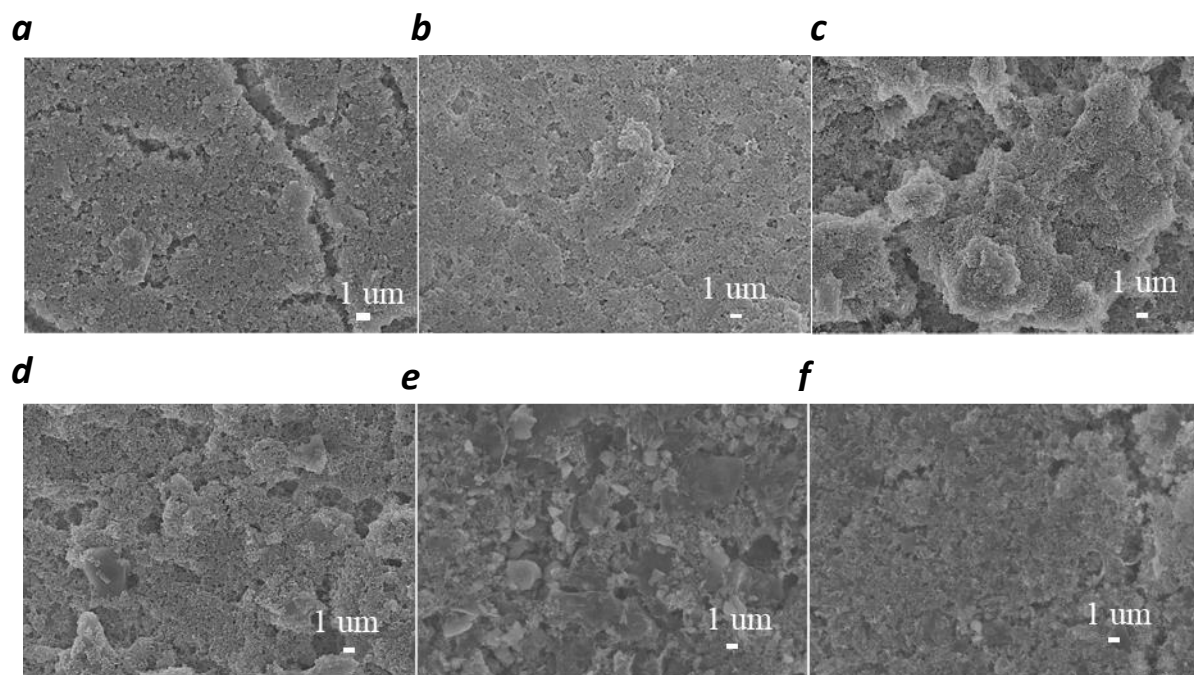


Fig. 6.5. SEM image of the composite electrodes containing **P2** (a), **P3** (b), **P4** (c), **P6** (d), **P7** (e) and **P8** (f).

6.5 Recommendations for the prospective research

To present the real application of polymers as cathodes, it is highly recommended to introduce electron-withdrawing moieties into their structure (Fig. 6.6). Unfortunately, the organic materials presented in this study have insufficient average redox potentials that are too low to be considered cathodes.

Additionally, the practical application of K-free organic molecules, even with an average reduction potential of approximately 3 V, is questionable. Therefore, efforts should be focused either on synthesizing organic potassium salts or on pre-metalation of organic materials.

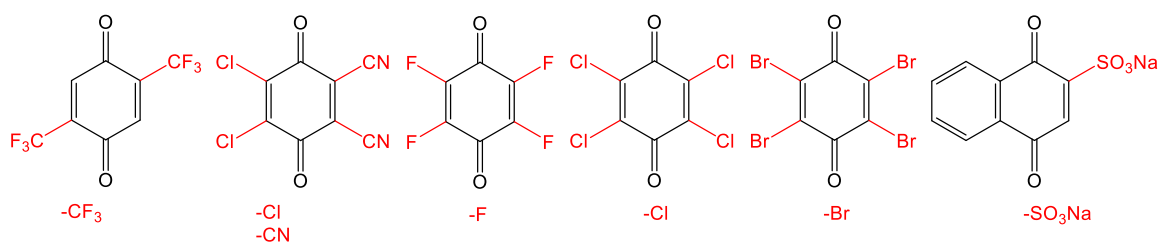


Fig. 6.6 Proposed electron withdrawing groups (shown in red) to be introduced in the molecular structure. (135)

Although the inclusion of MWCNT in the composite electrode preparation has a great impact on composition optimization (**P7-P9**), the cyclability of these polymers must be further improved by designing a novel electrolyte formulation. Thus, it necessitates determining precisely the LUMO and HOMO of electrolytes and the novel electrode materials. Furthermore, following the implementation of the aforementioned recommendations, it is necessary to explore the possibility of assembling all-polymer batteries (Fig.6.7a). In addition, an *n*-type polymer might be paired with a high voltage cathode material (either organic or inorganic) in the full configuration hetero-structure batteries. Nevertheless, maximum care should be used to apply electrolytes compatible with both electrode materials (Fig 6.7b).

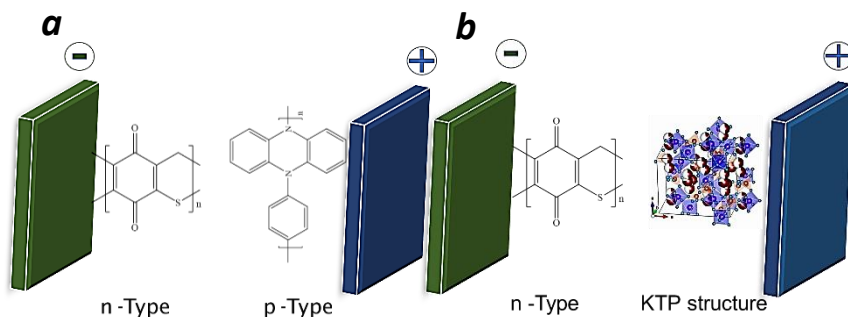


Fig. 6.7 Possible scenarios to assemble full potassium batteries. All organic (a), hetero-structure (b).

Bibliography

1. Yan Z and Obrovac M N. Quantifying the cost effectiveness of non-aqueous potassium-ion batteries. *J. Power Sources* 2020 464 228228.
2. <https://cicenergigune.com/en/blog/sodium-battery-perfect-sustainable-complement-lithium-batteries>
3. Zhou M, Bai P, Ji X, Yang J, Wang C, Xu Y. Electrolytes and Interphases in Potassium Ion Batteries. *Adv. Mater.* 202133(7), 200374.
4. Borah R, Hughson FR, Johnston J, Nann T. On battery materials and methods. *Mater. Today Adv.* 2020 6 100046.
5. Chang WC, Wu JH, Chen KT, Tuan HY. Red Phosphorus Potassium-Ion Battery Anodes. *Adv. Sci.* 2019 6(9) 1970052.
6. Madec L, Gabaudan V, Gachot G, Stievano L, Monconduit L, Martinez H. Paving the Way for K-Ion Batteries: Role of Electrolyte Reactivity through the Example of Sb-Based Electrodes. *ACS Appl. Mater. Interfaces.* 2018 10(40), 34116–22.
7. Jian Z, Luo W, Ji X. Carbon Electrodes for K-Ion Batteries. *J Am Chem Soc.* 2015 137(36), 11566–9.
8. Mao J, Wang C, Lyu Y, Zhang R, Wang Y, Liu S, Wang Z, Zhang S and Guo Z. Organic electrolyte design for practical potassium-ion batteries. *J. Mater. Chem. A.* 2022, 10, 19090-106
9. Wen S, Gu X, Ding X, Zhang L, Dai P, Li L, Liu D, Zhang W, Zhao X and Guo Z. Constructing ultrastable electrode/electrolyte interface for rapid potassium ion storage capability via salt chemistry and interfacial engineering. *Nano Res.* 2022 15(3), 2083–91.

10. Bie X, Kubota K, Hosaka T, Chihara K, Komaba S. A novel K-ion battery: hexacyanoferrate(ii)/graphite cell. *J Mater Chem A*. 2017, 5(9), 4325–30.
11. Hosaka T, Matsuyama T, Kubota K, Yasuno S, Komaba S. Development of KPF₆/KFSA Binary-Salt Solutions for Long-Life and High-Voltage K-Ion Batteries. *ACS Appl Mater Interfaces*. 2020 12(31), 34873–81.
12. Tan H, Lin X. Electrolyte Design Strategies for Non-Aqueous High-Voltage Potassium-Based Batteries. *Molecules* 2023 28(2), 823.
13. Westman K. Diglyme as an electrolyte solvent for sodium-ion batteries Deciphering degradation mechanisms and redox behaviour. 2016
14. Li M, Hicks RP, Chen Z, Luo C, Guo J, Wang C, Xu Y. Electrolytes in Organic Batteries. *Chem. Rev.* 2023 123 1712–1773.
15. Goujon N, Casado N, Patil N, Marcilla R, Mecerreyes D. Organic batteries based on just redox polymers. *Prog. Polym. Sci.* 2021 122 101449.
16. Pavlovskii AA, Pushnitsa K, Kosenko A, Novikov P, Popovich AA. Organic Anode Materials for Lithium-Ion Batteries. *Recent Progress and Challenges. Materials*. 2023 16(1), 17716.
17. Zhao L Bin, Gao ST, He R, Shen W, Li M. Molecular Design of Phenanthrenequinone Derivatives as Organic Cathode Materials. *ChemSusChem*. 2018 11(7), 1215–22.
18. Nishida S, Yamamoto Y, Takui T, Morita Y. Organic rechargeable batteries with tailored voltage and cycle performance. *ChemSusChem*. 2013 6(5), 794–7.

19. Morita Y, Nishida S, Murata T, Moriguchi M, Ueda A, Satoh M, Arifuku K, Sato K, Takui T. Organic tailored batteries materials using stable open-shell molecules with degenerate frontier orbitals. *Nat Mater.* 2011 10(12), 947–51.
20. Lee M, Hong J, Seo DH, Nam DH, Nam KT, Kang K, Park CB. Redox cofactor from biological energy transduction as molecularly tunable energy-storage compound. *Angewandte Chemie.* 2013 52(32), 8322–8.
21. Kim H, Kwon JE, Lee B, Hong J, Lee M, Park SY, Kang K. High Energy Organic Cathode for Sodium Rechargeable Batteries. *Chem. Mater.* 2015 27(21), 7258–64.
22. Banda H, Damien D, Nagarajan K, Raj A, Hariharan M, Shaijumon MM. Twisted Perylene Diimides with Tunable Redox Properties for Organic Sodium-Ion Batteries. *Adv. Energy Mater.* 2017 7(20), 2017.
23. Lyu H, Jafta CJ, Popovs I, Meyer HM, Hachtel JA, Huang J, Sumpter B, Sheng Dai S and Sun XG. A dicyanobenzoquinone based cathode material for rechargeable lithium and sodium ion batteries. *J Mater Chem A.* 2019 7(30), 17888–95.
24. Vadehra GS, Maloney RP, Garcia-Garibay MA, Dunn B. Naphthalene diimide based materials with adjustable redox potentials: Evaluation for organic lithium-ion batteries. *Chem. Mater.* 2014 26(24), 7151–7.
25. Wan W, Lee H, Yu X, Wang C, Nam KW, Yang XQ, Zhou H. Tuning the electrochemical performances of anthraquinone organic cathode materials for Li-ion batteries through the sulfonic sodium functional group. *RSC Adv.* 2014 4(38), 19878–82.

26. Lu Y, Zhao Q, Miao L, Tao Z, Niu Z, Chen J. Flexible and Free-Standing Organic/Carbon Nanotubes Hybrid Films as Cathode for Rechargeable Lithium-Ion Batteries. *J. Phys. Chem. C* 2017, 121, 27, 14498–1450626.
27. Liang Y, Zhang P, Chen J. Function-oriented design of conjugated carbonyl compound electrodes for high energy lithium batteries. *Chem Sci.* 2013 4(3), 1330–7.
28. Liang Y, Zhang P, Yang S, Tao Z, Chen J. Fused heteroaromatic organic compounds for high-power electrodes of rechargeable lithium batteries. *Adv Energy Mater.* 2013 3(5), 600–5.
29. Burkhardt SE, Lowe MA, Conte S, Zhou W, Qian H, Rodríguez-Calero GG, Gao J, Hennig G and Abruña HD. Tailored redox functionality of small organics for pseudocapacitive electrodes. *Energy Environ. Sci.* 2012 5(5), 7176–87.
30. Heiska J, Nisula M, Karppinen M. Organic electrode materials with solid-state battery technology. *J. Mater. Chem. A.* 2019 7 18735–58.
31. Liang Y, Jing Y, Gheyhani S, Lee KY, Liu P, Facchetti A, Yao Y. Universal quinone electrodes for long cycle life aqueous rechargeable batteries. *Nat Mater.* 2017 16(8), 841–8.
32. Lee J, Park MJ. Tattooing Dye as a Green Electrode Material for Lithium Batteries. *Adv Energy Mater.* 2017 7(12), 1602279.
33. Wang Y, Song Y, Xia Y. Electrochemical capacitors: Mechanism, materials, systems, characterization and applications. *Chem. Soc. Rev.* 2016 45 5925–50.
34. Zhang L, Liu Z, Cui G, Chen L. Biomass-derived materials for electrochemical energy storages. *Prog. Polym. Sci.* 2015 43 136–64.

35. Jian Z, Liang Y, Pérez IAR, Yao Y, Ji X. Poly(anthraquinonyl sulfide) cathode for potassium-ion batteries. *Electrochem commun.* 2016 71 5–8.
36. Tang M, Wu Y, Chen Y, Jiang C, Zhu S, Zhuo S, Wang C. An organic cathode with high capacities for fast-charge potassium-ion batteries. *J Mater. Chem. A.* 2019 7(2), 486–92.
37. Gao H, Xue L, Xin S, Goodenough JB. A High-Energy-Density Potassium Battery with a Polymer-Gel Electrolyte and a Polyaniline Cathode. *Angewandte Chemie.* 2018 57(19), 5449–53.
38. Zhou M, Liu M, Wang J, Gu T, Huang B, Wang W, Wang K, Chenga S and Jiang K. Polydiaminoanthraquinones with tunable redox properties as high performance organic cathodes for K-ion batteries. *Chem. Commun.* 2019 55(43), 6054–7.
39. T. Sun, Z.-J. Li, X. Yang, S. Wang, Y.-H. Zhu and X.-B. Zhang, Imine-Rich Poly(O-phenylenediamine) as High-Capacity Trifunctional Organic Electrode for Alkali-Ion Batteries. *Chin. Chem. Soc.*, 2019 1 365–372.
40. Kato M, Masese T, Yao M, Takeichi N, Kiyobayashi T. Organic positive-electrode material utilizing both an anion and cation: A benzoquinone-tetrathiafulvalene triad molecule, Q-TTF-Q, for rechargeable Li, Na, and K batteries. *New J. Chem.* 2019 43(3), 1626–31.
41. Ma J, Zhou E, Fan C, Wu B, Li C, Lu ZH, Li J. Endowing CuTCNQ with a new role: A high-capacity cathode for K-ion batteries. *Chem. Commun.* 2018 54(44):5578–81.
42. Chen L, Zhao Y. Exploration of p-Na₂C₆H₂O₆ -based organic electrode materials for sodium-ion and potassium-ion batteries. *Mater Lett.* 2019 243, 69–72.

43. Pan Q, Zheng Y, Tong Z, Shi L, Tang Y. Novel Lamellar Tetrapotassium Pyromellitic Organic for Robust High-Capacity Potassium Storage. *Angewandte Chemie*, 2021 60(21), 11835–40.
44. Fan L, Ma R, Wang J, Yang H, Lu B. An ultrafast and highly stable potassium–Organic battery. *Adv. Mater.* 2018 30(51), 1805486.
45. Chen Y, Luo W, Carter M, Zhou L, Dai J, Fu K, Lacey S, Li T, Wan J, Han X, Bao Y, Hu L. Organic electrode for non-aqueous potassium-ion batteries. *Nano Energy*. 2015 18, 205–11.
46. Tong Z, Tian S, Wang H, Shen D, Yang R, Lee CS. Tailored Redox Kinetics, Electronic Structures and Electrode/Electrolyte Interfaces for Fast and High Energy-Density Potassium-Organic Battery. *Adv Funct Mater.* 2019 1907656, 1–10.
47. Kapaev RR, Zhidkov IS, Kurmaev EZ, Stevenson KJ, Troshin PA. Hexaazatriphenylene-based polymer cathode for fast and stable lithium-, sodium- And potassium-ion batteries. *J Mater Chem A*. 2019 7(39), 22596–603.
48. Liang Y, Luo C, Wang F, Hou S, Liou SC, Qing T, Li Q, Zheng J, Cui C, Wang C. An Organic Anode for High Temperature Potassium-Ion Batteries. *Adv. Energy Mater.* 2019 9(2), 1802986.
49. Chiang C. K., Fincher C. R., Jr., Park Y. W., Heeger A. J., Shirakawa H., Louis E. J., Gau S. C., and MacDiarmid Alan G. Electrical Conductivity in Doped Polyacetylene. *Phys. Rev. Lett.* 1979 39 1098.

50. Winsberg J, Hagemann T, Janoschka T, Hager MD, Schubert US. Redox-Flow-Batterien: von metallbasierten zu organischen Aktivmaterialien. *Angewandte Chemie*. 2017 129(3), 702–29.
51. Liang Y, Chen Z, Jing Y, Rong Y, Facchetti A, Yao Y. Heavily n-dopable π -conjugated redox polymers with ultrafast energy storage capability. *J Am Chem Soc*. 2015 137(15), 4956–9.
52. Kye H, Kang Y, Jang D, Kwon JE and Kim BG. p-Type Redox-Active Organic Electrode Materials for Next-Generation Rechargeable Batteries. *Adv. Energy Sustainability Res*. 2022 3, 2200030.
53. Obrezkov FA, Shestakov AF, Traven VF, Stevenson KJ, Troshin PA. An ultrafast charging polyphenylamine-based cathode material for high rate lithium, sodium and potassium batteries. *J Mater Chem A*. 2019 7(18), 11430–7.
54. Li C, Xue J, Huang A, Ma J, Qing F, Zhou A, Wang Z, Wang Y, Li J. Poly(N-vinylcarbazole) as an advanced organic cathode for potassium-ion-based dual-ion battery. *Electrochim Acta*. 2019 297, 850–5.
55. Obrezkov FA, Shestakov AF, Vasil'ev SG, Stevenson KJ, Troshin PA. Polydiphenylamine as a promising high-energy cathode material for dual-ion batteries. *J Mater Chem A*. 2021 9(5), 2864–71.
56. Obrezkov FA, Somova AI, Fedina ES, Vasil'ev SG, Stevenson KJ, Troshin PA. Dihydrophenazine-Based Copolymers as Promising Cathode Materials for Dual-Ion Batteries. *Energy Technol*. 2021 9(1) 2000772.

57. Park J, Lee J, Alfaruqi MH, Kwak WJ, Kim J, Hwang JY. Initial investigation and evaluation of potassium metal as an anode for rechargeable potassium batteries. *J. Mater. Chem. A*. 2020 8 16718–37.
58. Sugawara K, Yamamura N, Matsuda K, Norimatsu W, Kusunoki M, Sato T, Takahashi T. Selective fabrication of free-standing ABA and ABC trilayer graphene with/without Dirac-cone energy bands. *NPG Asia Mater.* 2018 10(2), e466.
59. Jian Z, Luo W, Ji X. Carbon Electrodes for K-Ion Batteries. *J Am Chem Soc.* 2015 137(36), 11566–9.
60. An Y, Fei H, Zeng G, Ci L, Xi B, Xiong S, Feng J. Commercial expanded graphite as a low-cost, long-cycling life anode for potassium-ion batteries with conventional carbonate electrolyte. *J Power Sources.* 2018 378 66–72.
61. Share K, Cohn AP, Carter R, Rogers B, Pint CL. Role of Nitrogen-Doped Graphene for Improved High-Capacity Potassium Ion Battery Anodes. *ACS Nano.* 2016 10(10), 9738–44.
62. Li D, Sun Q, Zhang Y, Dai X, Ji F, Li K, Yuan Q, Liu X, Ci L. Fast and stable K-ion storage enabled by synergistic interlayer and pore-structure engineering. *Nano Res.* 2021;14 4502–11.
63. Jian Z, Xing Z, Bommier C, Li Z, Ji X. Hard Carbon Microspheres: Potassium-Ion Anode Versus Sodium-Ion Anode. *Adv Energy Mater.* 2016, 6(3) 1501874.
64. Li W., Li Z., Zhang C., Liu W., Han C., Yan B., An S., Qiu X. Hard Carbon Derived from Rice Husk as Anode Material for High-Performance Potassium-Ion Batteries. *Solid State Ion.* 2020, 351, 115319.

65. Yuan F, Zhang D, Li Z, Sun H, Yu Q, Wang Q, Zhang J, Wu Y, Xi K and Wang B. Unraveling the intercorrelation between micro/mesopores and K migration behavior in hard carbon. *Small* 2107 18 113
66. Larbi L, Larhrib B, Beda A, Madec L, Monconduit L, and Ghimbeu C.M. Impact of Hard Carbon Properties on Their Performance in Potassium-Ion Batteries. *ACS Appl. Energy Mater.* 2023 6 5274–5289
67. Luo G, Feng X, Qian M, Zhang W, Qin W, Wu C and Pan L. State-of-art progress and perspectives on alloy-type anode materials for potassium-ion batteries. *Mater. Chem. Front.*, 2023 7 3011-3036.
68. Imtiaz S, Amiin I.S, Xu Y, Kennedy T, Blackman C, Ryan K. M. Progress and perspectives on alloying-type anode materials for advanced potassium-ion batteries. *Materials Today* 2021 48 241-269.
69. Shen C, Cheng T, Liu C, Huang L, Cao M, Song G, Wang D, Lu B, Wang J, Qin C, Huang X, Peng P, Li X and Wu Y. Bismuthene from sonoelectrochemistry as a superior anode for potassium-ion batteries. *J. Mater. Chem. A.* 2020 8 453–60.
70. Wu Q, Chen B, Xie H, Bai X, Liang M, Wu Z, Jin X, He C, Zhao N. Bismuth-antimony alloy nanoparticles encapsulated in 3D carbon framework: Synergistic effect for enhancing interfacial potassium storage. *Chem. Eng. J.* 2022 430 132906.
71. Wang H, Chen S, Fu C, Ding Y, Liu G, Cao Y, Chen Z. Recent Advances in Conversion-Type Electrode Materials for Post Lithium-Ion Batteries. *ACS Materials Lett.* 2021 3 956–77.

72. Yang F, Wang L, Huang L, Zou G. The study of structure evolvement of KTiOPO_4 family and their nonlinear optical properties. *Coord. Chem. Rev.* 2020 423 213491.
73. Fedotov SS, Samarin AS, Nikitina VA, Stevenson KJ, Abakumov AM, Antipov E V. α -VPO 4: A Novel Many Monovalent Ion Intercalation Anode Material for Metal-Ion Batteries. *ACS Appl Mater Interfaces.* 2019 11(13)12431–40.
74. Tan H, Du X, Huang H-Q and Zhang B. KVPO_4F as a novel insertion-type anode for potassium ion batteries. *Chem. Commun.*, 2019 55 11311-4.
75. Liao J, Hu Q, Mu J, He X, Wang S, Jiemin D, Chen C. In situ carbon coated flower-like VPO_4 as an anode material for potassium-ion batteries. *Chem. Commun.* 2019 55 13916–9.
76. Lu X, Wang S, Xiao R, Shi S, Li H, Chen L. First-principles insight into the structural fundamental of super ionic conducting in NASICON $\text{MTi}_2(\text{PO}_4)_3$ ($M = \text{Li}, \text{Na}$) materials for rechargeable batteries. *Nano Energy.* 2017 41626–633.
77. Voronina N, Jo JH, Konarov A, Kim J, Myung ST. $\text{KTi}_2(\text{PO}_4)_3$ Electrode with a Long Cycling Stability for Potassium-Ion Batteries. *Small.* 2020 16 2001090.
78. Wei Z, Wang D, Li M, Gao Y, Wang C, Chen G, Du F. Fabrication of Hierarchical Potassium Titanium Phosphate Spheroids: A Host Material for Sodium-Ion and Potassium-Ion Storage. *Adv. Energy Mater.* 2018 8 1801102.
79. Qi Y, Li J, Zhong W, Bao S, Xu M. KTiOPO_4 : A long-life, high-rate and low-temperature-workable host for Na/K-ion batteries. *Chem. Eng. J.* 2021 417 128159.
80. Wang W, Kang Z, Sun CF, Li Y. $\text{K}_{2.13}\text{V}_{1.52}\text{Ti}_{0.48}(\text{PO}_4)_3$ as an anode material with a long cycle life for potassium-ion batteries. *Electrochem. commun.* 2022 136 107247.

81. Sun X, Li Z, Liu Z, Lv X, Shi K, Chen R, Wu F, Li Li. A New Candidate in Polyanionic Compounds for Potassium Ion Battery Anode: MXene Derived Carbon Coated π -Ti₂O(PO₄)₂. *Adv Funct Mater.* 2023 2300125.
82. Zhao Q, Lu Y, Chen J. Advanced Organic Electrode Materials for Rechargeable Sodium-Ion Batteries. *Adv. Energ. Mater.* 2017 7 1601792.
83. Xie J, Gu P, Zhang Q. Nanostructured Conjugated Polymers: Toward High-Performance Organic Electrodes for Rechargeable Batteries. *ACS Energy Letters.* 2017 2 1985–1996.
84. Muench S, Wild A, Friebe C, Häupler B, Janoschka T, Schubert U S. Polymer-Based Organic Batteries, *Chem. Rev.* 2016 116 9438–9484.
85. Kulova T L, Skundin A M. High-voltage materials for positive electrodes of lithium ion batteries. (review), *Russ. J. Electrochem.* 2016 52 501–524.
86. Tang M, Li H, Wang E, Wang C. Carbonyl polymeric electrode materials for metal-ion batteries. *Chin. Chem.Lett.* 2018 29 232–244.
87. Liang Y, Yao Y. Positioning Organic Electrode Materials in the Battery Landscape. *Joule.* 2018 2 1690–1706.
88. Xu Y, Zhou M, Lei Y. Organic materials for rechargeable sodium-ion batteries. *Mater. Today.* 2018 21 60–78.
89. Zhao Q, Zhu Z, Chen J. Molecular Engineering with Organic Carbonyl Electrode Materials for Advanced Stationary and Redox Flow Rechargeable Batteries. *Adv. Mater.* 2017 29 1607007.
90. Schon T B, McAllister B T, Li P F, Seferos D S. The rise of organic electrode materials for energy storage. *Chem. Soc. Rev.* 2016 45 6345–6404.

91. Häupler B, Wild A, Schubert U S. Carbonyls: Powerful Organic Materials for Secondary Batteries. *Adv. Energ. Mater.* 2015 5 1402034.
92. Armand M, Michot C, Ravet N. Novel electrode materials derived from polyquinoid ionic compounds and their uses in electrochemical generators, WO Patent 1999 9928984 A1.
93. Chen H, Armand M, Courty M, M Jiang, Grey C P, Dolhem F, Tarascon J M, Poizot P. Lithium Salt of Tetrahydroxybenzoquinone: Toward the Development of a Sustainable Li-Ion Battery. *J. Am. Chem. Soc.* 2009 131 8984–8988.
94. Chen H, Armand M, Demailly G, Dolhem F, Poizot P, Tarascon J M. From Biomass to a Renewable LiXC₆O₆ Organic Electrode for Sustainable Li-Ion Batteries, *ChemSusChem.* 2008 1 348–355.
95. Song Z, Zhou H. Towards sustainable and versatile energy storage devices: an overview of organic electrode materials. *Energy Environ. Sci.* 2013 6 2280.
96. Song Z, Qian Y, Gordin M L, Tang D, Xu T, Otani M, Zhan H, Zhou H, Wang D. Polyanthraquinone as a Reliable Organic Electrode for Stable and Fast Lithium Storage. *Angew. Chem.* 2015 54 13947–13951. doi:10.1002/anie.201506673.
97. Strakhov A, Pushkareva Z. Heterocyclic N-oxides. IX. Preparation and properties of some heterocyclic N-oxides with condensed rings, *Trudy Ural'skogo Politekhnikheskogo Instituta im. S. M. Kirova.* 94 (1960) 34–44.
98. Eistert B, Fink H, Werner H K. Phenazin-Derivate aus Rhodizonsäure, *Liebigs Ann.* 1962 657 131–141.

99. Halls M D, Djurovich P J, Giesen D J, Goldberg A, Sommer J, McAnally E, Thompson M E. Virtual screening of electron acceptor materials for organic photovoltaic applications. *New J. Phys.* 2013 15 105029.
100. Tang X D, Liao Y, Geng H, Shuai Z G. Fascinating effect of dehydrogenation on the transport properties of N-heteropentacenes: transformation from p- to n-type semiconductor. *J. Mater. Chem.* 22 2012 18181.
101. Ma Y, Sun Y, Liu Y, Gao J, Chen S, Sun X, Qiu W, Yu G, Cui G, Hu W, Zhu D. Organic thin film transistors based on stable amorphous ladder tetraazapentacenes semiconductors. *J. Mater. Chem.* 2005 15 4894.
102. Wu J I, Wannere C S, Mo Y, von P, Schleyer R, Bunz U H F. $4n \pi$ Electrons but Stable: N , N -Dihydrodiazapentacenes. *J. Org. Chem.* 2009 74 4343–4349.
103. Thompson M E, Saris P, Djurovich P I, Chen S. Host materials and ligands for dopants in organic light emitting diodes. WO Patent 2015 066244.
104. Miao Q, Liu D, He Z. Self-assembled monolayers of phosphonic acids as dielectric surfaces for high-performance organic thin film transistors. WO Patent 2015 189701.
105. Schnurpfeil G, Löffler F, Hild O R, Tsaryova O, Gerdes R, Wöhrle D, Gorun S M. Doped semiconductor material and use thereof. WO Patent (2009) 021663.
106. Katakura R, Tanaka T, Hirai K, Kita H. Organic thin-film transistor material, organic thin-film transistor, field effect transistor, switching device, organic semiconductor material, and organic semiconductor film. WO Patent 2006 059486.

107. Sutton C, Risko C, Brédas J L. Noncovalent Intermolecular Interactions in Organic Electronic Materials: Implications for the Molecular Packing vs Electronic Properties of Acenes, *Chem. Mater.* 2016 28 3–16.
108. Martin R. Electrodes for energy storage devices. WO Patent 2015 097197.
109. Xiao N, McCulloch W D, Wu Y. Reversible Dendrite-Free Potassium Plating and Stripping Electrochemistry for Potassium Secondary Batteries. *J. Am. Chem. Soc.* 2017 139 9475–9478.
110. Chen Y, Luo W, Carter M, Zhou L, Dai J, Fu K, Lacey S, Li T, Wan J, Han X, Bao Y, Hu L, Organic electrode for non-aqueous potassium-ion batteries, *Nano Energy.* 2015 18 205–211.
111. Jian Z, Liang Y, Rodríguez-Pérez I A, Yao Y, Ji X. Poly(anthraquinonyl sulfide) cathode for potassium-ion batteries. *Electrochem. Comm.* 2016 71 5–8.
112. Fei H, Liu Y, An Y, Xu X, Zeng G, Tian Y, Ci L, Xi B, Xiong S, Feng J. Stable all-solid-state potassium battery operating at room temperature with a composite polymer electrolyte and a sustainable organic cathode. *J. Power Sources.* 2018 399 294–298.
113. Fan L, Liu Q, Xu Z, Lu B. An Organic Cathode for Potassium Dual-Ion Full Battery, *ACS Energy. Lett.* 2017 2 1614–1620.
114. Chen L, Liu S, Wang Y, Liu W, Dong Y, Kuang Q, Zhao Y. Ortho-di-sodium salts of tetrahydroxyquinone as a novel electrode for lithium-ion and potassium-ion batteries, *Electrochim. Acta.* 2019 294 46–52.
115. Fan L, Ma R, Wang J, Yang H, Lu B. An Ultrafast and Highly Stable Potassium-Organic Battery. *Adv. Mater.* 2018 30 1805486.

116. Pramudita J C, Sehwat D, Goonetilleke D, Sharma N. An Initial Review of the Status of Electrode Materials for Potassium-Ion Batteries. *Adv. Energ. Mater.* 2017 7 1602911.
117. Kim H, Kim J C, Bianchini M, Seo D H, Rodriguez-Garcia J, Ceder G. Recent Progress and Perspective in Electrode Materials for K-Ion Batteries. *Adv. Energ. Mater.* 2018 8 1702384.
118. Kapaev R R, Troshin P A. Organic-based active electrode materials for potassium batteries: status and perspectives. *J. Mater. Chem. A.* 2020 8 17296–17325.
119. Xu S, Chen Y, Wang C. Emerging organic potassium-ion batteries: electrodes and electrolytes. *J. Mater. Chem. A.* 2020 8 15547–15574.
120. Slesarenko A, Yakuschenko I K, Ramezankhani V, Sivasankaran V, Romanyuk O, Mumyatov A V, Zhidkov I, Tsarev S, Kurmaev E Z, Shestakov A F, Yarmolenko O V, Stevenson K J, Troshin P A. New tetraazapentacene-based redox-active material as a promising high-capacity organic cathode for lithium and potassium batteries. *J. of Power Sources.* 2019 435 226724.
121. Zhao Q, Wang J, Lu Y, Li Y, Liang G, Chen J. Oxocarbon Salts for Fast Rechargeable Batteries. *Angew. Chem. Int. Ed.* 2016 55 12528–12532.
122. Yang S Y, Chen Y J, Zhou G, Fu Z W. Multi-Electron Fused Redox Centers in Conjugated Aromatic Organic Compound as a Cathode for Rechargeable Batteries. *J. Electrochem. Soc.* 2018 165 A1422–A1429.
123. Lu Y, Zhang Q, Li L, Niu Z, Chen J. Design Strategies toward Enhancing the Performance of Organic Electrode Materials in Metal-Ion Batteries. *Chem.* 2018 4 2786–2813.

124. Tong Z, Tian S, Wang H, Shen D, Yang R, Lee C. Tailored Redox Kinetics, Electronic Structures and Electrode/Electrolyte Interfaces for Fast and High Energy-Density Potassium-Organic Battery, *Adv. Funct. Mater.* 2020 30 1907656.
125. Westman K, Dugas R, Jankowski P, Wieczorek W, Gachot G, Morcrette M, Irisarri E, Ponrouch A, Palacín M R, Tarascon J M, Johansson P. Diglyme Based Electrolytes for Sodium-Ion Batteries. *ACS Appl. Energy Mater.* 2018 1 2671–2680.
126. Huang J, Lin X, Tan H, Zhang B. Bismuth Microparticles as Advanced Anodes for Potassium-Ion Battery. *Adv. Energy Mater.* 2018 8 1703496.
127. Katorova N S, Fedotov S S, Rupasov D P, Luchinin N D, Delattre B, Chiang Y M, Abakumov A M, Stevenson K J. Effect of Concentrated Diglyme-Based Electrolytes on the Electrochemical Performance of Potassium-Ion Batteries. *ACS Appl. Energy Mater.* 2019 2 6051–6059.
128. Junek H, Unter B, Peltzmann R. Notizen: Eine einfache Synthese von Tetrahydroxybenzochinon-1.4 / A Simple Synthesis of Tetrahydroxy-benzoquinone- 1,4, *Zeitschrift Für Naturforschung B.* 1978 33 1201–1203.
129. Liu J, Wang J, Xu C, Jiang H, Li C, Zhang L, Lin J, Shen Z X. Advanced Energy Storage Devices: Basic Principles, Analytical Methods, and Rational Materials Design. *Adv. Sci.* 2018 5 1700322.
130. Obrezkov F A, Ramezankhani V, Zhidkov I, Traven V F, Kurmaev E Z, Stevenson K J, Troshin P A. High-Energy and High-Power-Density Potassium Ion Batteries Using Dihydrophenazine-Based Polymer as Active Cathode Material. *J. Phys. Chem. Lett.* 2019 10 5440–5445.

131. Liang Y, Tao Z, Chen J. Organic electrode materials for rechargeable lithium batteries, *Adv. Energy Mater.* 2012 2 742–769.
132. Taletskiy K S, B Sorovkov V I, Schegoleva L N, Beregovaya I V, Taratayko A I, Molin Y N. Radical cationic pathway for the decay of ionized glyme molecules in liquid solution, *J. Phys. Chem. B.* 2015 119 14472–14478.
133. Peled E, Menkin S, Review—SEI: past, present and future, *J. Electrochem. Soc.* 2017 164 A1703–A1719.
134. Kapaev R R, Stevenson K J. Solution-based chemical pre-alkaliation of metal-ion battery cathode materials for increased capacity. *J Mater Chem A.* 2021 9 11771–11777.
135. Han C, Li H, Shi R, Zhang T, Tong J, Li, B. Li J. Organic quinones towards advanced electrochemical energy storage: Recent advances and challenges, *J. Mater. Chem. A.* 2019 7 23378–23415.
136. Tian B, Zheng J, Zhao C, Liu C, Su C, Tang W, Li X, Ning G H. Carbonyl-based polyimide and polyquinoneimide for potassium-ion batteries, *J. Mater. Chem. A.* 2019 7 9997–10003.
137. Shestakov A F, Romanyuk O E, Mumyatov A V, Luchkin S Y, Slesarenko A A, Yarmolenko O V, Stevenson K J, Troshin P A. Theoretical and experimental evidence for irreversible lithiation of the conformationally flexible polyimide: Impact on battery performance. *J. Electroanal. Chem.* 836 (2019) 143–148,
138. Ignatova A A, Kozlov A V, Shestakov A F, Chernyak A V, Yarmolenko O V, Troshin P A. Insight in the degradation of polyquinone-based cathode material in lithium-organic battery under cycling, *Mendeleev Communications.* 2017 27 524–526.

139. Kapaliev R R, Olthof S, Zhidkov I S, Kurmaev E Z, Stevenson K J, Meerholz K, Troshin P A. Nickel(II) and Copper(II) coordination polymers derived from 1,2,4,5-Tetraaminobenzene for Lithium-Ion Batteries. *Chem. Mater.* 2019 31 5197–5205.
140. Dou J H, Sun L, Ge Yi, Li w, Hendon C H, Li J, Gul S, Yano J, Stach E A. Signature of metallic behavior in the metal-organic frameworks $M_3(\text{hexaiminobenzene})_2$ ($M = \text{Ni, Cu}$) *Am. Chem. Soc.* 2017 139 13608–13611,
141. Peng C, Ning G H, Su J, Zhong G, Tang W, Tian B, Su C, Yu Di, Zu L, Yang J, Ng M F, Hu Y S, Yang Y, Armand M and Loh K P. Reversible multi-electron redox chemistry of π -conjugated N-containing heteroaromatic molecule-based organic cathodes. *Nat. Energy.* 2017 2 17074.
142. Wu S, Wang W, Li M, Cao L, Lyu F, Yang M, Wang Z, Shi Y, Nan B, Yu S, Sun Z, Liu Y and Lu Z. Highly durable organic electrode for sodium-ion batteries via a stabilized α -C radical intermediate. *Nat. Commun.* 2016 7 13318.
143. Thangavel R, Ponraj R, Kannan A G, Kaliyappan K, Kim D W, Chen Z and Lee Y S. High performance organic sodium-ion hybrid capacitors based on nano-structured disodium rhodizonate rivaling inorganic hybrid capacitors. *Green Chem.* 2018 20 4920–4931
144. B. Flamme, B. Jismy, M. Abarbri and M. Anouti. Poly-anthraquinone sulfide isomers as electrode materials for extended operating temperature organic batteries. *Mater. Adv.* 2021 2 376–383.
145. Y. Hu, W. Tang, Q. Yu, X. Wang, W. Liu, J. Hu, and C. Fan. Novel Insoluble Organic Cathodes for Advanced Organic K-Ion Batteries. *Adv. Funct. Mater.* 2020, 2000675.

146. Xie K, Yuan K, Li X, Lu W, Shen C, Liang C, Vajtai R, Ajayan P and Wei B. Superior Potassium Ion Storage via Vertical MoS₂ “Nano-Rose” with Expanded Interlayers on Graphene. *Small*, 2017 13 1701471.
147. Zhang C., Qiao Y., Xiong P., Ma W., Bai P., Wang X., Li Q, Zhao J., Xu Y., Chen Y., Zeng H., Wang F., Xu Y., and Jiang J-X. Conjugated Microporous Polymers with Tunable Electronic Structure for High-Performance Potassium-Ion Batteries. *ACS Nano* 2019, 13, 745–754.
148. Kapaev R. R, Zhidkov I.S., Kurmaev E., Stevenson K.J. and Troshin P. A. A nickel coordination polymer derived from 1,2,4,5-tetraaminobenzene for fast and stable potassium battery anodes. *Chem. Commun.*, 2020,56, 1541-1544.
149. Bai Y., Fu W., Chen W., Chen Z., Pan X., Lv X., Wu J. and Pan X. Perylenetetracarboxylic diimide as a high-rate anode for potassium-ion batteries. *J. Mater. Chem. A*, 2019, 7, 24454-24461.
151. Xu B., Qi S., Li F., Peng X., Cai J., Liang J., Ma J. Cotton-derived oxygen/sulfur co-doped hard carbon as advanced anode material for potassium-ion batteries. *Chin. Chem. Lett.*, 2020, 31, 217-222.
152. Obrezkov F. A, Ramezankhani V., Traven V. F., Kurmaev E. Z., Stevenson K. J., Troshin P. A., High-energy and high-power-density potassium ion batteries using dihydrophenazine-based polymer as active cathode material. *J. Phys. Chem. Lett.* 2019, 10, 5440–5445.

152. Xue L, Li Y, Gao H, Zhou W, Lü X., W. Kaveevivitchai W., Manthiram A, Goodenough J B. Low-Cost High-Energy Potassium Cathode. *J. Am. Chem. Soc.* 2017, 139 (6), 2164–2167
153. Kapaev R R and Troshin P A. Organic-based active electrode materials for potassium batteries: status and perspectives. *J Mater. Chem. A.* 2020 8 17296–17325.
154. Hosaka T, Kubota K, Hameed A S and Komaba S. Research Development on K-Ion Batteries. *Chem Rev.* 2020 120 6358–6466.
155. Tan H, Du X, Huang J Q and Zhang B. KVPO₄F as a novel insertion-type anode for potassium ion batteries. *Chem. Commun.*, 2019 55 11311–11314.
156. Bao J, Deng W, Liu J and Sun C. F. Ultrafast-kinetics, ultralong-cycle-life, bifunctional inorganic open-framework for potassium-ion batteries. *Energy Storage Mater.*, 2021, 42, 806–814.
157. Han J, Niu Y, Bao S. J, Yu Y. N, Lu S. Y and Xu M. Nanocubic KTi₂(PO₄)₃ electrodes for potassium-ion batteries. *Chem. Commun.* 2016, 52, 11661–11664.
158. Elgrishi N, Rountree K J, McCarthy B D, Rountree E C, Eisenhart T T, and. Dempsey J L. A Practical Beginner's Guide to Cyclic Voltammetry. *J. Chem. Educ.* 2018, 95, 2, 197–206.
159. Zhang J, Lai L, Wang H, Chen M, Shen Z X. Energy storage mechanisms of anode materials for potassium ion batteries. *Mater. Today Energy.* 2021, 21, 100747.

Appendices A

A.1 Materials and instrumentation

Chemicals and solvents were purchased from Sigma-Aldrich and used as received. A CHNS/O elemental analyzer «Vario Micro cube» Elementar GmbH was used to do Chemical analysis. FTIR spectra were recorded with PerkinElmer Spectrum BX 100 instrument. The Bruker AVANCE III spectrometer operating at 400 MHz for ^1H and 101 MHz for ^{13}C was used to conduct solid-state NMR experiments. A 3.2 mm MAS probe was utilized at room temperature. The chemical shifts were measured relative to TMS at 0 ppm. To acquire the ^{13}C NMR spectra, conventional cross-polarization (CP) experiments were employed with a spinning rate of 14-16 kHz and ^1H SPINAL-64 decoupling. The duration of the ^1H $\pi/2$ pulse was 2.5 μs , and the contact time was set at 1000 μs .

A.2 Synthesis of OHTAP

The solution of 1.67 g (8 mmol) of 1 in the form of dihydrate in 45 mL of 10% aqueous acetic acid was warmed up to 60-70 °C. Afterwards, the solution of 1.08 g (3.8 mmol) of 1,2,4,5-tetraaminobenzene dihydrochloride in 10 mL of 10% aqueous acetic acid was added dropwise. The resulting mixture was stirred at the temperature of 60-70 °C within 6 h. Cooling the reaction mixture resulted in the formation of a solid precipitate, which was

collected by filtration and washed with water (until washing liquids became colorless), methanol and acetone. The resulting solid was dried in a vacuum desiccator with phosphorous pentaoxide. The target **OHTAP** was obtained in the form of tetrahydrate with the yield of 1.51 g (~91%). No melting was detected for **OHTAP** up to the temperature of 320°C. FTIR spectrum (ν , cm^{-1}): 3544, 3506, 3316, 3261, 3123, 1629, 1567, 1356, 1299, 1268, 1152, 1035, 879, 850, 741, 715. Elemental analysis: calculated for $\text{C}_{18}\text{H}_{10}\text{N}_4\text{O}_8 \cdot (\text{H}_2\text{O})_4$, %: C 44.82, H 3.76, N 11.62; found, %: C 44.40, H 3.62, N 11.89.

A.3 Synthesis of OHTAPQ

The mixture of N-methylpyrrolidone (40 ml) and sulfuric acid (1 ml) was heated up to 180 °C and then 1.5 g (8.9 mmol) of 2,3,5,6-tetraamino-1,4-benzoquinone and 3.07 g (17.8 mmol) of tetrahydroxy-1,4- benzoquinone dihydrate were successively added. The combination was agitated at the identical temperature for a duration of 5 hours. Following the cooling process, the mixture was thinned out with an equal amount of water (60 ml). The solid substance was separated by filtration, then rinsed with water until the washings were colourless (150 ml) and acetone (20 ml). Finally, it was left to dry in the air. Then the precipitate was vigorously suspended in hot acetone (45–50 °C) and collected by filtration, this procedure was repeated 3 times. Finally, the precipitate was dried in a vacuum over P_2O_5 to produce 1.77 g of the target compound **OHTAPQ**. The isolated yield was 45%. Elemental analysis calcd. for $\text{C}_{18}\text{H}_8\text{N}_4\text{O}_{10}$ (% w/w): C – 49.10, H – 1.83, N – 12.73, found (% w/w): C – 49.23, H – 1.78, N – 12.68. FTIR spectrum (cm^{-1}): 630 w, 669 w, 742 w, 814

w, 867 w, 928 m, 1001 s, 1094 s, 1169 s, 1222 s, 1299 vs, 1336 vs, 1459 s, 1505 s, 1565 s, 1635 s ¹³C SS MAS NMR (ppm): 173.0, 168.9, 150.0, 135.2, 134.6, 132.6, 123.7.

A.4 Synthesis of polymers P1-P6

A.4. 1. Synthesis of P1

3,3'-Diaminobenzidine (1.29, 6 mmol) was added to a suspension of 1.98 g (6 mmol) of triquinoyl hydrate in 100 ml of glacial AcOH stirred at 60 °C. The mixture was further stirred for 1 h at 60 °C and then another 5 h at 100–105 °C. After cooling, a brown precipitate was filtered off, washed on a filter successively with 30 ml of ice-cold AcOH, 30 ml of 10% aqueous AcOH, 50 ml of water and 30 ml of methanol. The remaining powder was dried at room temperature in vacuum over P₂O₅. The crude product (2.00 g) was further stirred with 50 ml of DMF at 80–85 °C for 4 hours, filtered and successively washed on the filter with 150 ml (5 x 30 ml) of hot DMF, 150 ml (5 x 30 ml) of methanol and 150 ml (5 x 30 ml) of acetone. After drying at room temperature in a vacuum over phosphorous anhydride, the compound **P1** (1.89 g) was annealed in a vacuum at 180 °C for 4 h to remove the hydrated water. The target compound **P1** was obtained with a yield of 1.67 g (~90% of the theoretical yield). FTIR spectrum (ν , cm⁻¹): 3392, 1710, 1616, 1492, 1361, 1195, 1086, 1061, 890, 832, 789. Elemental analysis: calculated for C₁₈H₁₂N₄O₅, %: C 59.34, H 3.32, N 15.38, O 21.96; found, %: C 60.43, H 3.72, N 15.80.

A.4.2 Synthesis of polymer P2

1,2,4,5-Tetraaminobenzene tetrahydrochloride (0.92 g, 3.24 mmol) was added to a suspension of 1.07 g (3.24 mmol) of triquinoyl hydrate in 50 ml of glacial AcOH stirred at 50 °C. The mixture was stirred at the same temperature for 1 h, then 1.06 g (12.93 mmol) of anhydrous sodium acetate was added and the reaction mixture was stirred at 100–105 °C for another 5 h. After cooling down, 50 ml of water were introduced into the reaction mixture, and the resultant solid that formed was separated by filtration. The unrefined substance was rinsed on the filter using water until the liquid that passed through became colorless, and then it was dried in a vacuum with P₂O₅. The desiccated unprocessed material, weighing 0.85 g, was mixed with 35 ml of DMF at a temperature of 80–85 °C for a duration of 4 h. Following the cooling process, the solid that precipitated was gathered through filtration and subjected to sequential washing on the filter using 150 ml (in five 30 ml portions) of DMF, 150 ml (in five 30 ml portions) of methanol, and 150 ml (in five 30 ml portions) of acetone. It was then dried in a vacuum at room temperature with phosphorous anhydride.

The resulting powder (0.66 g) was annealed in a vacuum at 150 °C for 5 h. The target compound **P2** was obtained with a yield of 0.55 g (73% of the theoretical). FTIR spectrum (ν , cm⁻¹): 3204, 1621, 1469, 1354, 1252, 1051, 881, 752. Elemental analysis: calculated for C₁₂H₆N₄O₄, %: C 53.34; H 2.24; N, 20.74; O 23.69; found, %: C 52.83; H 2.44; N 22.53.

A.4.3 Synthesis of polymer P3

2,6-Diaminoantraquinone (1.43 g, 6.0 mmol) and triquinoyl hydrate (0.99 g, 3.0 mmol) were successively added to a mixture of N-methylpyrrolidone (30 ml) and glacial AcOH (30 ml) stirred at 45-50 °C. The mixture was stirred at the same temperature for 1 h and then at 100-110 °C for another 5 h. After cooling, the reaction mixture was diluted with an equal volume of water (60 ml), the precipitate was filtered off, washed with water until the filtrate becomes colorless (150 ml) followed by acetone (20 ml) and dried in air. The crude product (1.49 g) was suspended in 30 ml of dimethylformamide, stirred 1 h at 55-60 °C and the precipitate was isolated by filtration; this procedure was repeated three times. Afterward, the crude product was treated three times with acetone in the same way at 45-50 °C. After drying in vacuum over phosphorous anhydride, the target product **P3** was obtained with a yield of 0.82 g (24% of the theoretical). FTIR spectrum (ν , cm^{-1}): 3427, 3321, 3202, 1659, 1623, 1565, 1359, 1322, 1284, 1153, 890, 840, 740, 660, 546. Elemental analysis: calculated for $\text{C}_{34}\text{H}_{14}\text{N}_4\text{O}_7$, %: C 67.10; H 2.63; N, 9.21, found, %: C 68.50; H 4.29; N, 11.06.

A.4.4 Synthesis of polymer P4

p-Phenylenediamine (0.86 g, 8 mmol) was added in one portion to the suspension of 2.50 g (8 mmol) of triquinoyl hydrate in 150 ml of glacial acid stirred at 60 °C. The mixture was stirred at a temperature range of 60-65 °C for 2 hours, followed by an additional 5 hours at a temperature range of 100-110 °C. After cooling, 150 ml of water was introduced and the

mixture was stirred for 2 hours at room temperature. The resulting solid was separated by filtration. The filtrate was washed on the filter with water until the filtrate became colourless, followed by methanol (50 ml) and acetone (50 ml). Polymer **P4** was obtained in the form of a hydrate (three water molecules per polymer unit) with a yield of 1.10 g (56% of the theoretical value). FTIR spectrum (ν , cm^{-1}): 3442, 2978, 2636, 1579, 1459, 1409, 1172, 1059, 1026. Elemental analysis, found, %: C 50.51; H 3.90; N 9.78.

A.4.5 Synthesis of polymer P5

p-Phenylenediamine 1.30 g (12 mmol) was added in one portion to a suspension of 1.98 g (6 mmol) of triquinoyl hydrate in 100 ml of glacial AcOH stirred at 50-60 °C. The mixture was stirred at the same temperature for 1 h and then at 100 °C for another 5 h. After cooling, the reaction mixture was diluted with an equal volume of water and the formed precipitate was isolated by filtration. The crude product was washed on the filter with water until the filtrate became colorless, dried in air to a constant weight (1.81 g). Then, the material was stirred with 60 ml of DMF at 50-60 °C for 5 h, the solids were filtered off and successively washed on the filter with 150 ml (5 x 30 ml) of DMF, 150 ml (5 x 30 ml) of methanol, 150 ml (5 x 30 ml) of acetone. The residue was dried in a vacuum over phosphorous anhydride at room temperature and then additionally at 150–160 °C in a vacuum oven for 5 h. The target product **P5** was obtained with a yield of 1.09 g (60% of the theoretical value). FTIR spectrum (ν , cm^{-1}): 3317, 1675, 1603, 1513, 1407, 1314, 1252, 1175, 1019, 827. Elemental analysis, found, %: C 56.68; H 4.20; N 13.68.

A.4.6 Synthesis of polymer P6

p-Phenylenediamine 1.08 g (18 mmol) was added in one portion to a suspension of 1.98 g (6 mmol) of triquinoyl hydrate in 120 ml of glacial AcOH stirred at 50 °C. The mixture was stirred at the same temperature for 1 h and then at 100-105 °C for another 5 h. After cooling, the reaction mixture was diluted with an equal volume of water and the formed precipitate was isolated by filtration. The crude product was washed on the filter with water until the filtrate became colorless and dried in air to a constant weight (1.38 g). Then, the material was stirred with 60 ml of DMF at 70-80 °C for 5 h, the solids were filtered off and successively washed on the filter with 150 ml (5 x 30 ml) of DMF, 150 ml (5 x 30 ml) of methanol, and 150 ml (5 x 30 ml) of acetone. The residue was dried in a vacuum over phosphorous anhydride at room temperature and then additionally at 160–170 °C in a vacuum oven for 5 h. The target product **P6** was obtained with a yield of 0.82 g (36% of the theoretical value). FTIR spectrum (ν , cm^{-1}): 3052, 1670, 1601, 1512, 1407, 1312, 1244, 1176, 1059, 1023, 974, 829. Elemental analysis, found, %: C 57.75; H 4.11; N 14.22.

A. 5 Synthesis of polymers P7-P9

A.5.1 Synthesis of P7

Polyhydroquinonemethylene (PHQM) was synthesized according to the previously published procedure. Briefly, 5.5 g (50 mmol) of hydroquinone and 2.3 g (75 mmol) of

paraformaldehyde were dissolved in 25 ml of acetic acid. Then, 0.1 ml of sulfuric acid was added and the resulting mixture was heated at reflux for 3 h. The dark precipitate was isolated by filtration and washed repeatedly with water (1.5–2.0 L). Afterward, the powder was dried in a vacuum oven at 100 °C overnight. Yield 6.0 g (98%). Polythiopyranoquinone (**P7**) was synthesized following a similar procedure reported by A. A. Berlin A finely ground mixture of 5.8 g (180 mmol) of sulfur, 2 g (16 mmol) of PHQM and 0.4 g (1.6 mmol) of iodine was heated under an inert argon atmosphere at 250 °C and stirred for 60 h. Then, the reaction mass was dissolved in carbon disulfide. The polymer was separated from the sulfur solution by filtration and washed with N-methylpyrrolidone (NMP) in a Soxhlet apparatus. Yield 2.4 g (96%). FTIR spectrum (ν , cm^{-1}): 2924 (w), 2854 (w), 1606 (st), 1424 (st), 1223 (st), 1054 (w), 871 (w), 670 (mid), 589 (w). Elemental analysis calculated for $\text{C}_7\text{S}(\text{OH})_2$, %: C 55.99, H 1.34, S 21.38; found %: C 55.23, H 1.62, S 21.44. SS MAS ^{13}C NMR spectrum: 179.1, 150.4, 125.3, 28.4 ppm.

A.5.2 Synthesis of P8

The synthesis was carried out by sintering bromanilic acid following the procedure reported by A. A. Berlin et al. Bromanilic acid (3 g, 10 mmol) was subjected to pyrolysis at 250 °C in an argon atmosphere for 1 h. The resulting dark powder was washed repeatedly with NMP in a Soxhlet apparatus. The yield of insoluble in NMP fraction of **P8** was 0.8 g (59%). FTIR spectrum (ν , cm^{-1}): 1730 (mid), 1618 (st), 1548 (mid), 1429 (w), 1354 (w), 1264 (w), 1122 (w), 670 (mid), 582 (w). Elemental analysis calculated for calculated for

C₆O₄, %: C 52.96, H 0; found, %: C 52.4%, H 0.74%; SS MAS ¹³C NMR spectrum: 152.4, 139.5, 113.6 ppm.

A.5.3 Synthesis of P9

To synthesize 2,5-diamino-3,6-dibromo-1,4-benzoquinone, 5 g (11.8 mmol) of bromanil and 120 ml of ethanol are placed in a two-necked round-bottom flask equipped with a gas inlet tube and a reflux condenser. A flow of dry ammonia was passed for 30 min through the solution, which was heated at reflux. The formed red crystalline precipitate was filtered off, washed with water and alcohol and dried in a vacuum. The yield of 2,5-diamino-3,6-dibromo-1,4-benzoquinone was 3 g (86%). Elemental analysis calculated for C₆N₂(OH)₂: C 24.35%, H 1.36%, N 9.47%; found %: C 25.45%, H 1.43%, N 9.16%. At the second stage, the 2,5-diamino-3,6-dibromo-1,4-benzoquinone (2.5 g, 8 mmol) was dissolved in 30 ml of NMP and heated at reflux for 3 days. The precipitated black precipitate was filtered off, washed with NMP, ethyl alcohol and water. Then the resulting powder was vigorously shaken with bromine water (25 mL) four times. The product was separated by filtration and washed with water and ethanol. The yield was 0.8 g (71%). FTIR spectrum (ν, cm⁻¹): 1624 (st), 1438 (w), 1382 (w), 1282 (w), 850 (w), 746 (w), 614 (w). Elemental analysis calculated for C₆N₂O₂, %: C 54.56%; H 0%; N 21.21%; found %: C 53.75, H 0.149%, N 21.66%. SS MAS ¹³C NMR spectrum: 164.0, 154.3, 135.6 ppm.

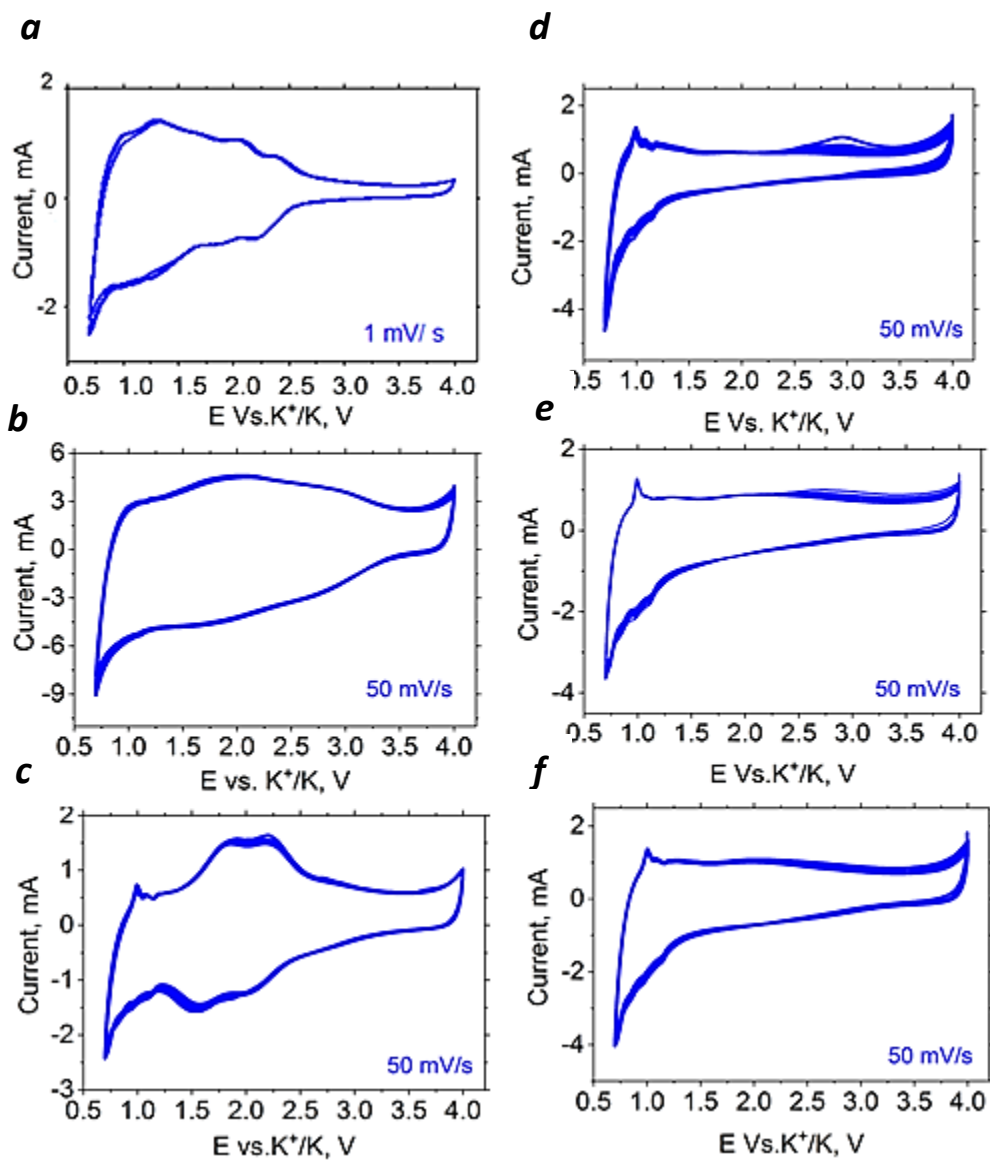


Fig. A.1 Cyclic voltammograms of **P1** (a), **P2** (b), **P3** (c), **P4** (d), **P5** (e) and **P6** (f) in half-cells with potassium anodes after galvanostatic pre-conditioning at 0.5 A g^{-1} for a number of cycles required to reach stable capacity after initial activation period.

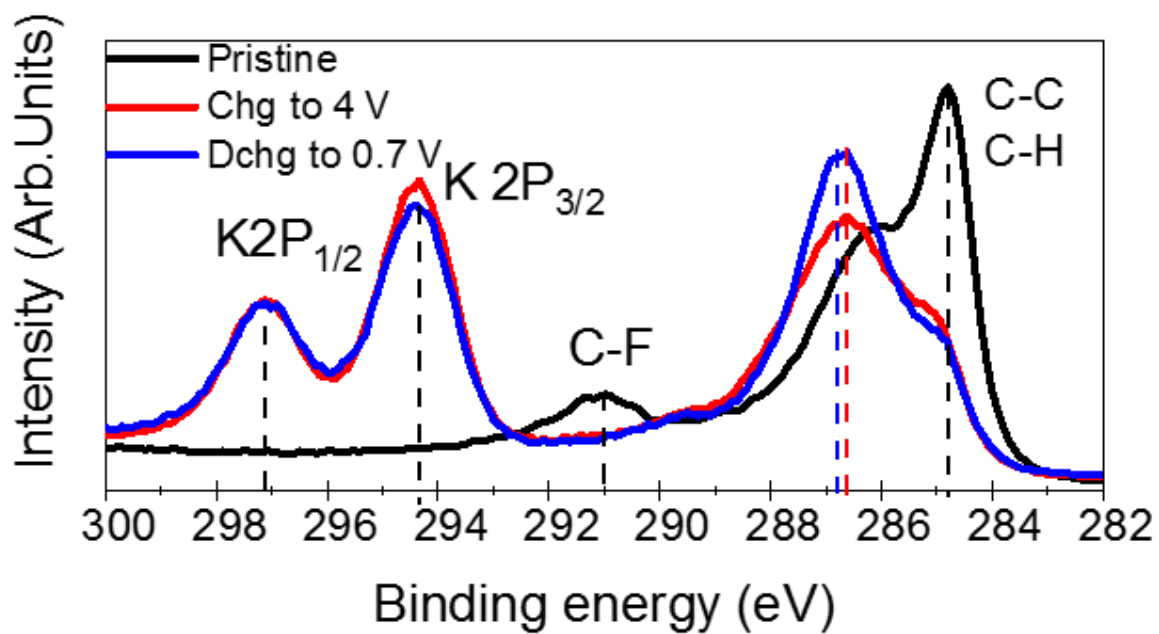


Fig. A.2 High-resolution core-level C 1s and K 2P XPS spectra of **P1**-based electrode in a pristine state, after first charge to 4 V and after discharge to 0.7 V vs. K⁺/K.

Table A.1 The calculated metallation energies δE_{2n} for models of polymes P1, P2, and P4* given in eV per introduced K⁺ ion. The energies estimated for supramolecular dimers of the fully metallated structures are given in parenthesis.

n	P1	P2	P4*
2	1.66	1.58	2.03
4	1.05	0.97	1.17
6	0.73 (1.53)	0.67 (1.46)	0.87 (1.95)

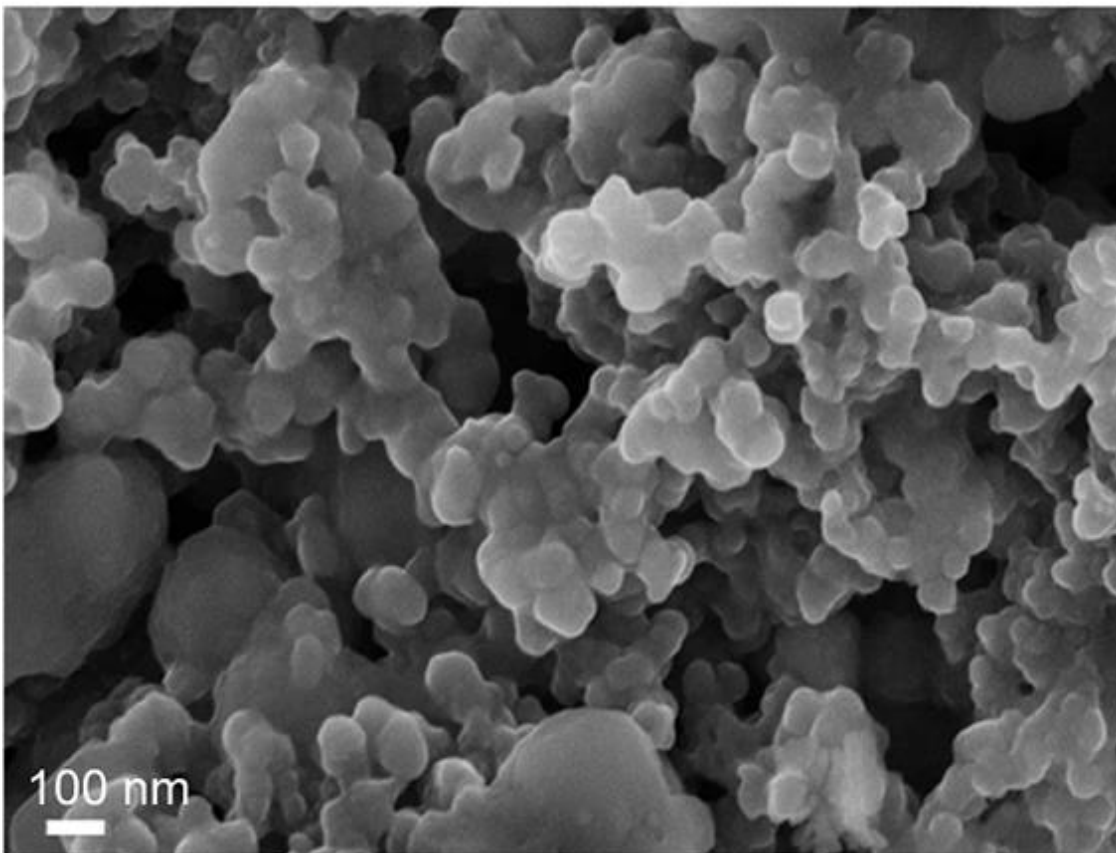


Fig. A.3 SEM image of the composite electrode comprised of polymer **P1** after 400 charge-discharge cycles at 0.5 A g⁻¹ using 2.2 M KPF₆ in diglyme as electrolyte.

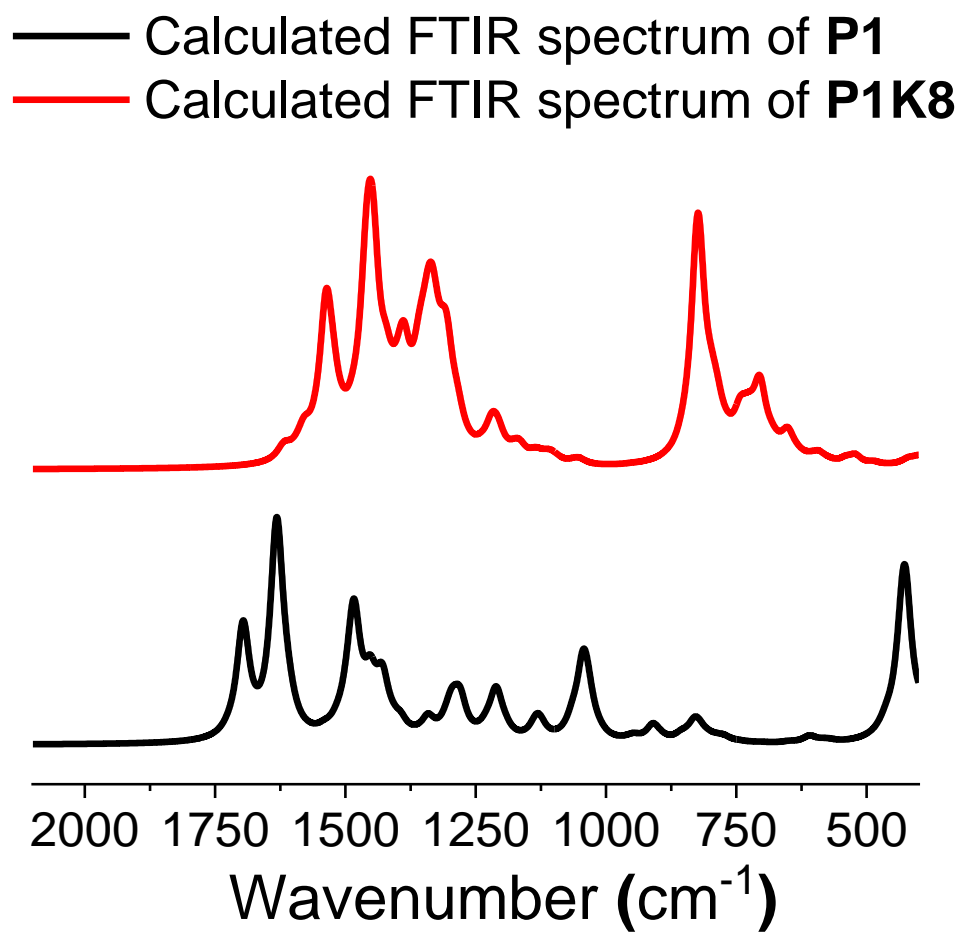


Fig. A.4 The comparison of the DFT calculated FTIR spectra of **P1** and its fully metallated form **P18K**.

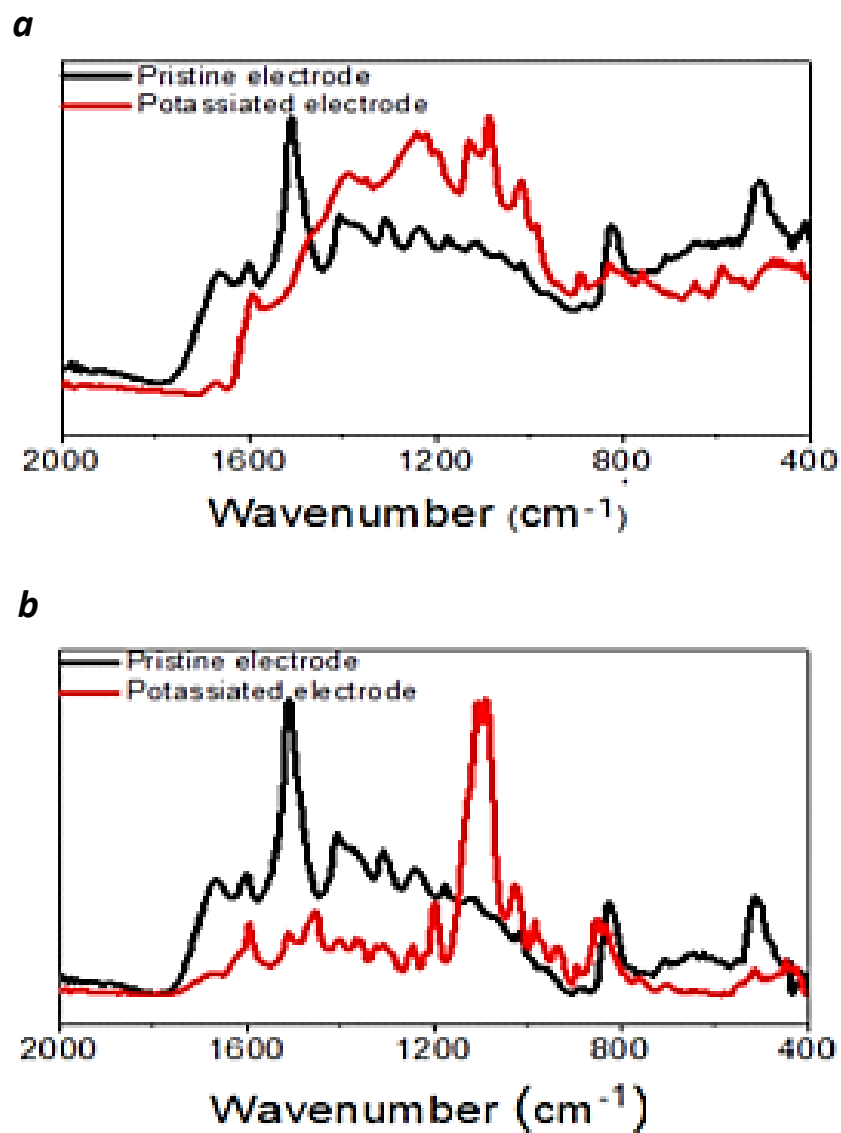


Fig. A.5 ATR FTIR spectra of pristine and potassiated electrodes comprised of polymers **P2** (a) and **P4** (b).

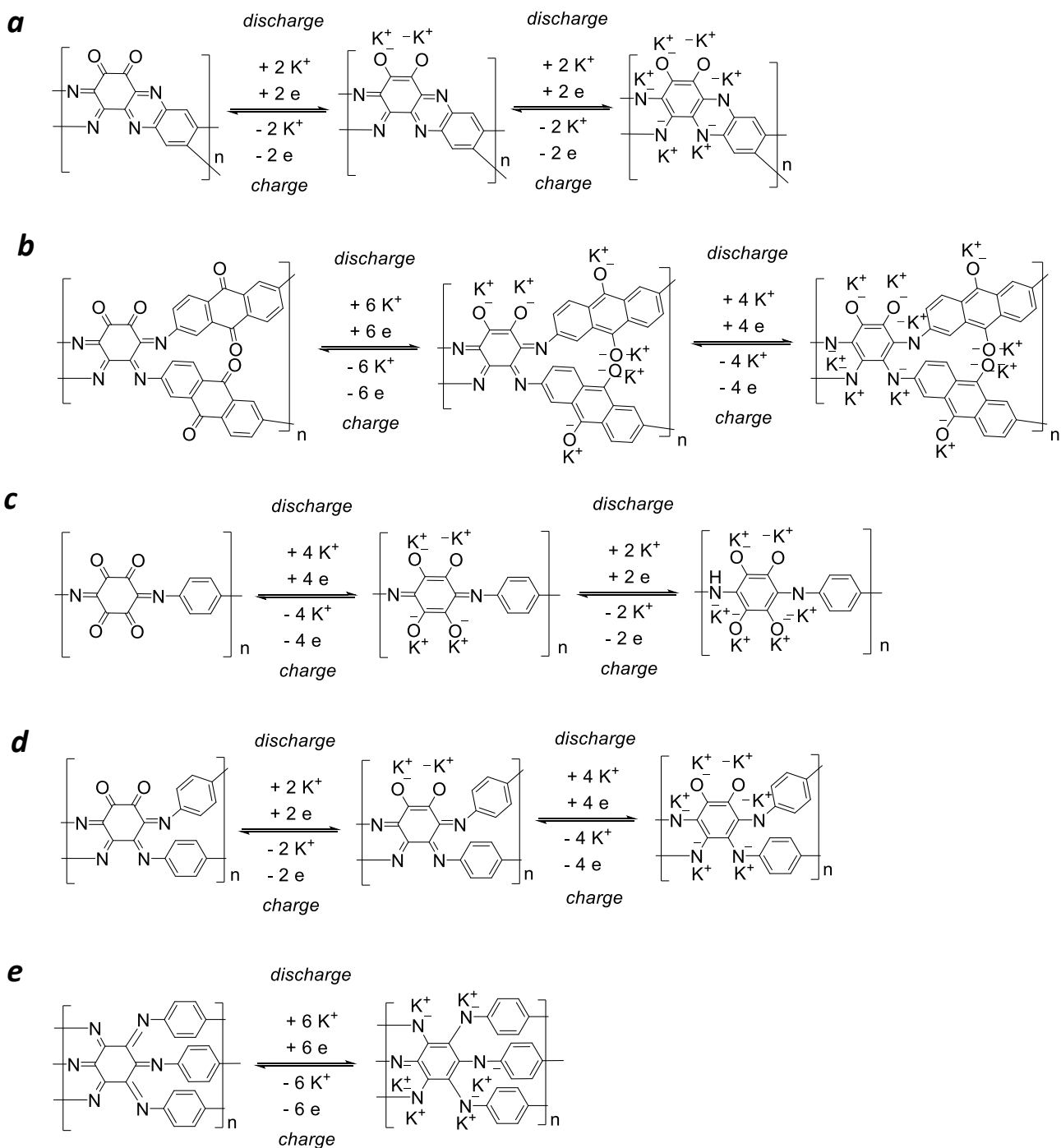


Fig. A.6 Redox transformations of P2 (a), P3 (b), P4* (c), P5* (d) and P6* (e) upon charging and discharging of potassium half-cells. The model molecular structures P4*, P5* and P6* were selected due to the reasons explained in the main text.

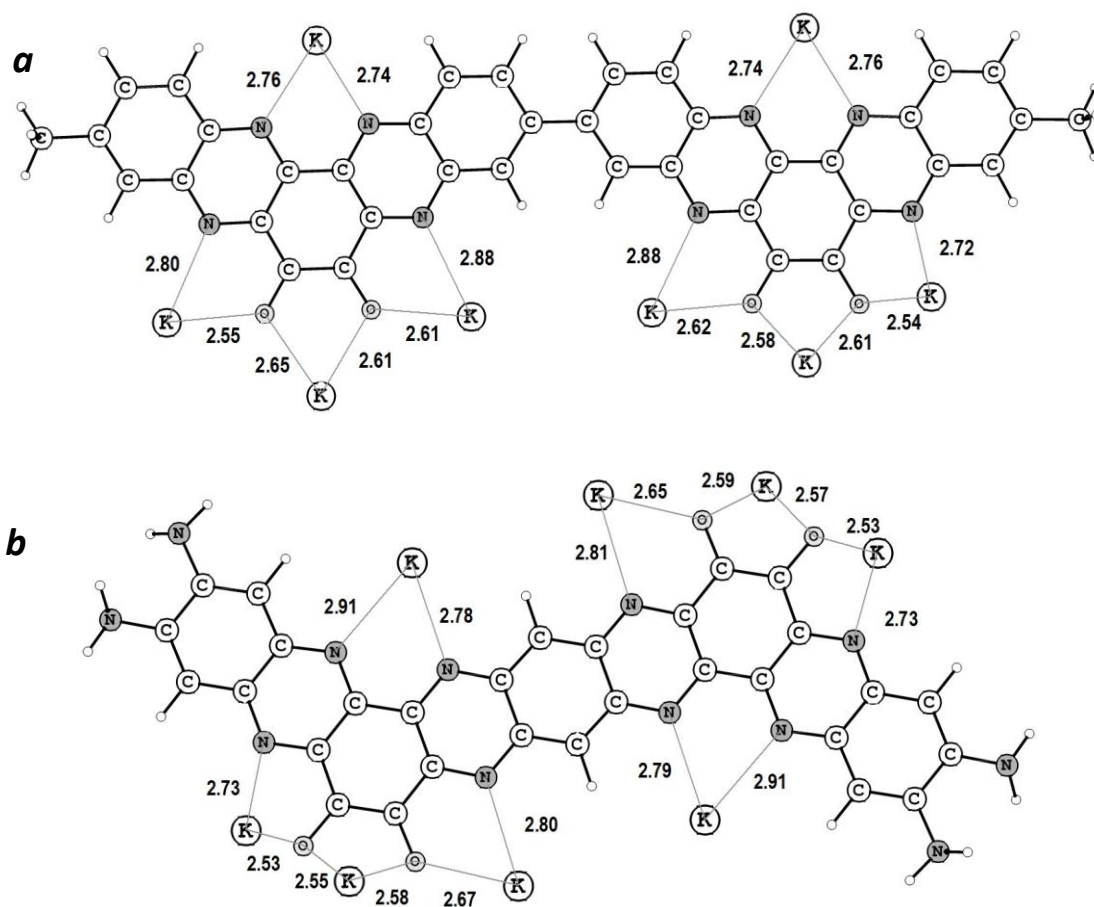


Fig. A.7 Computed molecular structures of the oligomeric frameworks resembling polymers **P1** (a) and **P2** (b) after the introduction of 4 K^+ ions and the same number of electrons per repeating unit.

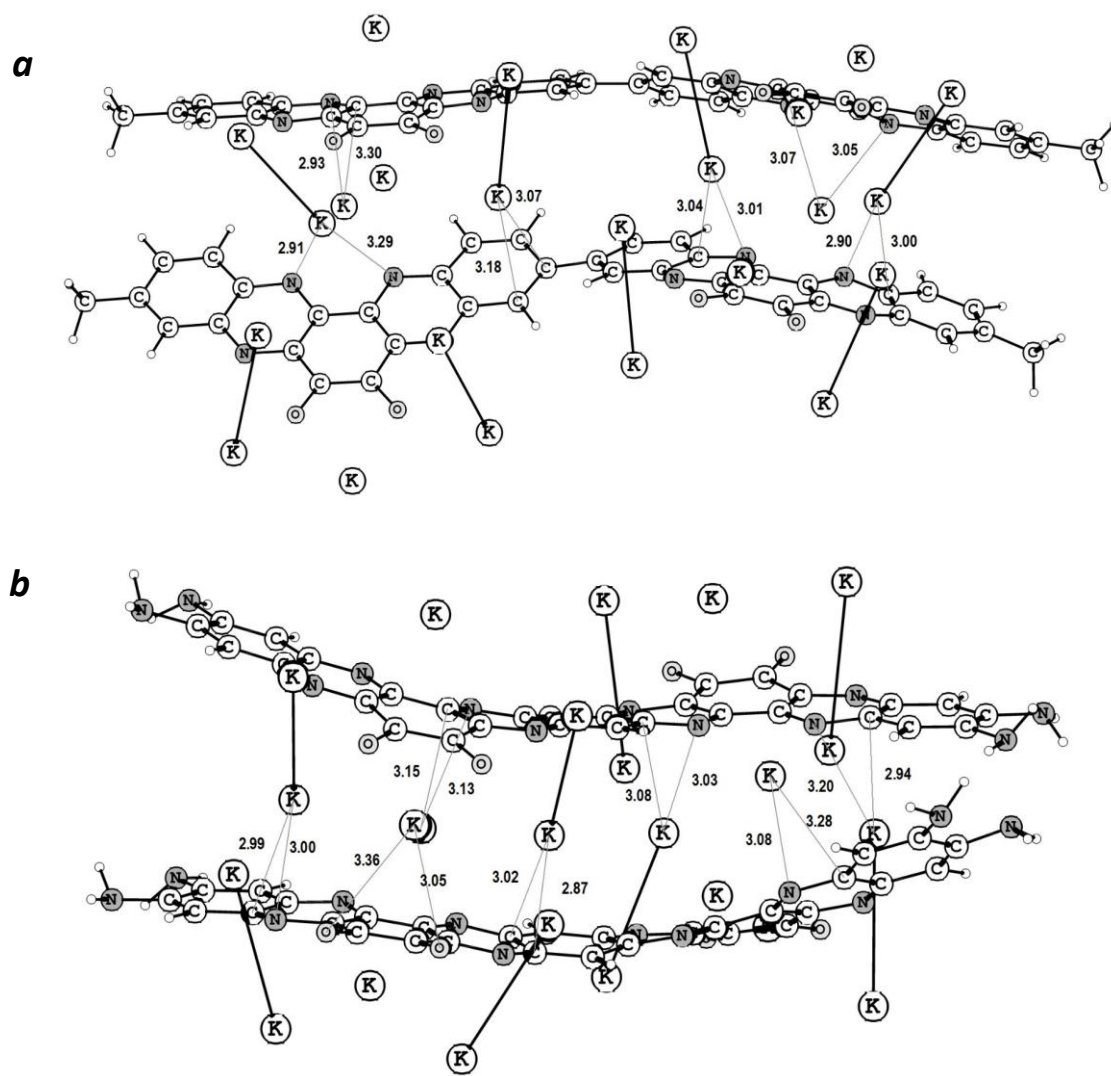


Fig. A.8 Computed structures of the supramolecular dimers formed by **P1** (a) and **P2** (b) after the introduction of 6 K^+ ions and the same number of electrons per repeating unit.

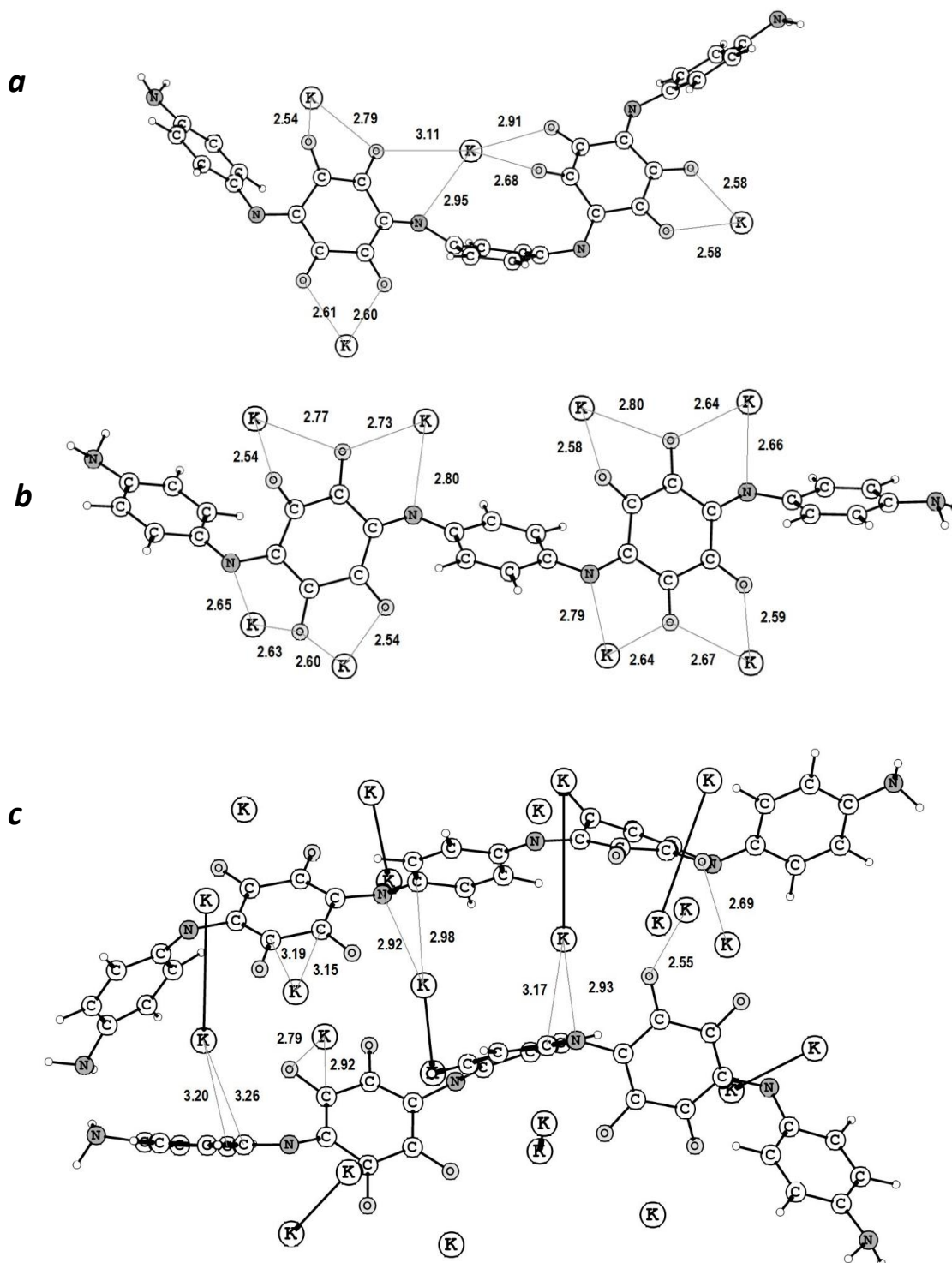


Fig. A.9 Computed molecular structures of the oligomeric frameworks of the model polymer **P4*** (see Fig. S2g above) after the introduction of 2 (a), 4 (b) and 6 (c) K^+ ions and the same number of electrons per each repeating unit. The supramolecular dimer structure is shown in (c).

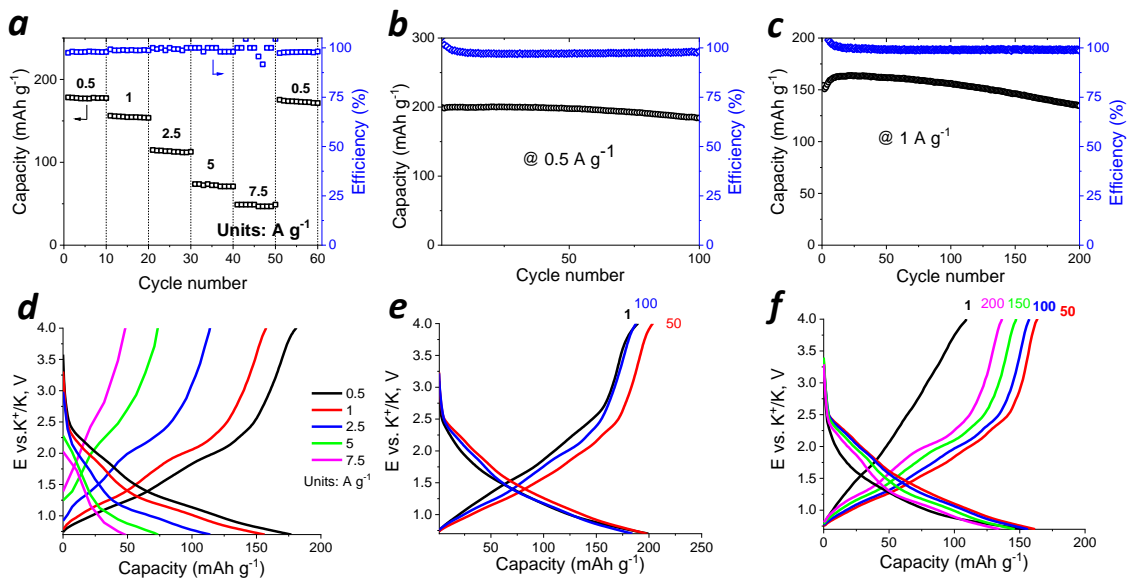


Fig. A.10 The rate capability of the electrodes comprised of polymer **P1** with increased loading of 0.7 mg cm^{-2} (a) and the cell cycling behaviour at the current densities of 0.5 A g^{-1} (b) and 1.0 A g^{-1} (c). The corresponding charge-discharge curves are presented in (d-f).

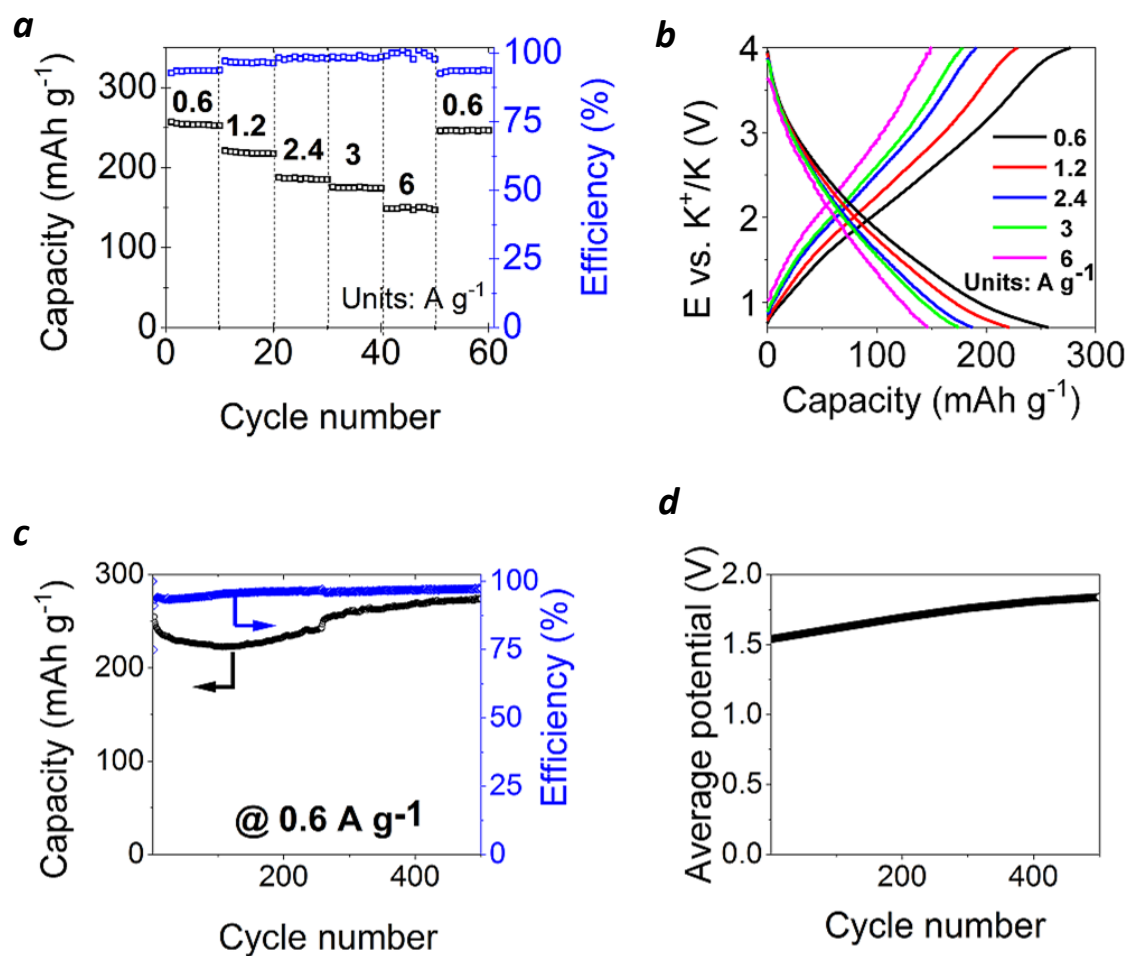


Fig. A.11 The rate capability of the electrodes comprised of polymer **P2** (a); charge-discharge curves recorded at different current densities (b); cycling performance of **P2**//K half cells after preconditioning at 0.6 A g⁻¹(c); evolution of the average discharge potential of the cells upon cycling (d).

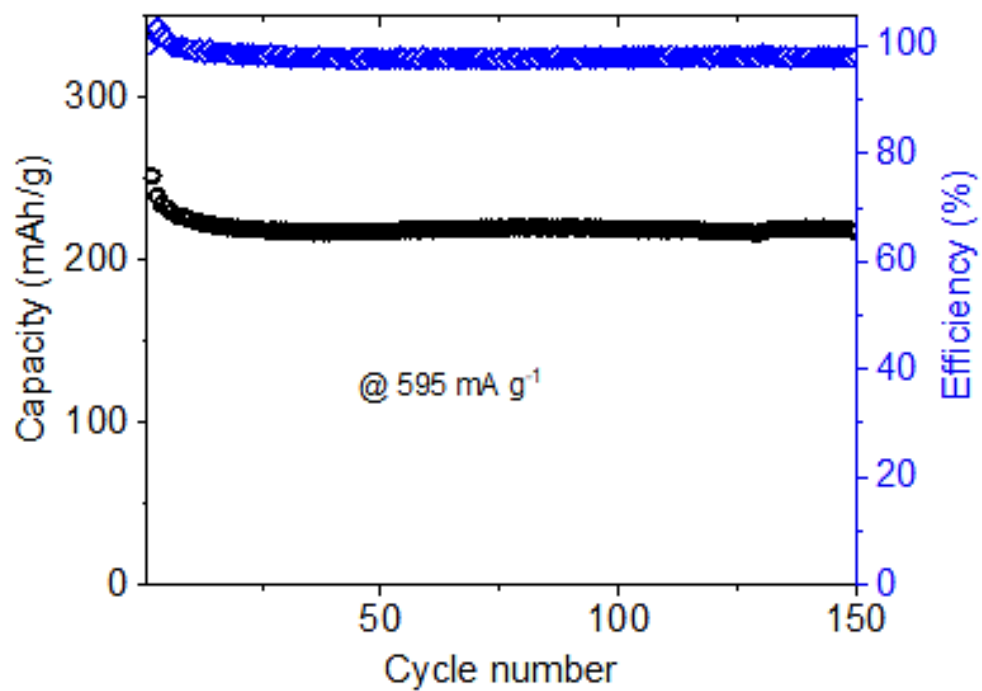


Fig. A.12 The cycling behaviour of the cells comprised polymer **P2** with increased areal loading (0.7 mg cm^{-2}) at the current density of 0.595 A g^{-1}

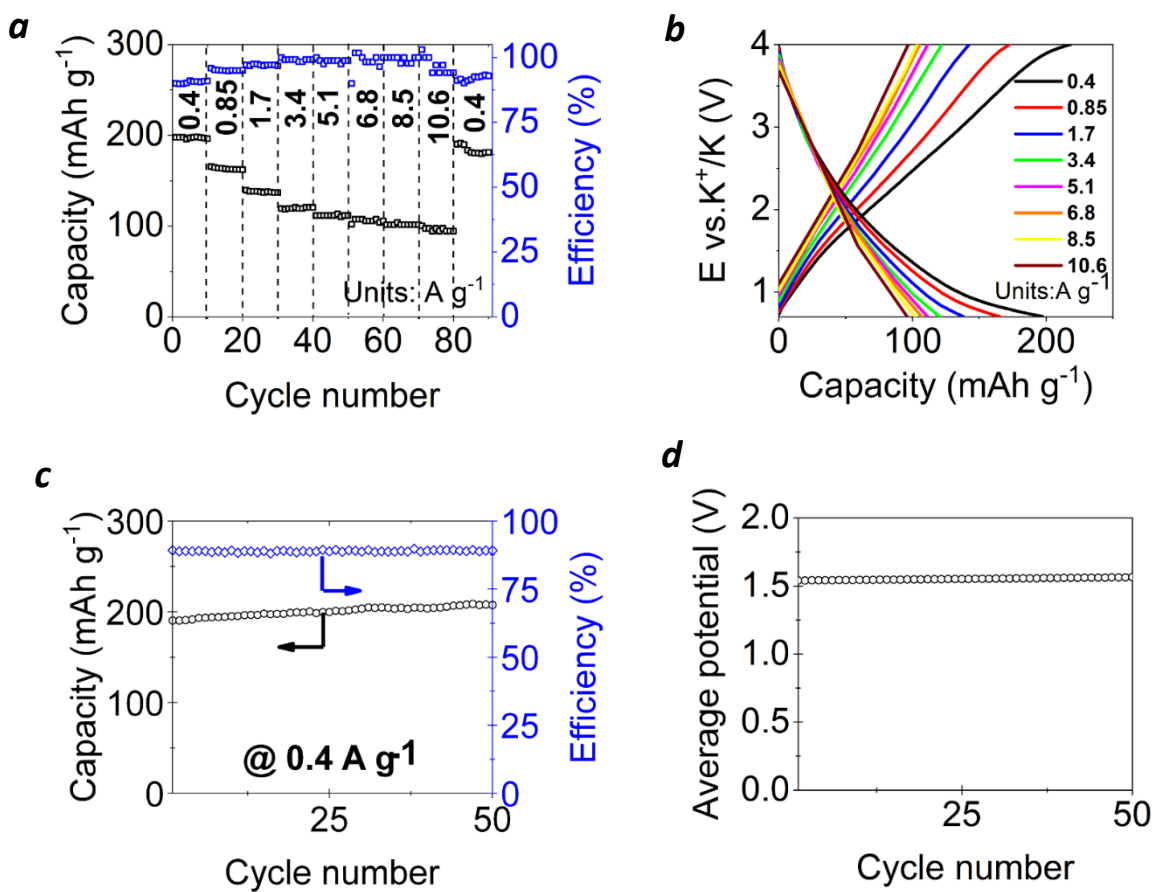


Fig. A.13 The rate capability of the electrodes comprised of polymer **P3** (a); charge-discharge curves recorded at different current densities (b); cycling performance of **P3**/K half cells after preconditioning at 0.4 A g⁻¹(c); evolution of the average discharge potential of the cells upon cycling (d).

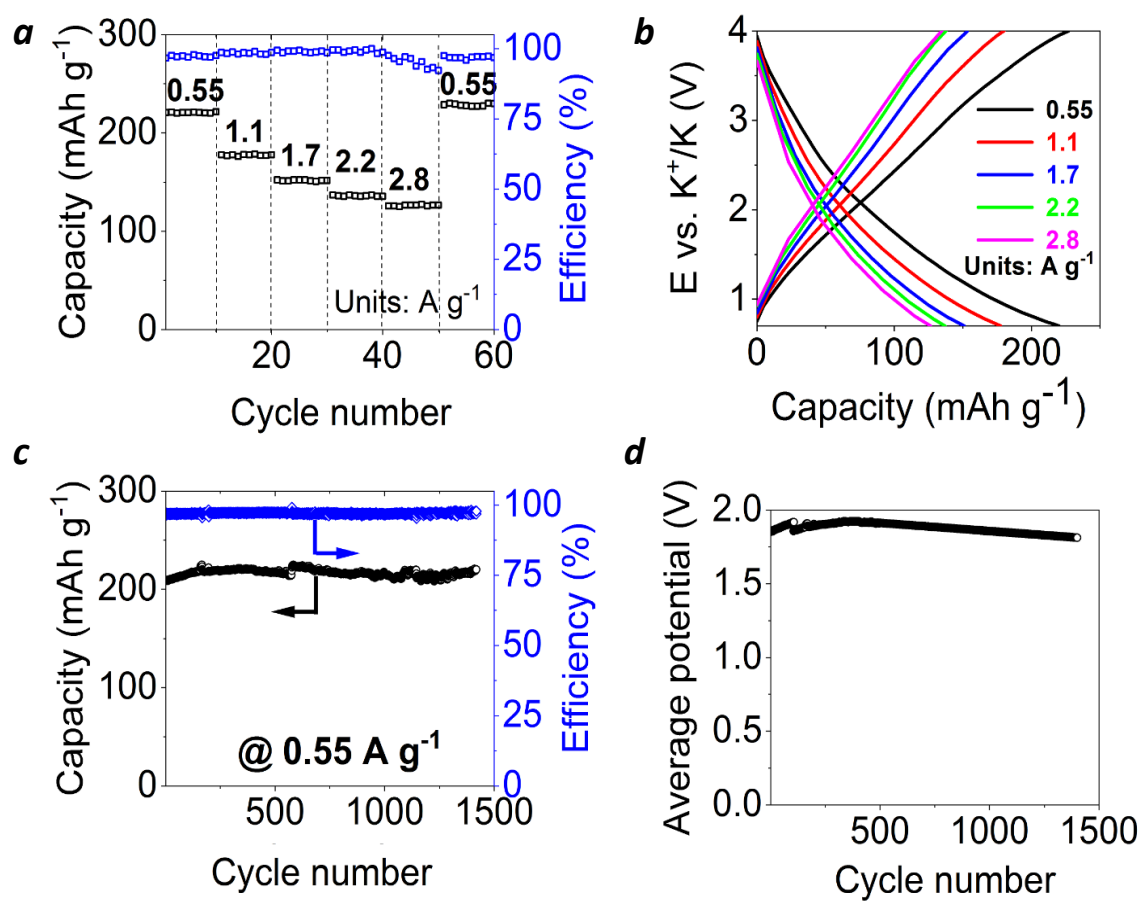


Fig. A.14 The rate capability of the electrodes comprised of polymer **P4** (a); charge-discharge curves recorded at different current densities (b); cycling performance of **P4**/ K half cells after preconditioning at 0.55 A g^{-1} (c); evolution of the average discharge potential of the cells upon cycling (d).

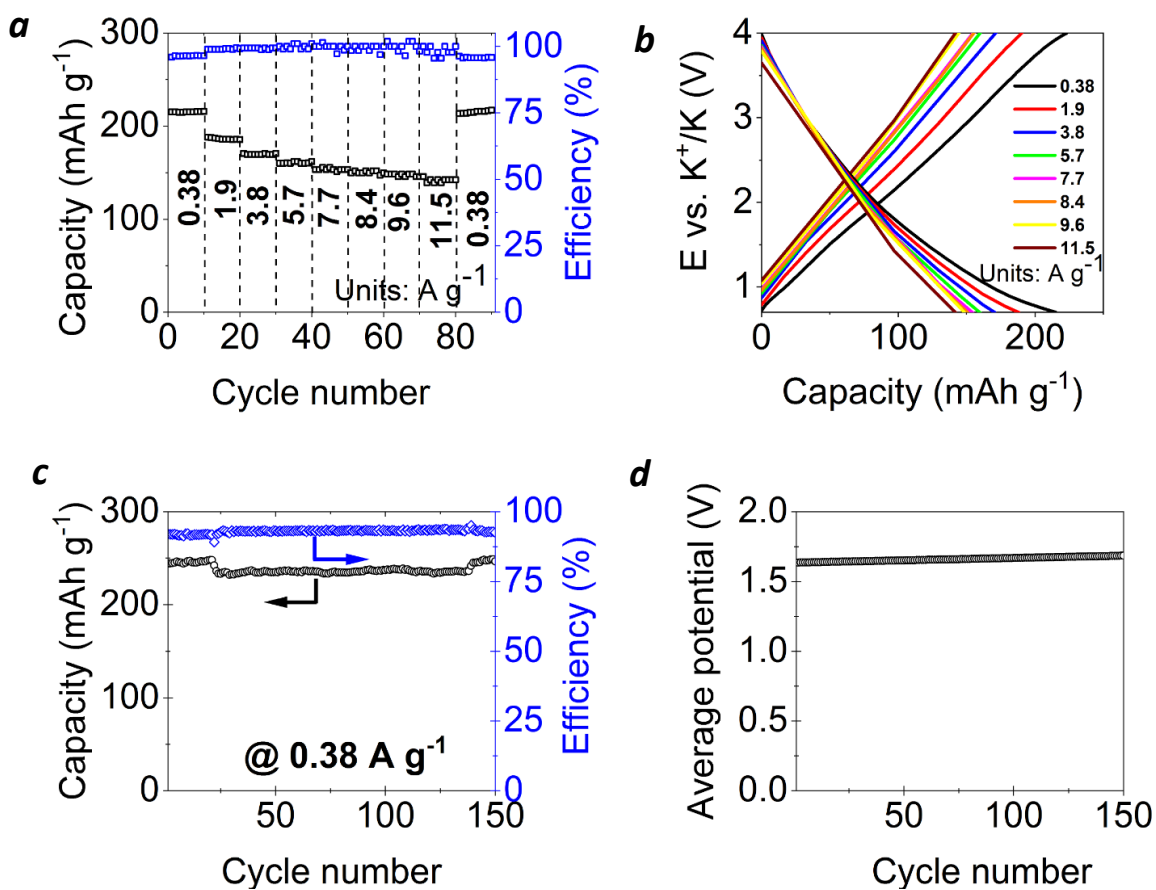


Fig. A.15 The rate capability of the electrodes comprised of polymer **P5** (a); charge-discharge curves recorded at different current densities (b); cycling performance of **P5**//K half cells after preconditioning at 0.38 A g⁻¹(c); evolution of the average discharge potential of the cells upon cycling (d).

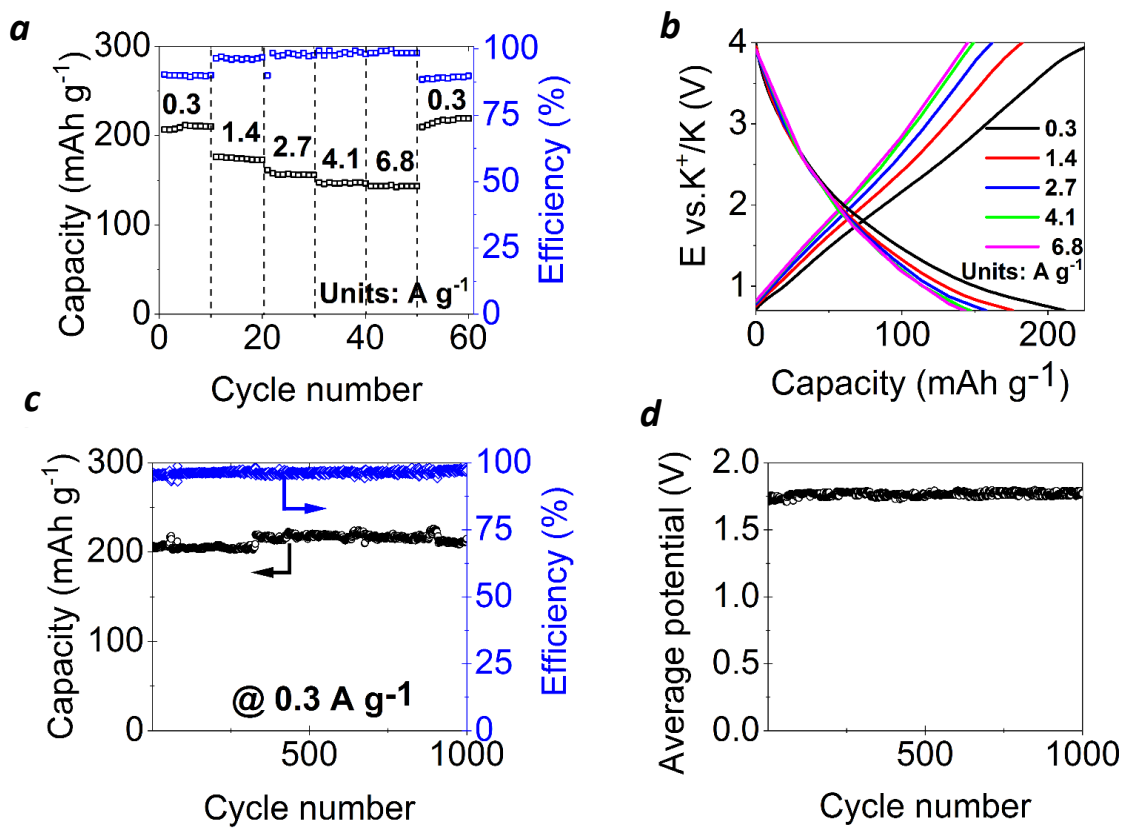


Fig. A.16 The rate capability of the electrodes comprised of polymer **P6** (a); charge-discharge curves recorded at different current densities (b); cycling performance of **P6**/ K half cells after preconditioning at 0.3 A g^{-1} (c); evolution of the average discharge potential of the cells upon cycling (d).

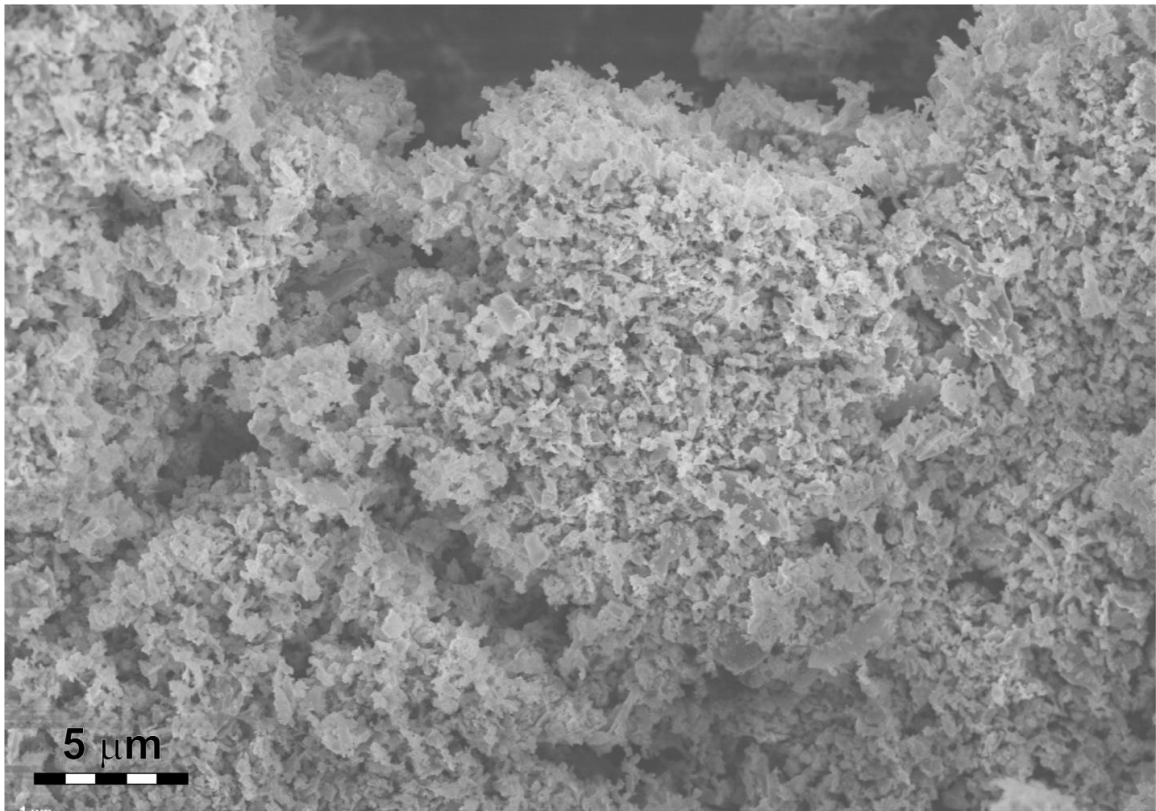
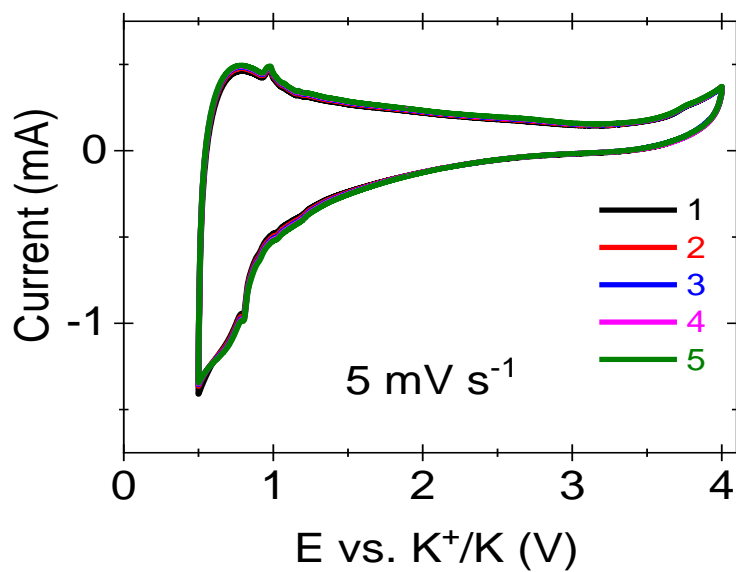


Fig. A.17 SEM image of the well-grinded powder of polymer **P7**.

a



b

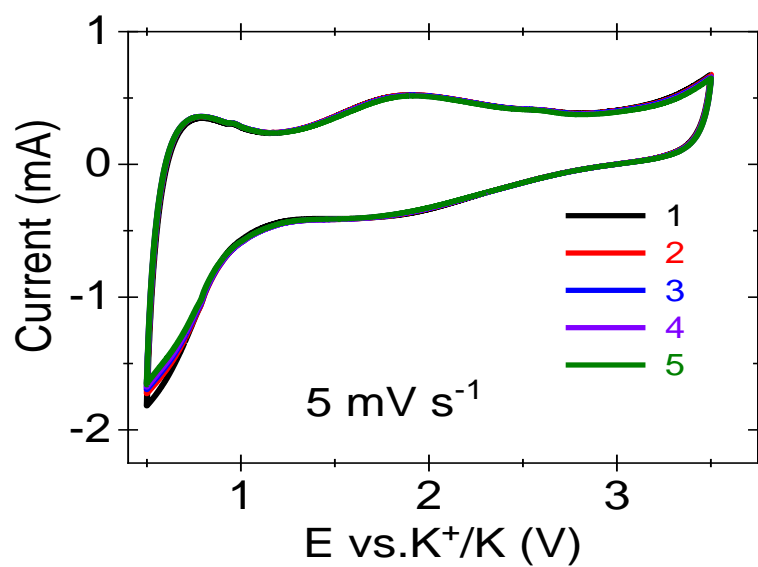


Fig. A.18 Cyclic voltammograms of **P8** (a) and **P9** (b) after preconditioning at 5 mV s⁻¹.

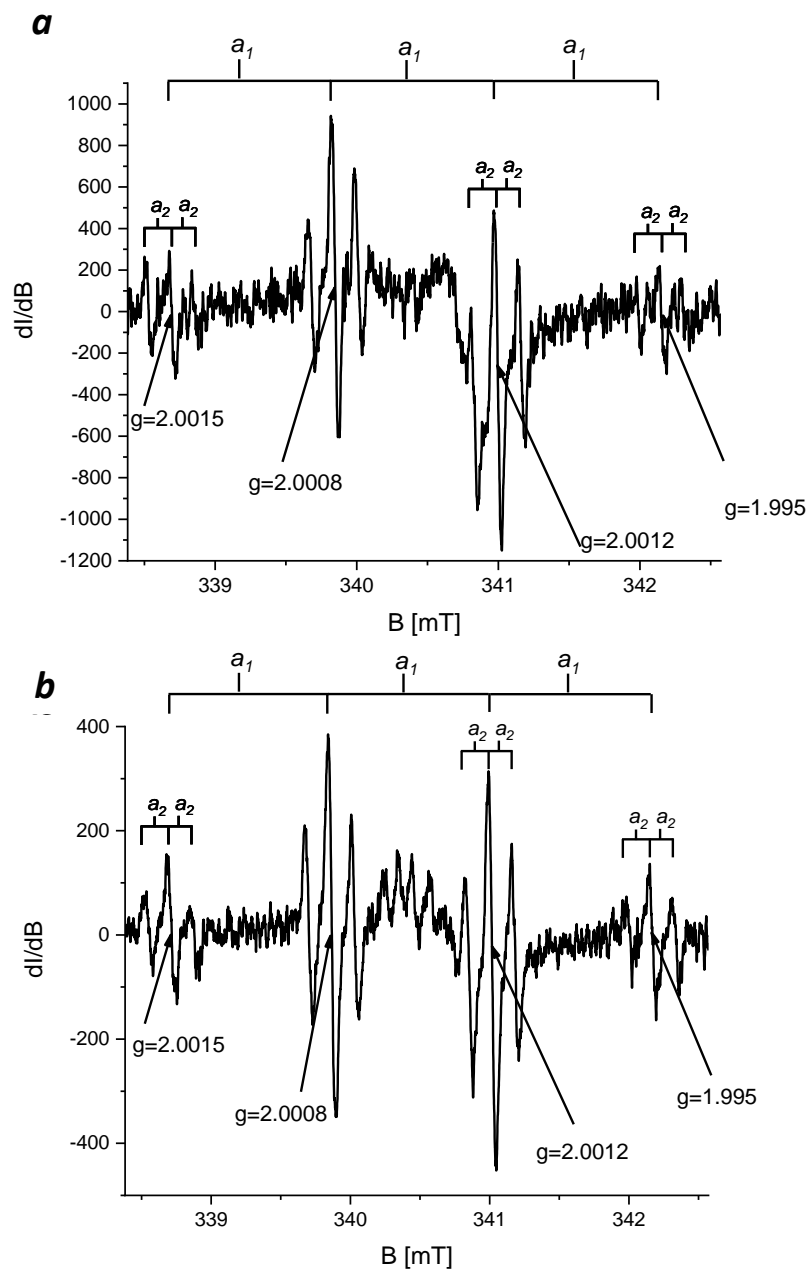


Fig. A.19 Typical ESR spectra registered in the spectroelectrochemical cells with the redox-active polymer composite (polymer + Super-P carbon + PVDF on Al foil) working electrodes, Pt counter electrode and 1M KPF₆ solution in dimethoxyethane (DME) as electrolyte: (a) polymer **P7**; (b) polymer **P8**.

Table A.2 The comparison of the experimental, computed and literature data on HFCs for several radical species

Radical	Computed HFCs, mT	Experimental HFCs, mT	Ref.
Experimentally obtained spectrum	-	1.16 (3H), 0.17 (2H)	This work
CH ₃ ·	2.32	2.31	[7]
[CH ₃ COCH ₃]·	1.78	1.62	[8]
		1.69	[9]
[CH ₃ COOCH ₂ CH ₃]·	1.20 (3H), 0.16 (2H)	1.12 (3H)	[8]
		1.36 (3H)	[10]
CH ₃ O-C=CH ₂	0.04 (3H), 1.5 (1H-trans), 4.59 (1H-cis)	N/A	N/A

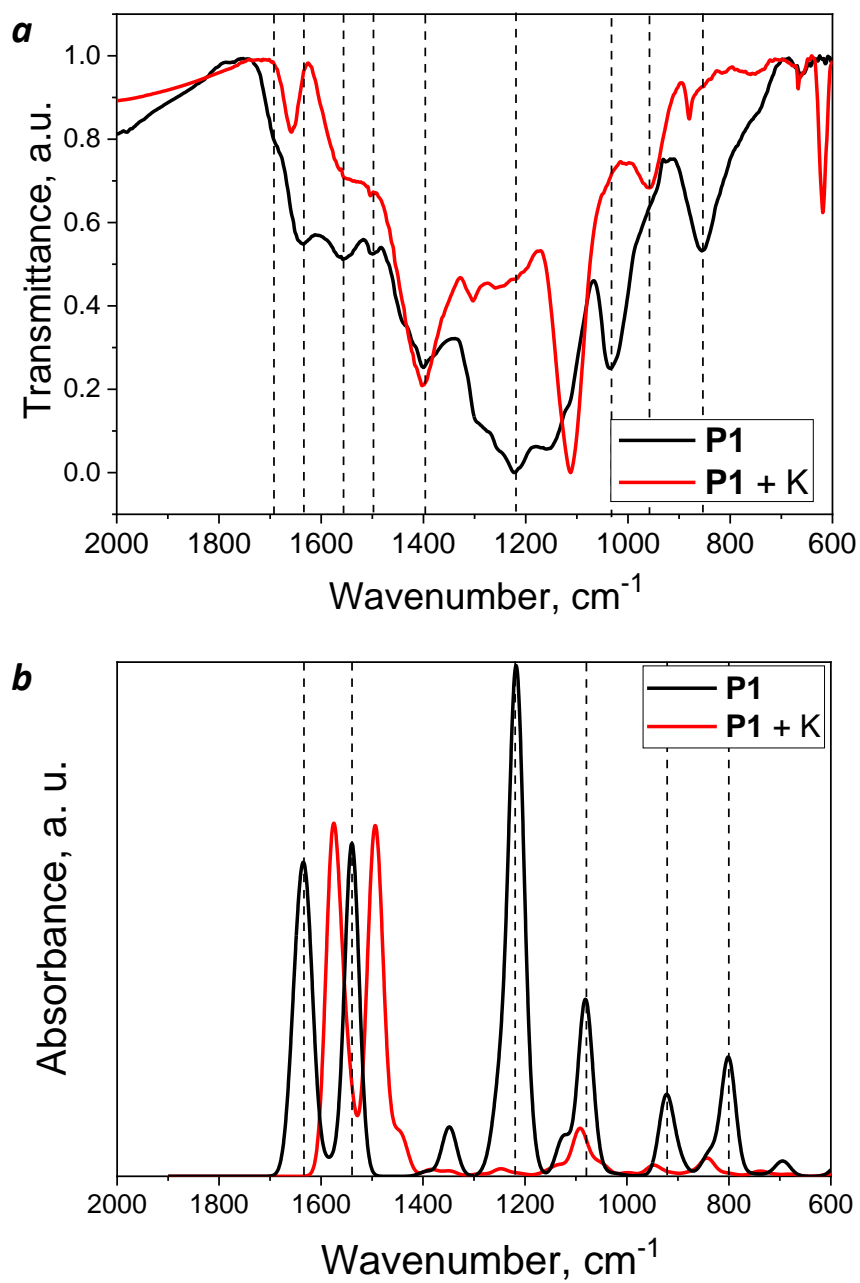


Fig. A.20 The comparison of the experimental ATR FTIR spectral changes induced by potassiation of **P7** (a) and the computed spectral evolution for the model type I oligomer (Fig. S1 above) upon attachment of two potassium atoms per repeating unit (b)

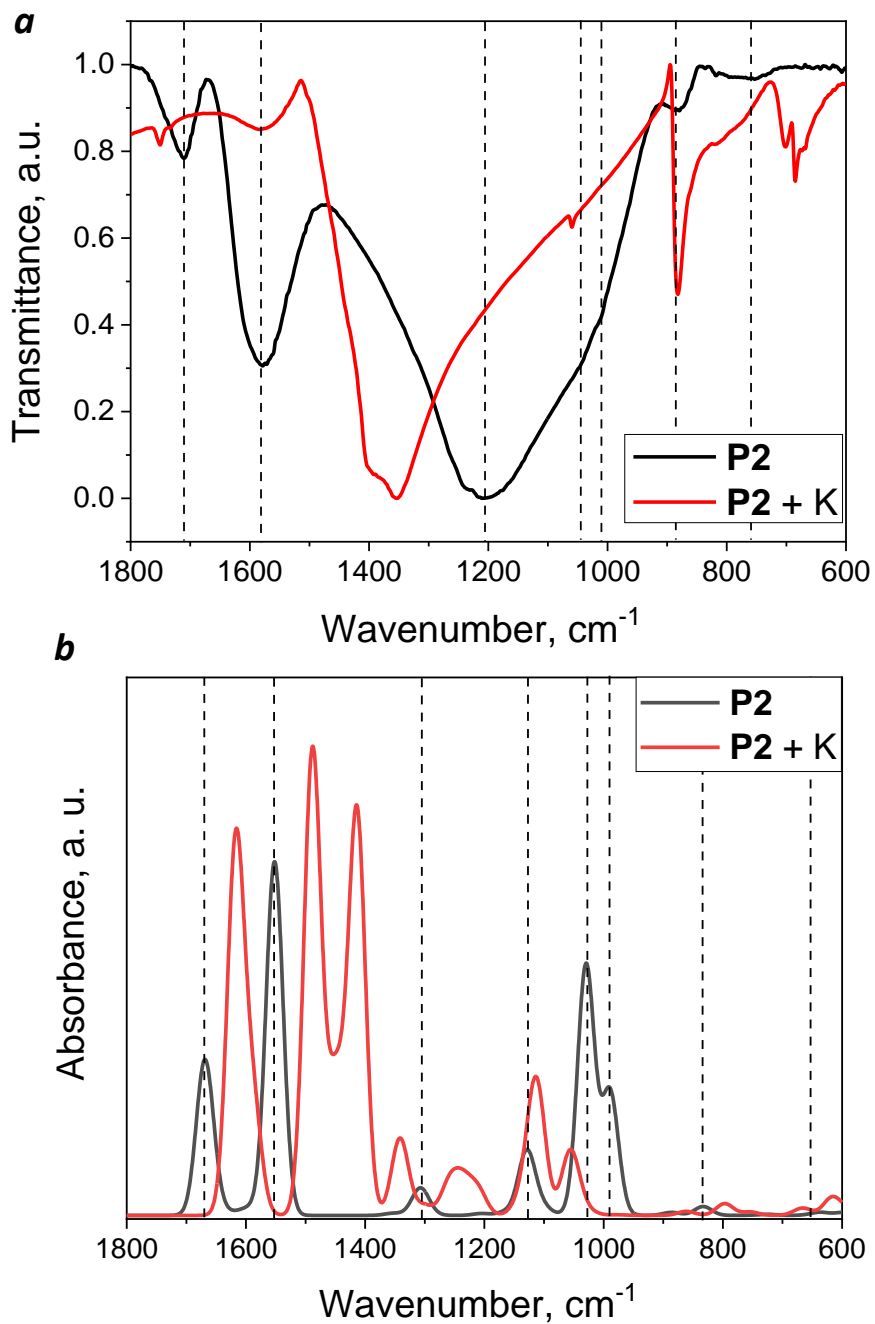


Fig. A.21 The comparison of the experimental ATR FTIR spectral changes induced by potassiation of **P8** (a) and the computed spectral evolution for the **P8** oligomer upon attachment of two potassium atoms per repeating unit (b)

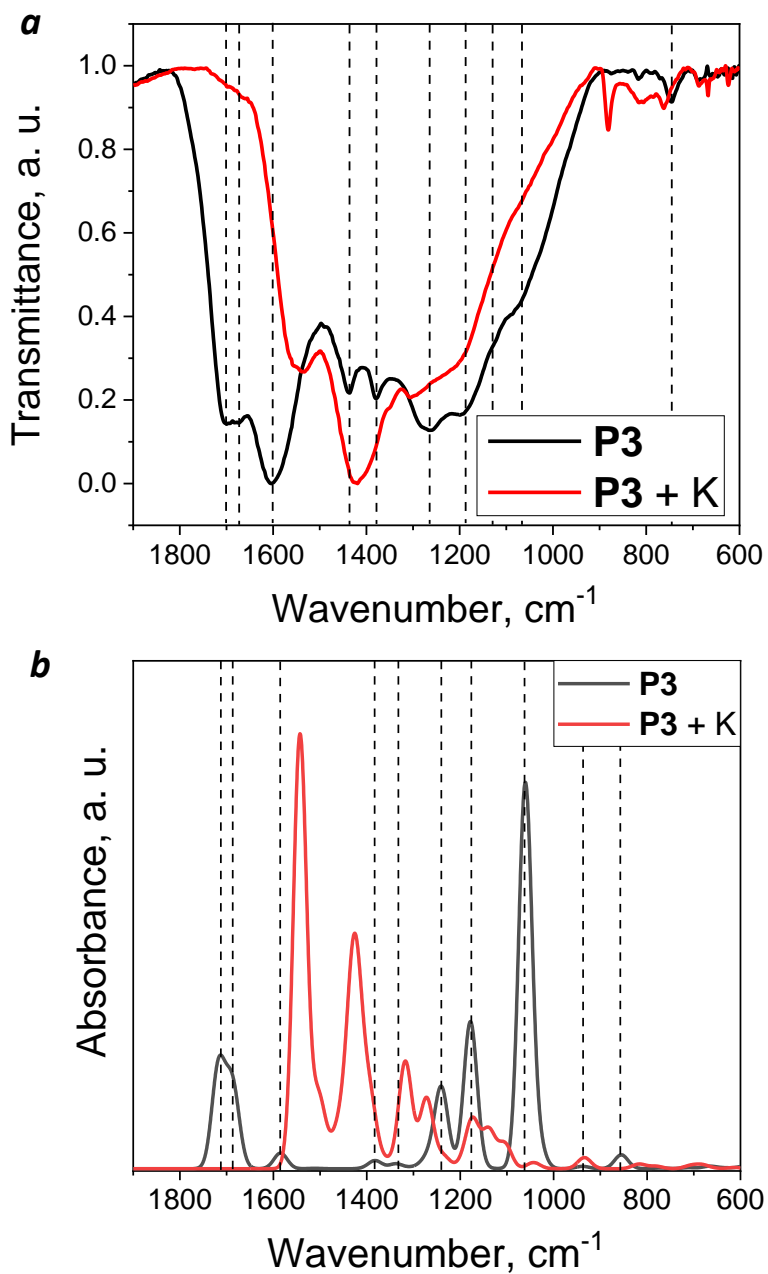


Fig. A.22 The comparison of the experimental ATR FTIR spectral changes induced by potassiation of **P9** (a) and the computed spectral evolution for the **P9** oligomer upon attachment of two potassium atoms per repeating unit (b)

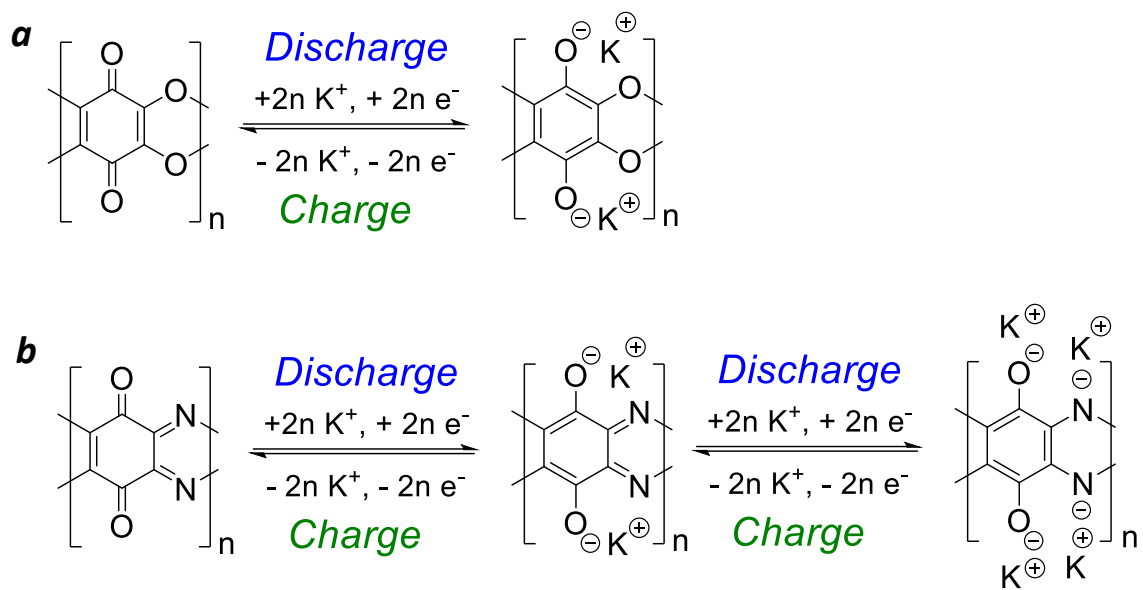


Fig. A.23 The schemes illustrating K^+ storage and release in the electrodes based on polymers **P8**(a) and **P9** (b)

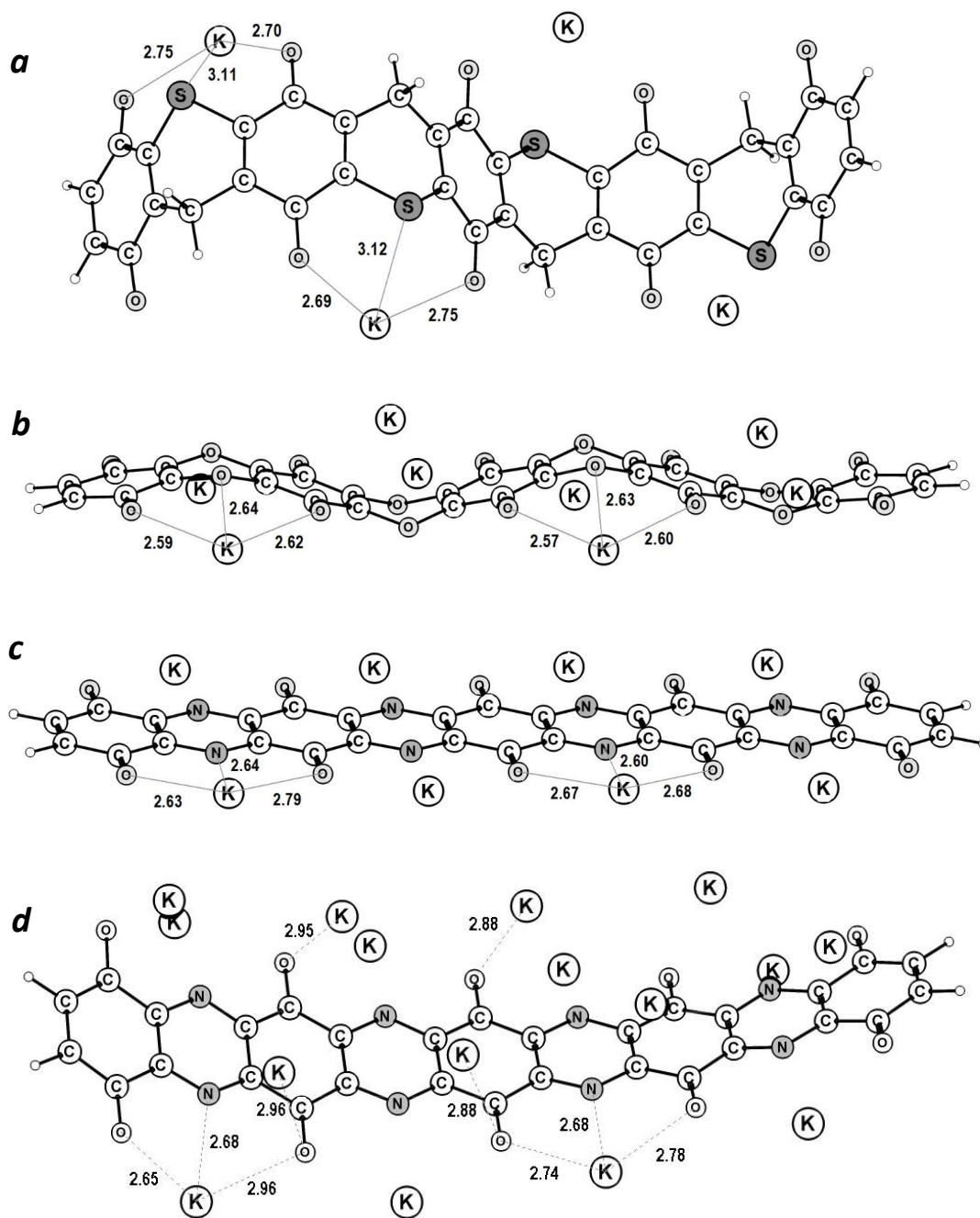


Fig. A.24 The computed structures of the potassiated polymers **P7** (a), **P8** (b) and **P9** (c-d) with 1 (a), 2 (b, c) and 4 (d) potassium ions introduced per the polymer repeating unit.

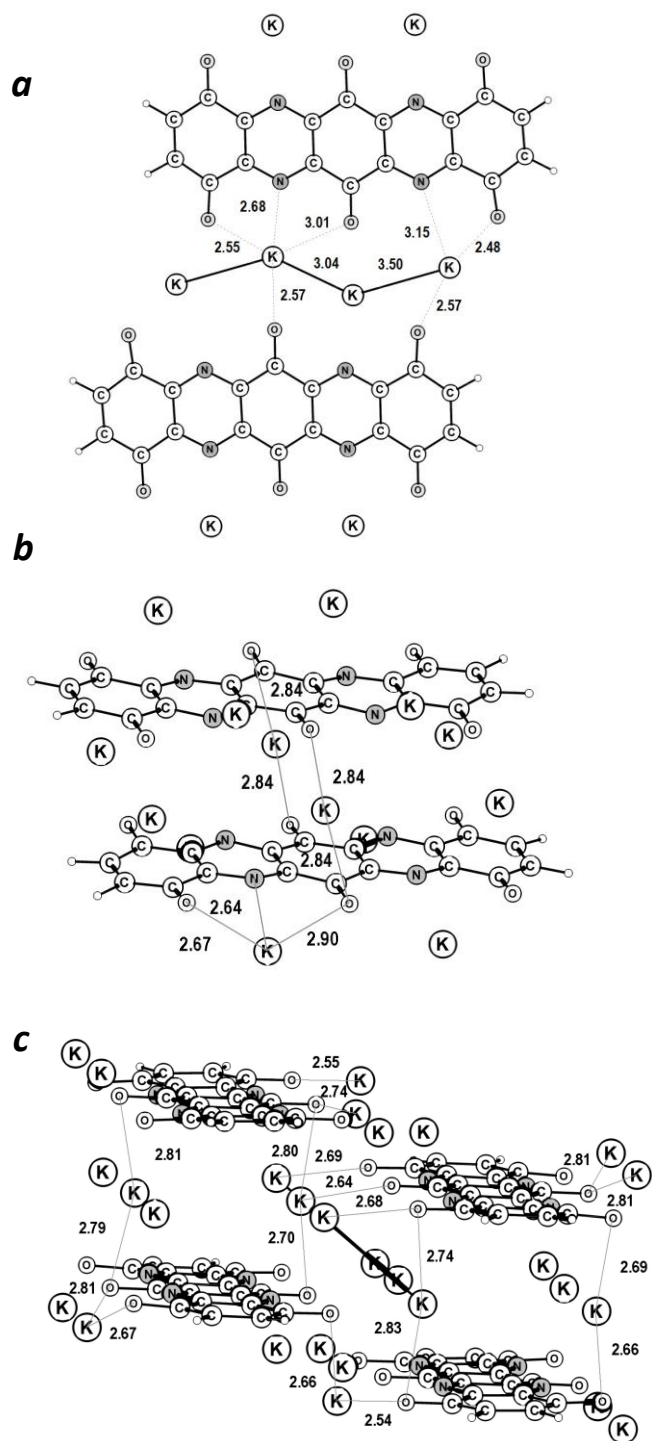


Fig. A.25 The computed structure of the supramolecular dimers $[P3K2]_2$ (a), $[P3K4]_2$ (b) and dimer of dimers $\{[P3K4]_2\}_2$ (c).

Table A.3 Specific energies per inserted K^+ ion released upon reductive metalation of polymers **P7-P9** according to DFT calculations performed for the model oligomers of different lengths.

Polymer	Number of repeating units in the model oligomer	Number of K^+ ions per repeating unit	Specific accumulated energy ΔE_n, eV
P7	2	1	2.04
	4	0.5	1.91
	4	1	1.89
P8	2	2	2.09
	4	2	2.05
	5	2	1.91
P9	2	1	2.69
	2	2	2.23 (2.65)*
	4	2	2.20 (3.25)*
	4	4	1.08 [1.71]*

* - values in round and square brackets correspond to the estimates for 2D and 3D structures, respectively

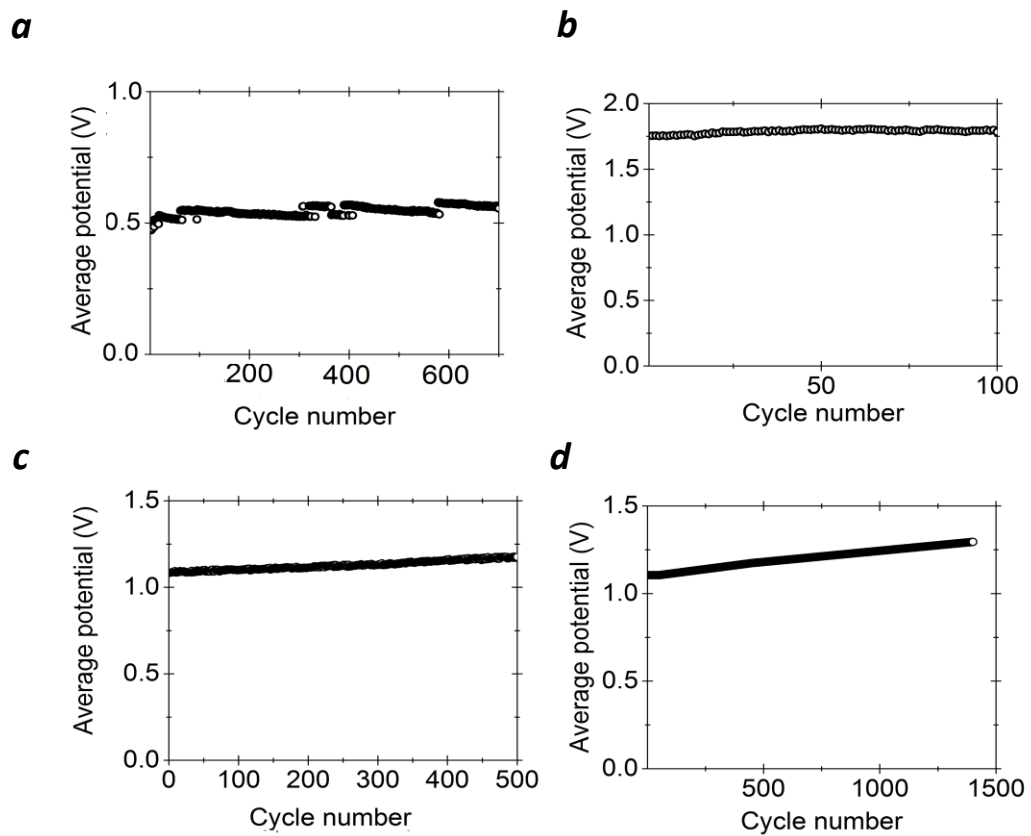


Fig. A.26 Average discharge potentials of potassium half-cells assembled with the electrodes comprising P1 (50 wt. %) (a), **P1** (70 wt. %) (b), **P2** (c) and P3 (d).

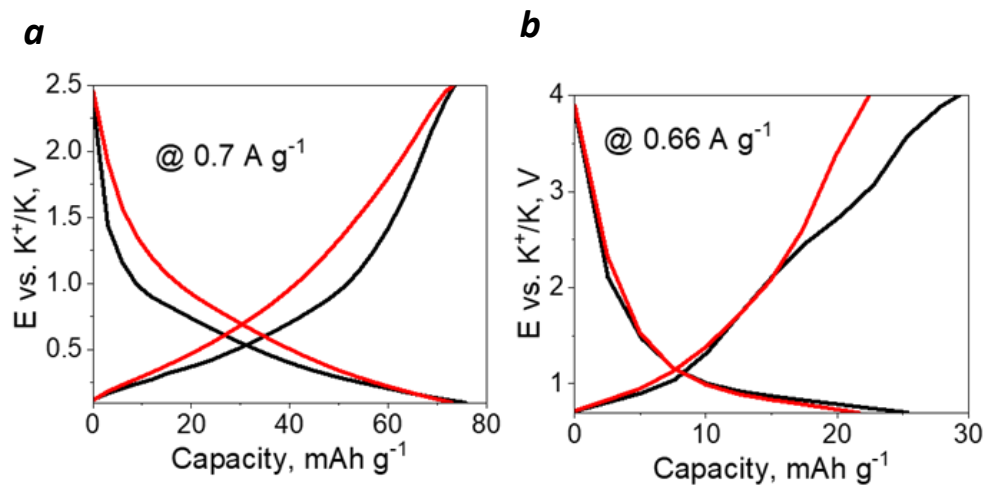


Fig A.27 Charge-discharge profiles for the reference potassium half-cells assembled with the electrodes comprising electrochemically inactive Al₂O₃ (50%), Super P carbon filler (40%), and PVdF binder (10%) to evaluate the carbon contribution to the overall cell capacity. The results are shown for (a) 0.1-2.5 V and (b) 0.7-4.0 V potential ranges.